

**PHOTOPRODUCTION OF $\Phi(1020)$
MESON IN NEUTRAL DECAY MODE**

$\gamma p \rightarrow \phi p \rightarrow p K_S \bar{K}_L$

by

Heghine Seraydaryan
May 15, 2011

TABLE OF CONTENTS

	Page
List of Tables	iv
List of Figures	x
 CHAPTERS	
1 Introduction	1
2 Theory	4
2.1 Introduction to Theory	4
2.2 Kinematical Variables	6
2.3 The diffractive amplitudes	10
2.3.1 Pomeron exchange amplitudes	10
2.3.2 Pseudoscalar meson exchange amplitudes	13
2.3.3 f'_2 meson and glueball exchange	14
2.4 Baryon and baryon resonance exchange	15
2.4.1 Baryon resonance exchange	15
2.4.2 Direct ϕ meson Radiation	15
2.5 Theoretical results and expectations	16
2.5.1 Unpolarized cross section	16
2.5.2 Spin observables	18
2.6 Summary	21
3 Data Analysis	22
3.1 Data selection	22
3.2 Energy and Momentum Corrections	24
3.2.1 Tagger Energy Corrections	24
3.2.2 Energy Loss Correction	24
3.2.3 Momentum Corrections	28
3.3 The Detector Efficiency Corrections	33
3.4 Fiducial Cuts	41
3.5 Particle Identification	41
3.6 Background Subtraction	48
3.7 Acceptance Correction and Normalization	51
3.7.1 Monte Carlo generator	51
3.7.2 Acceptance	69
3.7.3 The Target Density	70
3.7.4 Normalization to the Flux	70
4 Physics Results	84
4.1 Differential Cross Sections	84
4.2 Angular Distribution Functions and Spin Observables	90

4.3 Summary	99
-----------------------	----

LIST OF TABLES

	Page
I Table of corrections applied to data.	23
II Removed problematic scintillator paddles.	41
III Table of kinematic cuts applied for data selection.	48
IV The parameter values, used to calculate liquid hydrogen target density [55].	70

LIST OF FIGURES

	Page
1 Experimental results for the energy dependence of $(d\sigma/dt)_{t=- t _{min}}$ measured by different collaborations [2].	2
2 Phase-space overlap of $\phi(1020)$ meson and $\Lambda(1520)$ baryon [11].	2
3 Feynman diagrams of two γp processes producing the same K^+K^-p final state: via the ϕ resonance (left) and via the Λ resonance(right).	3
4 Diagrams of ϕ meson production mechanisms by A.I. Titov [13]	5
5 The schematic pictures of the $\gamma N \rightarrow \phi N \rightarrow K_SK_L$ reaction in c.m.s.	6
6 Diagrammatic representation of GJ, H and A reference systems in ϕ meson rest frame, where k , q , p and p' are the four momenta of the incoming photon, outgoing meson, initial and final nucleon, respectively.	7
7 Pomeron exchange models for ϕ meson production: (a) VDM model, (b) DL model [13].	10
8 Two gluon exchange mechanism for vector meson photoproduction [14].	12
9 The total cross section as a function of photon energy: (a) modeels A,B and C indicated by dashed, long-dashed and dot-dashed curves, (b) hybrid model [14].	17
10 (a) The differential cross section as a function of $-t$ at $E_\gamma = 2.2$ GeV for PS exchange (long-dashed), diffractive channels (dot-dashed), resonance excitation (dashed) and the total amplitude (solid). (b) The differential cross section as a function of ϕ production angle at $E_\gamma = 1.7, 2.0$ and 3.6 GeV. The data are from [35, 36], [14].	18
11 The spin-density matrix elements as a function of $-t$ at $E_\gamma = 2.2$ GeV: (a) for the Pomeron exchange amplitude, (b) for the full model [14].	19
12 Angular distribution function at $E_\gamma = 2.2$ GeV and $ t =0.2, 0.5$ and 1.8 GeV^2 as a function of: (a) $\cos\Theta$, (b) Φ . [14]	20
13 Spin-density matrix elements as a function of E_γ at $ t =0.4$ GeV^2 for: (a) Pomeron exchange amplitude, (b) full model. [14]	21
14 The tagger time subtracted from event start time. 2 ns cut was used to select good photons.	23
15 (a) The missing mass shift in the reaction $\gamma p \rightarrow K^+K^-X$, $\Delta M = M_X - M_{proton}$, (b) Beam energy correction factor $R = E_{corrected}/E_\gamma$ as a function of run number. [49]	25
16 Tagger energy correction $R = E_\gamma/E_{\gamma 0}$ as a function of tagger ID. The red points are the corrections before the electron energies were corrected, and the blue points show the corrections after the electron energy corrections. [49]	26
17 The difference of the missing mass of the reaction $\gamma p \rightarrow \pi^+\pi^-X$ and the proton mass $\Delta M = M_X - M_p$ as a function of tagger ID after the tagger energy correction. [49]	27

18	Momentum corrections for positive particles (π^+, K^+ , protons) $R = P_{\text{corrected}}/P_{\text{measured}} - 1$ estimated from the missing mass distributions in:(a,b,c) $\gamma p \rightarrow \pi^+ \pi^- p$,(d) for protons from the reaction $\gamma p \rightarrow K^+ K^- p$. [49]	29
19	Momentum corrections for negative particles (π^-, K^-) $R = P_{\text{corrected}}/P_{\text{measured}} - 1$ [49]	30
20	The mass distributions of missed protons before and after the corrections were applied in two reactions:(a) $\gamma p \rightarrow \pi^+ \pi^- X$, (b) $\gamma p \rightarrow K^+ K^- X$. [49]	31
21	Invariant and missing masses after all corrections were applied. The deviation from the table value is indicated for each distribution on the right side of the plot. [49]	32
22	The calculation of efficiency coefficients for the protons. (a) The missing protons θ angle vs ϕ angle; (b) The detected protons θ angle vs ϕ ; (c) The 3D plots of efficiency coefficients for the protons plotted versus θ and ϕ angles in different momentum ranges.	35
23	The calculation of efficiency coefficients for the positive pions. (a) The missing π^+ θ angle vs ϕ angle; (b) The detected π^+ θ angle vs ϕ ; (c) The 3D plots of efficiency coefficients for the positive pions plotted versus θ and ϕ angles in different momentum ranges.	36
24	The calculation of efficiency coefficients for the negative pions. (a) The missing π^- θ angle vs ϕ angle; (b) The detected π^- θ angle vs ϕ ; (c) The 3D plots of efficiency coefficients for the negative pions plotted versus θ and ϕ angles in different momentum ranges.	37
25	Proton angular distributions:(a),(b) before efficiency corrections, (c),(d) after efficiency corrections.	38
26	π^+ meson angular distributions:(a),(b) before efficiency corrections, (c),(d) after efficiency corrections.	39
27	π^- meson angular distributions:(a),(b) before efficiency corrections, (c),(d) after efficiency corrections.	40
28	The invariant mass of $\pi^+ \pi^-$ system with a very broad cut on K_L mass $M(K_L) = 0.49765 \pm 0.1(GeV/c^2)$ and a cut $M(K_S K_L) < 1.07GeV/c^2$. The distribution was fit with Gaussian + first order Polynomial function to obtain the peak parameters.	42
29	The missing mass of $\gamma p \rightarrow p \pi^+ \pi^- (X)$ with a cut $M(K_S) = 0.49765 \pm 0.035(GeV/c^2)$ and a cut $M(K_S K_L) < 1.07GeV/c^2$. The distribution was fit with Gaussian + first order Polynomial function to obtain the peak parameters.	43
30	Invariant mass of $\pi^+ \pi^-$ system with a cut on mass of missing K_L from $\gamma p \rightarrow p \pi^+ \pi^- (X)$ reaction: $\Delta M(K_L) = 30MeV/c^2$	44
31	Missing mass of $\gamma p \rightarrow p \pi^+ \pi^- (X)$ reaction, with a cut on invariant mass of $\pi^+ \pi^-$: $ M(\pi^+ \pi^-) - 0.49765 < 0.015GeV/c^2$	45

32	Missing mass of $\gamma p \rightarrow p\pi^+\pi^-(X)$ reaction in $0.45\text{-}0.55\text{ GeV}/c^2$ range, with cuts: $\Delta M(K_S) = 16\text{ MeV}/c^2$ and $M(K_SK_L) < 1.07\text{ GeV}/c^2$	46
33	Invariant mass of K_SK_L with cuts: $\Delta M(K_S) = 16\text{ MeV}/c^2$ and $\Delta M(K_L) = 30\text{ MeV}/c^2$	47
34	Signal and background separation for $1.6 \geq E_\gamma < 1.7\text{ GeV}$ and different $\cos \theta_{c.m.}^\phi$ bins. The black histograms are the unweighted distributions from data. The red histograms are the signal distributions weighted by W. The blue histograms are the background distributions weighted by (1-W).	50
35	Signal and background separation for $1.7 \geq E_\gamma < 1.8\text{ GeV}$ and different $\cos \theta_{c.m.}^\phi$ bins. The black histograms are the unweighted distributions from data. The red histograms are the signal distributions weighted by W. The blue histograms are the background distributions weighted by (1-W).	52
36	Signal and background separation for $1.8 \geq E_\gamma < 1.9\text{ GeV}$ and different $\cos \theta_{c.m.}^\phi$ bins. The black histograms are the unweighted distributions from data. The red histograms are the signal distributions weighted by W. The blue histograms are the background distributions weighted by (1-W).	53
37	Signal and background separation for $1.9 \geq E_\gamma < 2.0\text{ GeV}$ and different $\cos \theta_{c.m.}^\phi$ bins. The black histograms are the unweighted distributions from data. The red histograms are the signal distributions weighted by W. The blue histograms are the background distributions weighted by (1-W).	54
38	Signal and background separation for $2.0 \geq E_\gamma < 2.1\text{ GeV}$ and different $\cos \theta_{c.m.}^\phi$ bins. The black histograms are the unweighted distributions from data. The red histograms are the signal distributions weighted by W. The blue histograms are the background distributions weighted by (1-W).	55
39	Signal and background separation for $2.1 \geq E_\gamma < 2.2\text{ GeV}$ and different $\cos \theta_{c.m.}^\phi$ bins. The black histograms are the unweighted distributions from data. The red histograms are the signal distributions weighted by W. The blue histograms are the background distributions weighted by (1-W).	56
40	Signal and background separation for $2.2 \geq E_\gamma < 2.3\text{ GeV}$ and different $\cos \theta_{c.m.}^\phi$ bins. The black histograms are the unweighted distributions from data. The red histograms are the signal distributions weighted by W. The blue histograms are the background distributions weighted by (1-W).	57

41	Signal and background separation for $2.3 \geq E_\gamma < 2.4$ GeV and different $\cos \theta_{c.m.}^\phi$ bins. The black histograms are the unweighted distributions from data. The red histograms are the signal distributions weighted by W. The blue histograms are the background distributions weighted by (1-W).	58
42	Signal and background separation for $2.4 \geq E_\gamma < 2.5$ GeV and different $\cos \theta_{c.m.}^\phi$ bins. The black histograms are the unweighted distributions from data. The red histograms are the signal distributions weighted by W. The blue histograms are the background distributions weighted by (1-W).	59
43	Signal and background separation for $2.5 \geq E_\gamma < 2.6$ GeV and different $\cos \theta_{c.m.}^\phi$ bins. The black histograms are the unweighted distributions from data. The red histograms are the signal distributions weighted by W. The blue histograms are the background distributions weighted by (1-W).	60
44	Signal and background separation for $2.6 \geq E_\gamma < 2.7$ GeV and different $\cos \theta_{c.m.}^\phi$ bins. The black histograms are the unweighted distributions from data. The red histograms are the signal distributions weighted by W. The blue histograms are the background distributions weighted by (1-W).	61
45	Signal and background separation for $2.7 \geq E_\gamma < 2.8$ GeV and different $\cos \theta_{c.m.}^\phi$ bins. The black histograms are the unweighted distributions from data. The red histograms are the signal distributions weighted by W. The blue histograms are the background distributions weighted by (1-W).	62
46	Signal and background separation for $2.8 \geq E_\gamma < 2.9$ GeV and different $\cos \theta_{c.m.}^\phi$ bins. The black histograms are the unweighted distributions from data. The red histograms are the signal distributions weighted by W. The blue histograms are the background distributions weighted by (1-W).	63
47	Signal and background separation for $2.9 \geq E_\gamma < 3.0$ GeV and different $\cos \theta_{c.m.}^\phi$ bins. The black histograms are the unweighted distributions from data. The red histograms are the signal distributions weighted by W. The blue histograms are the background distributions weighted by (1-W).	64
48	Signal and background separation for $3.0 \geq E_\gamma < 3.1$ GeV and different $\cos \theta_{c.m.}^\phi$ bins. The black histograms are the unweighted distributions from data. The red histograms are the signal distributions weighted by W. The blue histograms are the background distributions weighted by (1-W).	65

49	Signal and background separation for $3.1 \geq E_\gamma < 3.2$ GeV and different $\cos \theta_{c.m.}^\phi$ bins. The black histograms are the unweighted distributions from data. The red histograms are the signal distributions weighted by W. The blue histograms are the background distributions weighted by (1-W).	66
50	Signal and background separation for $3.2 \geq E_\gamma < 3.3$ GeV and different $\cos \theta_{c.m.}^\phi$ bins. The black histograms are the unweighted distributions from data. The red histograms are the signal distributions weighted by W. The blue histograms are the background distributions weighted by (1-W).	67
51	Signal and background separation for $3.3 \geq E_\gamma < 3.4$ GeV and different $\cos \theta_{c.m.}^\phi$ bins. The black histograms are the unweighted distributions from data. The red histograms are the signal distributions weighted by W. The blue histograms are the background distributions weighted by (1-W).	68
52	Calculated acceptances for different $t - t_{min}$ bins and different photon energy ranges.	72
53	Calculated acceptances for different $\cos\Theta$ bins in Helicity frame and different photon energy ranges.	73
54	Calculated acceptances for different $\cos\Theta$ bins in Gottfried-Jackson frame and different photon energy ranges.	74
55	Calculated acceptances for different azimuthal angle Φ bins in Helicity frame and different photon energy ranges.	75
56	Calculated acceptances for different azimuthal angle Φ bins in Gottfried-Jackson frame and different photon energy ranges.	76
57	The z component of proton vertex for data (blue) and simulation (red).	77
58	Momentum of π^- meson for data (blue) and simulation (red).	78
59	Momentum of π^+ meson for data (blue) and simulation (red).	79
60	$ t - t_0 $ dependences of differential cross section $d\sigma/dt$ for ϕ mesons from data (blue) compared to normalized MC distributions (red).	80
61	$\cos \theta_{c.m.}$ dependences of differential cross section $d\sigma/d\cos \theta_{c.m.}$ for ϕ mesons from data (blue) compared to normalized MC distributions (red).	81
62	\sqrt{s} dependences of differential cross section $d\sigma/dt$ for ϕ mesons from data (blue) compared to normalized MC distributions (red).	82
63	Photon flux as a function of photon beam energy.	83
64	The $ t - t_{min} $ dependence of the ϕ meson differential cross section $d\sigma/dt$ in different photon beam energy bins of 1.6-2.6 GeV energy range.	86
65	The $\cos\theta_{c.m.}^\phi$ dependence of the ϕ meson differential cross section $d\sigma/d\cos\theta_{c.m.}$ for different photon beam energy bins of 1.6-2.6 GeV energy range.	87

66	The \sqrt{s} dependence of the ϕ meson differential cross section $d\sigma/dt$ in different $\cos\theta_{c.m.}$ bins for $-0.55 < \cos\theta_{c.m.} < 0.25$ range.	88
67	The \sqrt{s} dependence of the ϕ meson differential cross section $d\sigma/dt$ in different $\cos\theta_{c.m.}$ bins for $0.25 < \cos\theta_{c.m.} < 0.95$ range.	89
68	Differential cross section $d\sigma/dt$ at $t = t_{min}$ (a) and ϕ meson photoproduction slope β (b) for the Neutral decay channel plotted as functions of photon beam energy E_γ in 1.6-2.6 GeV energy range. The error bars represent the statistical errors, errors of the flux calculation, efficiency error at 40% efficiency cut, acceptance errors. The systematic errors are included as dashed pink regions at horizontal axis.	91
69	The decay distribution of ϕ meson as a function of polar angle Θ in Helicity frame for the 'neutral' decay channel of $\phi(1020)$ meson.	92
70	The decay distribution of ϕ meson as a function of polar angle Θ in Gottfried-Jackson frame for the 'neutral' decay channel of $\phi(1020)$ meson.	93
71	The decay distribution of ϕ meson as a function of azimuthal angle Φ in Helicity frame for the 'neutral' decay channel of $\phi(1020)$ meson.	95
72	The decay distribution of ϕ meson as a function of azimuthal angle Φ in Gottfried-Jackson frame for the 'neutral' decay channel of $\phi(1020)$ meson.	96
73	Spin-density matrix element components ρ_{00}^0 (blue) and ρ_{1-1}^0 (red) for different photon beam energies in 1.6-2.6 GeV range in Helicity frame.	97
74	Spin-density matrix element components ρ_{00}^0 (blue) and ρ_{1-1}^0 (red) for different photon beam energies in 1.6-2.6 GeV range in Gottfried-Jackson frame.	98

CHAPTER 1

INTRODUCTION

The ϕ meson photoproduction mechanism is not yet well understood. In "diffractive" regime the Pomeron exchange mechanism is dominant, therefore, ϕ meson photoproduction is an important tool to study the gluonic interactions, considering the gluonic structure of pomerons. Also, ϕ photoproduction process can be used to study the strangeness content of nucleons, using OZI rule violations, when the ϕ -nucleon interactions are taking place through the vector mesons exchanges. At high momentum transfers or high t , the ϕ photoproduction process is a good channel to study a nucleon resonance. This domain has not been studied very well until now. Experimental data for ϕ meson photoproduction are in a very limited kinematic range until now [1, 2, 5, 3, 4, 6, 7, 8] and in K^+K^- decay mode only. For some measurements the differential cross sections showed some unexpected local enhancement in approximately 1.8-2.4 GeV photon beam energy range (see Fig. 1). The measurements were done without any cuts on $\Lambda(1520)$, which is a strong resonance that can coexist with $\phi(1020)$ (Fig. 3). Moreover, the phase-spaces of the two resonances overlap nearly in the same photon energy region, where the local "structure" is observed in cross section plots of ϕ meson (Fig. 2). The interference between the resonances can have some noticeable effects in particle production processes [9, 10]. Therefore, ϕ meson cross section behavior could be due to coexistence of $\Lambda(1520)$ baryon and the interference between the $\Lambda(1520)$ and ϕ .

As mentioned above, different collaborations have studied only the "charged" decay mode $\gamma p \rightarrow p\phi \rightarrow pK^+K^-$ of ϕ photoproduction. The current analysis is the first time measurement of the ϕ photoproduction in the "neutral" decay mode $\gamma p \rightarrow p\phi \rightarrow pK_SK_L$. In the "neutral" case there is no known coexisting prominent resonance as $\Lambda(1520)$ in "charged" channel. So this analysis provides a powerful possibility to check the ϕ meson photoproduction cross section and s -dependence of the t slope and compare the results of two decay modes. The high statistics data of g11 experiment allows not only measure a new decay mode, but also extend it into much wider kinematic range.

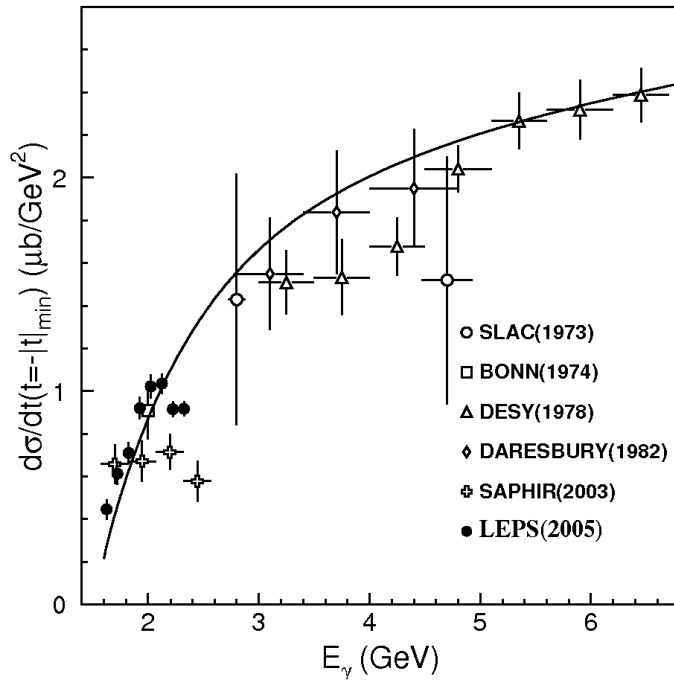


FIG. 1. Experimental results for the energy dependence of $(d\sigma/dt)_{t=-|t|_{min}}$ measured by different collaborations [2].

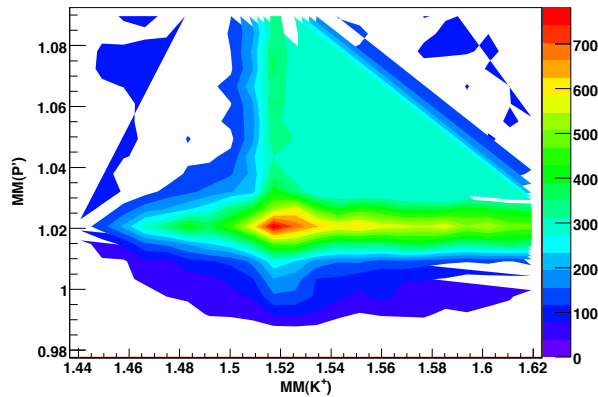


FIG. 2. Phase-space overlap of $\phi(1020)$ meson and $\Lambda(1520)$ baryon [11].

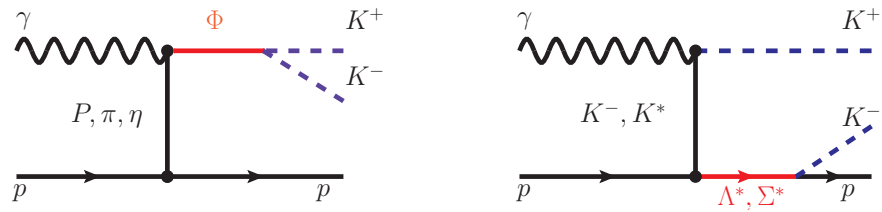


FIG. 3. Feynman diagrams of two γp processes producing the same K^+K^-p final state: via production and decay of $\phi(1020)$ resonance (left), and also via production and decay of $\Lambda(1520)$ and Σ^* resonances (right).

CHAPTER 2

THEORY

2.1 INTRODUCTION TO THEORY

The study of $\gamma p \rightarrow \phi p$ is important for many reasons. At high energy regime ($W \geq 10$ GeV) it is used to study the Pomeron exchange dynamics. But at relatively low energies ($W < 5$ GeV) only Pomeron exchange mechanism is not enough to describe the data. Here other mechanisms, such as meson exchange, must be considered in addition to the first, to obtain theory and data agreement. At low energies this process can be used to study the structure of baryon resonances and to search for missing resonances.

The ϕ meson mostly consists of strange quarks, i.e. $s\bar{s}$. By OZI rule [12] its production must be suppressed if the entrance channel does not have strange quarks. But there was observed a significant violation of this rule in some experiments with nucleons. So the ϕ photoproduction is also a good process to study the strange content of the nucleons.

According to [13],[14], in diffractive region, the main contribution in non-strange amplitude of ϕ photoproduction is from Pomeron exchange amplitude (Figure 4(a)) and π and η pseudoscalar meson exchange amplitudes (Figure 4(b)). At high momentum transfers the main contribution is from excitation of nucleon resonances.

In diffractive amplitude there can also be some contribution from other trajectories associated with a scalar meson and f'_2 -meson, glueball or some other exotic channels. The small contributions from these channels can be determined only from comparisons with data and are not so well understood yet.

The $g_{\eta NN}$ and $g_{\phi NN}$ coupling constants are determined differently in different analysis. In Ref. [15] the parameters of Pomeron exchange, pseudoscalar η meson exchange and ϕ radiation mechanism (Figure 4) are varied to fit the data.

In Titov et al. papers ([13],[14]) the coupling constants are estimated theoretically. The analyses also include the $f'_2(1525)$ meson exchange and glueball exchange mechanisms. The photoproduction of ϕ meson is studied by analyzing three models:

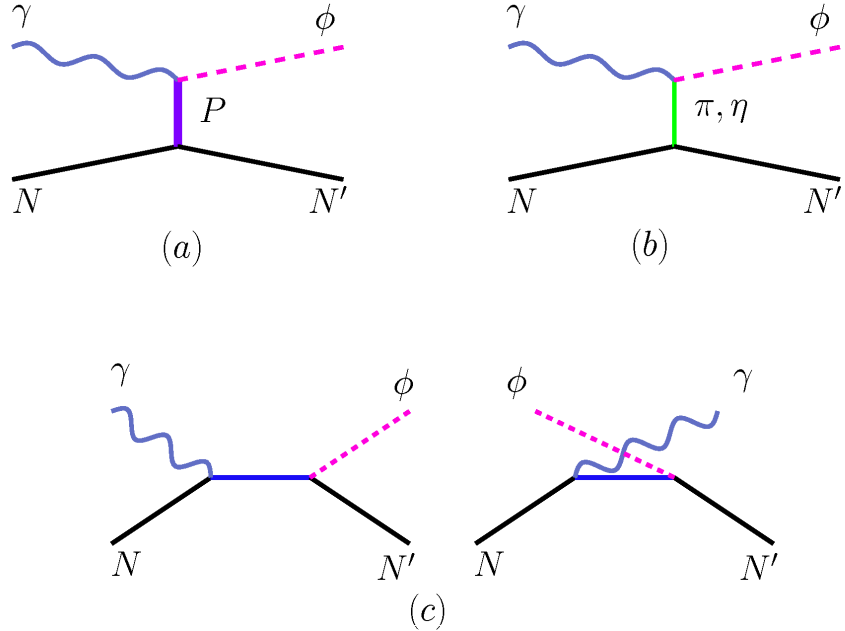


FIG. 4. Diagrams of ϕ meson production mechanisms by A.I. Titov [13]: (a) Pomeron exchange, (b) meson exchange, (c) ϕ meson radiation from nucleons.

- (model A) π, η exchange amplitude and the standard Pomeron (P_1) exchange
- (model B) model A + f'_2 meson exchange
- (model C) model A + the second Pomeron exchange (P_2) inspired by the ($J^\pi=0^+$, $M_b^2 \sim 3\text{GeV}^2$) glueball

2.2 KINEMATICAL VARIABLES

For the $\gamma N \rightarrow \phi N$ reaction S matrix ($S = \frac{1}{2}\sigma$) is related to the scattering amplitude T by

$$S_{fi} = \delta_{fi} - i(2\pi)^4 \delta^4(k + p - q - p')T_{fi} \quad (1)$$

where k, q, p and p' are the four momenta of the incoming photon, outgoing meson, initial and final nucleon, respectively. In the center-of-mass system (c.m.s.): $k=(\nu,\mathbf{k})$, $q=(E_\phi,\mathbf{q})$, $p=(E_p,-\mathbf{k})$, $p'=(E_{p'},-\mathbf{q})$.

The angle θ is the ϕ meson production angle in c.m.s. and is defined as $\cos \theta \equiv \frac{\mathbf{k} \cdot \mathbf{q}}{|\mathbf{k}| |\mathbf{q}|}$, $t=(p-p')^2 = (q-k)^2$, $s=W^2=(p+k)^2$ and $u=(p-q)^2=(k-p')^2$ are the standard Mandelstam variables.

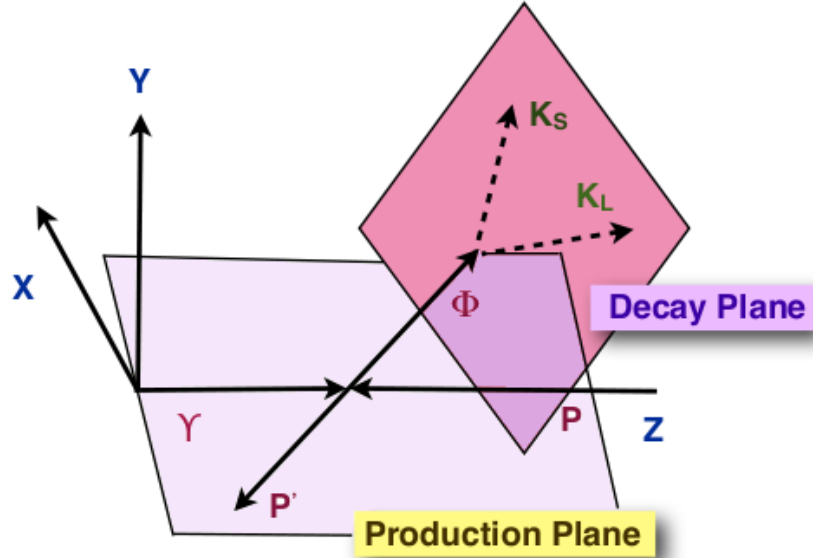


FIG. 5. The schematic pictures of the $\gamma N \rightarrow \phi N \rightarrow K_S K_L$ reaction in c.m.s.

The relation between the scattering amplitude T and the invariant amplitude I is

$$T_{fi} = \frac{I_{fi}}{(2\pi)^6 \sqrt{2E_\phi(\mathbf{q})2|\mathbf{k}|2E_p(\mathbf{p})2E_p(\mathbf{p}')}} \quad (2)$$

In the c.m.s. frame the cross section depends on invariant amplitude in the following way

$$d\sigma_{fi} = \frac{M_N^2}{2\pi^2(W^2 - M_N^2)} |I_{fi}|^2 \frac{d\mathbf{p}'}{2E_{p'}} \frac{d\mathbf{q}}{2E_\phi} \delta^4(p + k - p' - q) \quad (3)$$

The differential cross section is

$$\frac{d\sigma_{fi}}{dt} = \frac{M_N^2}{16\pi(W^2 - M_N^2)^2} \sum_{m_i, m_f, \lambda_\gamma, \lambda_\phi} |I_{m_f, \lambda_\phi; m_i, \lambda_\gamma}|^2 \quad (4)$$

where m_i, m_f are the proton spin projections in the initial and final state, and $\lambda_\gamma, \lambda_\phi$ are the helicities of the incoming photon and outgoing meson.

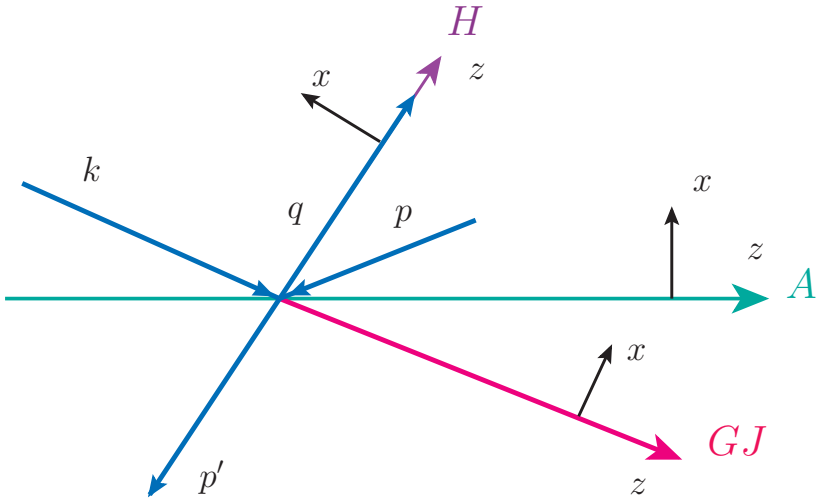


FIG. 6. Diagrammatic representation of GJ, H and A reference systems in ϕ meson rest frame, where k , q , p and p' are the four momenta of the incoming photon, outgoing meson, initial and final nucleon, respectively.

Depending on the choice of the quantization axis z , the following three reference systems can be considered (Fig.6):

- Gottfried-Jackson system (GJ) where Z is in the direction of photon in the rest frame of ϕ .
- Helicity system (H) where Z point into the direction of ϕ in the total c.m.s. or opposite to the direction of the recoiling nucleon in the rest frame of ϕ .

- Adair system (A) with Z parallel with to the photon momentum in c.m.s.

The choice of the reference system is a matter of convenience and one can change one system by another one with a rotation. The GJ system is the most common for the theoretical calculations (also used in [13]), because certain amplitudes in this frame take a simple helicity conserving form for an arbitrary production angle θ .

The decay angles Θ and Φ are defined as the polar and azimuthal angles of the direction of one of the ϕ decay particles in ϕ meson rest frame.

The vector meson decay distributions in its rest frame are determined by spin-density matrices ρ_{ij}

$$\rho_{\lambda\lambda'}^0 = \frac{1}{N} \sum_{\alpha\lambda_\gamma} I_{\alpha;\lambda,\lambda_\gamma} I_{\alpha;\lambda',\lambda_\gamma}^\dagger \quad (5)$$

$$\rho_{\lambda\lambda'}^1 = \frac{1}{N} \sum_{\alpha\lambda_\gamma} I_{\alpha;\lambda,-\lambda_\gamma} I_{\alpha;\lambda',\lambda_\gamma}^\dagger \quad (6)$$

$$\rho_{\lambda\lambda'}^2 = \frac{i}{N} \sum_{\alpha\lambda_\gamma} \lambda_\gamma I_{\alpha;\lambda,-\lambda_\gamma} I_{\alpha;\lambda',\lambda_\gamma}^\dagger \quad (7)$$

$$\rho_{\lambda\lambda'}^3 = \frac{1}{N} \sum_{\alpha\lambda_\gamma} \lambda_\gamma I_{\alpha;\lambda,\lambda_\gamma} I_{\alpha;\lambda',\lambda_\gamma}^\dagger \quad (8)$$

where α includes the polarizations of the initial and final baryons and N is the normalization factor

$$N = \frac{1}{N} \sum_{\alpha\lambda_\gamma} |I_{\alpha;\lambda,\lambda_\gamma}|^2 \quad (9)$$

The $\phi \rightarrow a + b$ decay angular distribution W is defined as

$$\frac{dN}{d\cos\Theta d\Phi} = W(\cos\Theta, \Phi) = \frac{3}{4\pi} \sum_{\lambda,\lambda'} D_{\lambda,\lambda_{ab}}^{1\star}(\Phi, \Theta, -\Phi) \rho_{\lambda\lambda'} D_{\lambda',\lambda_{ab}}^1(\Phi, \Theta, -\Phi) \quad (10)$$

In $\phi \rightarrow K_S K_L$, $\lambda_{ab} = \lambda_a - \lambda_b = 0$ and

$$W(\cos\Theta, \Phi) = \frac{3}{4\pi} \sum_{\lambda,\lambda'} D_{\lambda,0}^{1\star}(\Phi, \Theta, -\Phi) \rho_{\lambda\lambda'} D_{\lambda',0}^1(\Phi, \Theta, -\Phi) \quad (11)$$

where Wigner rotation functions are

$$D_{l0}^1(\Phi, \Theta, -\Phi) = \frac{-l}{\sqrt{2}} \sin \Theta e^{-il\Phi} \quad (12)$$

$$D_{0l}^1(\Phi, \Theta, -\Phi) = \frac{l}{\sqrt{2}} \sin \Theta e^{il\Phi} \quad (13)$$

$$D_{00}^1(\Phi, \Theta, -\Phi) = \cos \Theta \quad (14)$$

$$D_{ll'}^1(\Phi, \Theta, -\Phi) = \frac{l}{2}(1 + ll' \cos \Theta) e^{-i(l-l')\Phi} \quad (15)$$

for $l, l' = \pm 1$.

$$\begin{aligned} W(\cos \Theta, \Phi) = & \frac{3}{4\pi} \left(\frac{1}{2} (\rho_{11} + \rho_{-1-1}) \sin^2 \Theta + \rho_{00} \cos^2 \Theta \right. \\ & + \frac{1}{\sqrt{2}} (-\Re \rho_{10} + \Re \rho_{-10}) \sin 2\Theta \cos \Phi \\ & + \frac{1}{\sqrt{2}} (\Im \rho_{10} + \Im \rho_{-10}) \sin 2\Theta \sin \Phi \\ & \left. - \Re \rho_{1-1} \sin^2 \Theta \cos 2\Phi + \Im \rho_{1-1} \sin^2 \Theta \sin 2\Phi \right) \end{aligned} \quad (16)$$

In the case of unpolarized photon beam

$$\begin{aligned} W^0(\cos \Theta, \Phi) = & \frac{3}{4\pi} \left(\frac{1}{2} (1 - \rho_{00}^0) + \frac{1}{2} (3\rho_{00}^0 - 1) \cos^2 \Theta \right. \\ & \left. - \sqrt{2} \Re \rho_{10}^0 \sin 2\Theta \cos \Phi - \rho_{1-1}^0 \sin^2 \Theta \cos 2\Phi \right) \end{aligned} \quad (17)$$

Inregrating (17) over azimuthal angle Φ one obtains

$$W^0(\cos \Theta) = \frac{3}{2} \left(\frac{1}{2} (1 - \rho_{00}^0) \sin^2 \Theta + \rho_{00}^0 \cos^2 \Theta \right) \quad (18)$$

And if one integrates (17) over angle Θ

$$W^0(\Phi) = \frac{1}{2\pi} (1 - 2\Re \rho_{1-1}^0 \cos 2\Phi) \quad (19)$$

2.3 THE DIFFRACTIVE AMPLITUDES

2.3.1 Pomeron exchange amplitudes

There are two models describing Pomeron exchange process in photoproduction of vector mesons. The vector meson dominance model (VDM) (Fig.7(a)) assumes that the incoming photon first converts into a vector meson which interacts to the nucleon by a Pomeron exchange [17, 18]. In [13, 14], Donnachie - Landshoff (DL) model [19] is used to find the Pomeron exchange amplitude. According to this model the incoming photon splits into quark and antiquark pair, interacts with the nucleon by a Pomeron and then combines into the final vector meson (Fig.7(b)). It is assumed that the pomeron behaves like a C=+1 isoscalar photon. The high energy data can be described by Pomeron trajectory with $\alpha(0) \sim 1.08$ intercept.

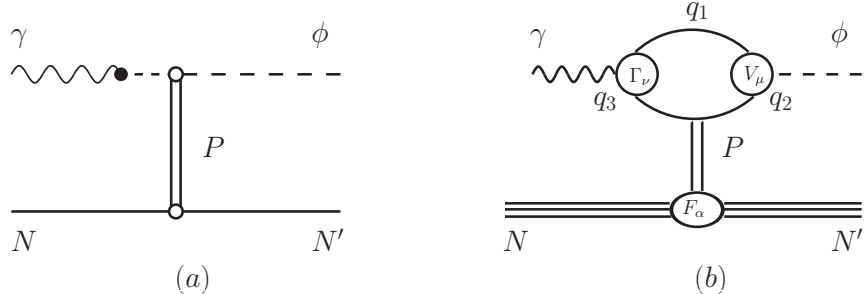


FIG. 7. Pomeron exchange models for ϕ meson production: (a) VDM model, (b) DL model [13].

In [14], using the factorized DL model, the invariant amplitude is expressed as

$$I_{fi}^P = -M_P(s, t)\varepsilon_\mu^\star(\lambda_\phi)\bar{u}_f h_P^{\mu\nu} u_i \varepsilon_\nu(\lambda_\gamma) \quad (20)$$

where:

$u = u_m(p)$ – is the Dirac spinor of the nucleon,

$\varepsilon_\nu(\gamma)$ – is the polarization vector of photon,

$\varepsilon_\mu(\phi)$ – is the polarization vector of ϕ meson.

By Regge parametrization

$$M_P(s, t) = C_P F_1(t) F_\phi(t) \frac{1}{s} \left(\frac{s}{s_P} \right)^{\alpha_P(t)} e^{-i(\pi/2)\alpha_P(t)} \quad (21)$$

where $F_1(t)$ is the electromagnetic form factor of the nucleon and $F_\phi(t)$ is the form factor of the vector-meson-photon-Pomeron coupling. From [19] it follows that

$$F_1(t) = \frac{4M_N^2 - 2.8t}{(4M_N^2 - t)[1 - \frac{t}{0.7}]^2} \quad (22)$$

$$F_\phi(t) = \frac{2\mu_0^2}{(1 - \frac{t}{M_\phi^2})(2\mu_0^2 + M_\phi^2 t)} \quad (23)$$

$$\alpha_P(t) = 1.08 + 0.25t \quad (24)$$

$$C_P = \frac{6g^2\sqrt{4\pi\alpha_{em}}}{\gamma_\phi} \quad (25)$$

here γ_ϕ is the ϕ meson decay constant $2\gamma_\phi = 13.13$, $\alpha_{em} = \frac{e^2}{4\pi}$ and $g^2 \equiv g_{P_{ss}} \cdot g_{P_{qq}}$. $g_{P_{ss}}$ and $g_{P_{qq}}$ describe the Pomeron couplings with the strange quarks in ϕ meson and the light quarks in proton. Fitting the high energy data for vector mesons, parameters $\mu_0^2 = 1.1 GeV^2$, $s_P = 4 GeV^2$, $g_{P_{qq}} = 4.1$, $g_{P_{ss}} = 3.22$ were obtained.

From the Fig.7(b) follows

$$h_P^{\mu\nu} = \not{k} \left(g^{\mu\nu} - \frac{q^\mu q^\nu}{q^2} \right) - \gamma^\nu \left(k^\mu - \frac{q^\mu k \cdot q}{q^2} \right) - q^\nu \left(\gamma^\mu - \frac{q^\mu q^\nu}{q^2} \right) \quad (26)$$

In this equation the term that is proportional to k^ν does not have contribution, and the last term violates gauge invariance. To make it invariant the following gauge transformation is applied in [14]

$$q^\nu \rightarrow \bar{q}^\nu = q^\nu - \bar{p}^\nu \frac{k \cdot q}{\bar{p} \cdot k} \quad (27)$$

Using this transformation, the vertex has the following form

$$\Gamma_{fi}^P = \bar{u}_f \not{k} u_i (\varepsilon_{\lambda_\phi}^\star \cdot \varepsilon_{\lambda_\gamma}) - \bar{u}_f \not{\gamma}_{\lambda_\gamma} u_i (\varepsilon_{\lambda_\phi}^\star \cdot k) - \bar{u}_f \not{\gamma}_{\lambda_\phi}^\star u_i \left(\varepsilon_{\lambda_\gamma} \cdot q - \frac{(\varepsilon_{\lambda_\gamma} \cdot \bar{p})(k \cdot q)}{\bar{p} \cdot k} \right) \quad (28)$$

Here \bar{p} must be fixed. It is done using Pomeron analogy to two gluons [22, 23, 24].

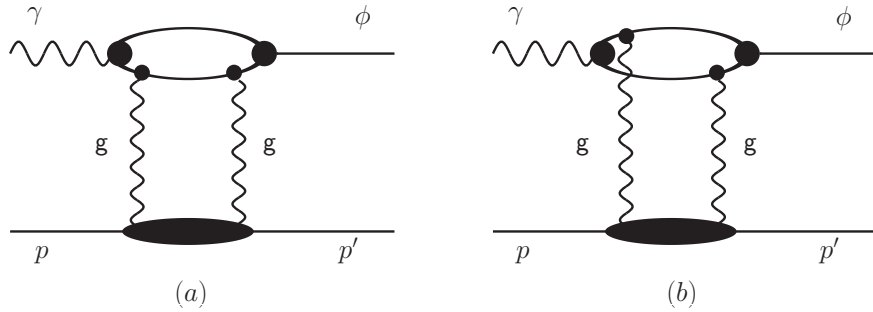


FIG. 8. Two gluon exchange mechanism for vector meson photoproduction [14].

To obtain gauge invariance, besides the two gluon interaction with the same quark (Fig.8(a)), must be taken into account the gluons interaction with different quarks (Fig.8(b)). In that case the amplitude obtains an additional term $\bar{u}(p') \not{\gamma}_{\lambda_\gamma} u(p_1) \cdot \bar{u}(p_1) \not{\gamma}_{\lambda_\phi}^\star u(p)$, where p_1 is the momentum of the quark in the intermediate state. At high energy limit and at small momentum transfers $p' \simeq p_1 \simeq p$, $\bar{u}(p') \gamma_\alpha u(p) \simeq 2p_\alpha$ and the vertex function is

$$\Gamma_{fi}^{2g} \sim (k \cdot p)(\varepsilon_{\lambda_{phi}}^\star \cdot \varepsilon_{\lambda_{gamma}}) - (\varepsilon_{\lambda_{gamma}} \cdot p)(\varepsilon_{\lambda_{phi}}^\star \cdot k) - (\varepsilon_{\lambda_{phi}}^\star \cdot p) \left(\varepsilon_{\lambda_{gamma}} \cdot q - \frac{(\varepsilon_{\lambda_{gamma}} \cdot \bar{p})(k \cdot q)}{\bar{p} \cdot k} \right) \quad (29)$$

For low energies the choice for \bar{p} is $\frac{1}{2}(p + p')$.

2.3.2 Pseudoscalar meson exchange amplitudes

There are two models which can be used to find the pseudoscalar meson exchange amplitude:

1. one-boson-approximation (OBA) model [13, 14, 15, 26, 27]
2. Regge model [28, 29]

According to [14], using OBA model the effective Lagrangians are:

$$\mathcal{L}_{\phi\gamma\varphi} = \frac{eg_{\phi\gamma\varphi}}{M_\phi} \epsilon^{\mu\nu\alpha\beta} \partial_\mu \phi \partial_\nu A_\beta \varphi \quad (30)$$

$$\mathcal{L}_{\varphi NN} = -ig_{\pi NN} \bar{N} \gamma_5 \tau_3 N \pi^0 - ig_{\eta NN} \bar{N} \gamma_5 N \eta \quad (31)$$

where A_β is the photon field and φ is either π^0 or η meson. The invariant amplitude for the pseudoscalar meson exchange is

$$I_{fi}^{ps} = - \sum_{\varphi=\pi\eta} \frac{iF_{\varphi NN} F_{\phi\gamma\varphi}(t)}{t - M_\varphi^2} \frac{eg_{\phi\gamma\varphi} g_{\varphi NN}}{M_\phi} \bar{u}_{m_f}(p') \gamma_5 u_{m_i}(p) \epsilon^{\mu\nu\alpha\beta} q_\mu k_\alpha \varepsilon_\nu^\star(\phi) \varepsilon_\beta(\gamma) \quad (32)$$

According to Ref.[30]

$$F_{\varphi NN}(t) = \frac{\Lambda_\varphi^2 - M_\varphi^2}{\Lambda_\varphi^2 - t} \quad F_{\phi\gamma\varphi}(t) = \frac{\Lambda_{\phi\gamma\varphi}^2 - M_\varphi^2}{\Lambda_{\phi\gamma\varphi}^2 - t} \quad (33)$$

Here, from $NN\varphi$ vertex coupling constants $g_{\pi NN} = 13.26$ and $g_{\eta NN} = 3.527$, and from $\phi\gamma\varphi$ vertex, using the decay widths

$$\Gamma(\phi \rightarrow \gamma\pi^0) = (5.80 \pm 0.58) \times 10^{-6} GeV \quad (34)$$

$$\Gamma(\phi \rightarrow \gamma\eta) = (5.56 \pm 0.26) \times 10^{-5} GeV \quad (35)$$

where the coupling constants $g_{\phi\gamma\pi} = -0.141$, $g_{\phi\gamma\eta} = -0.707$.

The Λ parameters for π^0 exchange are obtained from ω photoproduction analysis [31, 30] : $\Lambda_\pi = 0.6 GeV^2$, $\Lambda_\eta = 0.9 GeV^2$, $\Lambda_{\phi\gamma\pi} = 0.6 GeV^2$ and $\Lambda_{\phi\gamma\eta} = 1.0 GeV^2$.

2.3.3 f'_2 meson and glueball exchange

Both f'_2 meson and glueball exchanges are possible in ϕ meson photoproduction, thus their contribution must be included in total amplitude. The effective Lagrangians for this two trajectories are the following:

$$\mathcal{L}_{0+} = \frac{1}{4}g_{\alpha\beta}(\Lambda^{\alpha\beta} + \Lambda^{\beta\alpha})\xi \quad (36)$$

$$\mathcal{L}_{2+} = \frac{1}{4}g_{\alpha\beta}(\Lambda^{\alpha\beta} + \Lambda^{\beta\alpha})\xi_{\alpha\beta} + (\Lambda^{\alpha\beta} - \Lambda^{\beta\alpha})\xi_{\alpha\beta} \quad (37)$$

where

$$\Lambda^{\alpha\beta} = \partial_\mu\phi_1^\alpha\partial^\mu\phi_2^\beta + \partial^\alpha\phi_1^\mu\partial^\beta\phi_2_\mu - \partial^\alpha\phi_1^\mu\partial_\mu\phi_2^\beta - \partial_\mu\phi_1^\alpha\partial^\beta\phi_2^\mu \quad (38)$$

The vertices are

$$h_{0+}^{\mu\nu} = g^{\mu\nu}k \cdot q - k^\mu q^\nu \quad (39)$$

$$h_{2+}^{\mu\nu} = h_{0+}^{\mu\nu} - 2i\sigma_{\alpha\beta}[g^{\alpha\mu}g^{\beta\nu}k \cdot q + q^\alpha k^\beta g^{\mu\nu} + g^{\alpha\nu}q^\beta k^\mu + g^{\beta\mu}k^\alpha q^\nu] \quad (40)$$

The scalar function for $R = (f'_2, \text{glueball})$ is

$$M_R(s, t) = C_R F_1(t) F_\phi(t) \frac{1}{N_R} \left(\frac{s}{s_R} \right)^{\alpha_R(t)} \frac{\eta_R(1 + e^{-i\pi\alpha_R(t)})\pi\alpha'_R}{2\sin(\pi\alpha_R)\Gamma(\alpha_R(t))} \quad (41)$$

Here in C_P instead of g_P is g_R . $N_{2+} \simeq 2sM_\phi$, $N_{0+} \simeq M_N M_\phi^2$. From [28] $\alpha_{f'_2} = 0.55 + 0.7t$ and $s_{f'_2} = 1\text{GeV}^2$. For the glueball trajectory, from [32] $\alpha_{gl} = -0.75 + 0.25t$ and $s_{gl} = 4$.

The η_R and g_R parameters are obtained making the theoretical models fit the existing data for unpolarized total cross section. $g_{f'_2} = 1.87$, $\eta_{f'_2} = +1$; $g_{gl} = 7.66$, $\eta_{gl} = -1$.

2.4 BARYON AND BARYON RESONANCE EXCHANGE

2.4.1 Baryon resonance exchange

The baryon resonance exchange is believed to be the main mechanism for the backward angle ϕ photoproduction. In [14] an effective Lagrangian approach is used, developed for ω -meson photoproduction, to describe this processes. It includes all known isospin $I=1/2$ nucleon resonances listed in PDG [33]: $P_{11}(1440)$, $D_{13}(1520)$, $S_{11}(1535)$, $S_{11}(1650)$, $D_{15}(1675)$, $F_{15}(1680)$, $D_{13}(1700)$, $P_{11}(1710)$, $P_{13}(1720)$, $F_{17}(1990)$, $D_{13}(2080)$, $G_{17}(2190)$.

For N^* with $J^P = \frac{1}{2}^\pm, \frac{3}{2}^\pm, \frac{5}{2}^\pm, \frac{7}{2}^\pm$, the effective Lagrangians are

$$\mathcal{L}_{\gamma NN^*}^{\frac{1}{2}^\pm} = \frac{eg_{\gamma NN^*}}{2M_{N^*}} \bar{\psi}_{N^*} \Gamma^{(\pm)} \sigma_{\mu\nu} F^{\mu\nu} \psi_N + \text{h.c.} \quad (42)$$

$$\mathcal{L}_{\gamma NN^*}^{\frac{3}{2}^\pm} = i \frac{eg_{\gamma NN^*}}{M_{N^*}} \bar{\psi}_{N^*}^\mu \gamma_\lambda \Gamma^{(\mp)} F^{\lambda\mu} \psi_N + \text{h.c.} \quad (43)$$

$$\mathcal{L}_{\gamma NN^*}^{\frac{5}{2}^\pm} = \frac{eg_{\gamma NN^*}}{M_{N^*}^2} \bar{\psi}_{N^*}^{\mu\alpha} \gamma_\lambda \Gamma^{(\pm)} (\partial_\alpha F^{\lambda\mu}) \psi_N + \text{h.c.} \quad (44)$$

$$\mathcal{L}_{\gamma NN^*}^{\frac{7}{2}^\pm} = -i \frac{eg_{\gamma NN^*}}{M_{N^*}^3} \bar{\psi}_{N^*}^{\mu\alpha\beta} \gamma_\lambda \Gamma^{(\mp)} (\partial_\beta \partial_\alpha F^{\lambda\mu}) \psi_N + \text{h.c.} \quad (45)$$

where ψ_{N^*} , ψ_α , $\psi_{\alpha\beta}$ and $\psi_{\alpha\beta\gamma}$ are the Rarita-Schwinger spin $\frac{1}{2}$, $\frac{3}{2}$, $\frac{5}{2}$ and $\frac{7}{2}$ fields, A_μ is the photon field, and $F^{\mu\nu} = \partial^\nu A^\mu - \partial^\mu A^\nu$. $\Gamma^+ = 1$ ($\Gamma^- = \gamma_5$) defines the N^* excitations with different parity.

2.4.2 Direct ϕ meson Radiation

According to [13], the effective Lagrangians for the ϕNN and γNN interactions are

$$\begin{aligned}\mathcal{L}_{\phi NN} &= -g_{\phi NN} \left(\bar{N} \gamma_\mu N \phi^\mu - \frac{\kappa_\phi}{2M_N} \bar{N} \sigma^{\mu\nu} N \partial_\nu \phi_\mu \right) \\ \mathcal{L}_{\gamma NN} &= -e \left(\bar{N} \gamma_\mu N A^\mu - \frac{\kappa_N}{2M_N} \bar{N} \sigma^{\mu\nu} N \partial_\nu A_\mu \right)\end{aligned}\quad (46)$$

where $\kappa_p = 1.79$. The amplitude is

$$\begin{aligned}I_{fi}^C &= \bar{u}_{m_f}(p') M_{\mu\nu}^C \varepsilon_{\lambda_\phi}^{\star\mu} \varepsilon_{\lambda_\gamma}^\nu u_{m_i}(p) \\ M_{\mu\nu}^C &= e g_{\phi NN} \left[\Gamma_\mu^\phi(q) \frac{\not{p}_s + M_N}{\not{p}_s^2 - M_N^2} \Gamma_\nu^\gamma(k) + \Gamma_\nu^\gamma(k) \frac{\not{p}_u + M_N}{\not{p}_u^2 - M_N^2} \Gamma_\mu^\phi(q) \right]\end{aligned}\quad (47)$$

where

$$\begin{aligned}\Gamma_\mu^\phi(q) &= \gamma_\mu - i \frac{\kappa_\phi}{2M_N} \sigma_{\mu\nu} q^\nu \\ \Gamma_\mu^\gamma(k) &= f_N \gamma_\mu + i \frac{\kappa_N}{2M_N} \sigma_{\mu\nu} k^\nu\end{aligned}\quad (48)$$

$f_p = 1$, $p_s = p + k$, $p_u = p - q$. It is theoretically estimated in [34] that $g_{\phi NN} = -0.24$, $\kappa_\phi = 0.2$

2.5 THEORETICAL RESULTS AND EXPECTATIONS

2.5.1 Unpolarized cross section

In the total cross section the main contribution is from the diffractive channels at small $|t| < 1 GeV^2$. The main contributing mechanisms are the Pomeron and pseudoscalar meson exchange mechanisms. Four models are considered:

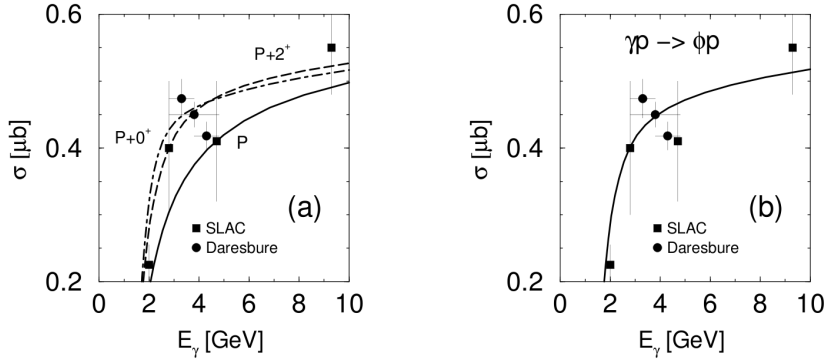


FIG. 9. The total cross section as a function of photon energy: (a) modeels A,B and C indicated by dashed, long-dashed and dot-dashed curves, (b) hybrid model [14].

- (model A) π, η exchange amplitude and the standard Pomeron (P_1) exchange
- (model B) model A + f'_2 meson exchange
- (model C) model A + the glueball trajectory
- (hybrid model) model A + small contribution from f'_2 and glueball with equal weights

In Fig.9 the theoretical results for the total cross section as a function of photon energy are plotted: (a) for the models A,B and C, and (b) for the hybrid model. Comparing the results with the existing data was found relatively good agreement for models B and C. But the precision of the data does not allow to choose which model fits the data the best, so for the further calculations was used the hybrid model, including both. The sum of the Pomeron, f'_2 and glueball amplitudes is denoted as 'diffractive'.

In Fig.10(a) the differential cross section is plotted as a function of $-t$ at $E_\gamma = 2.2$ GeV. In the calculation for the resonance channel the OZI-rule evading parameter is selected $x_{\text{OZI}}=4$. The diffractive part of the differential cross section is described by the hybrid model. It can be observed from the plot that the forward-angle photoproduction is completely defined by diffractive amplitude, the backward-angle photoproduction is well described by the resonant N^* -exchange mechanism and the central

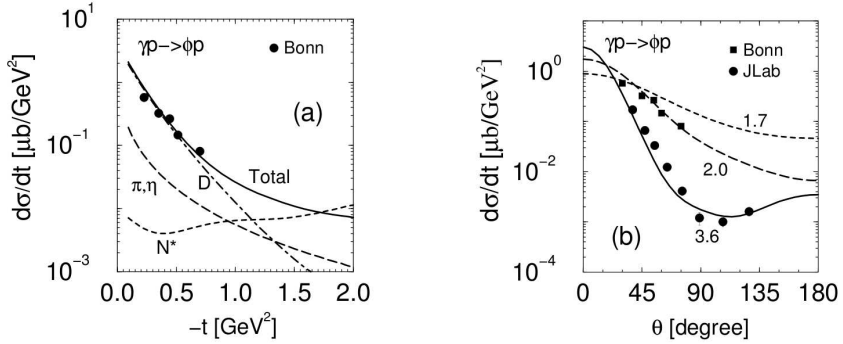


FIG. 10. (a) The differential cross section as a function of $-t$ at $E_\gamma = 2.2$ GeV for PS exchange (long-dashed), diffractive channels (dot-dashed), resonance excitation (dashed) and the total amplitude (solid). (b) The differential cross section as a function of ϕ production angle at $E_\gamma = 1.7, 2.0$ and 3.6 GeV. The data are from [35, 36], [14].

region can be described only by the sum of all the processes. The (b) plot of the same figure shows the differential cross section - production angle in c.m.s. dependence at three different photon energies. There is a pretty good agreement between theoretical results and data.

2.5.2 Spin observables

All the calculations for the spin observables are done in Gottfried-Jackson system in [14]. The model applicability at $E_\gamma \sim 2 - 3$ GeV is limited by the forward and backward photoproduction with $|t_{min}| \leq |t| \leq |t_l|$ and $|t_l| \leq |t| \leq |t_{max}|$, respectively, where $|t_l| \simeq 0.5 - 0.7 \text{ GeV}^2$, depending on energy.

For the forward angle photoproduction the scalar and pseudoscalar meson exchange amplitudes are

$$I_{m_f m_i; \lambda_\phi \lambda_\gamma}^{U^N}(t) = \begin{pmatrix} 1 \\ 2m_i \lambda_\gamma \end{pmatrix} \delta_{m_i m_f} \delta_{\lambda_\gamma \lambda_\phi} I_0^{U^N}(t) \quad (49)$$

The Pomeron exchange amplitude in GJ system has the following form

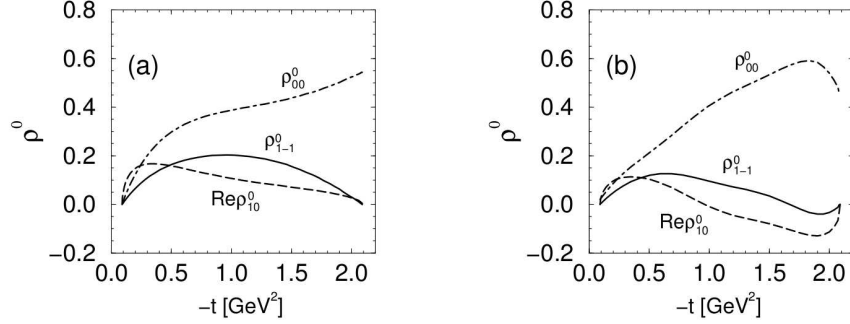


FIG. 11. The spin-density matrix elements as a function of $-t$ at $E_\gamma = 2.2$ GeV: (a) for the Pomeron exchange amplitude, (b) for the full model [14].

$$I_{fi}^P \equiv -\delta_{\lambda_\phi \lambda_\gamma} \bar{u}_f \not{u}_i + \delta_{\lambda_\phi 0} k_\gamma \bar{u}_f \not{\gamma}_\lambda u_i + \sqrt{2} \lambda_\gamma p_x \frac{k \cdot q}{2p \cdot k - k \cdot q} \bar{u}_f \not{\gamma}_{\lambda_\phi} u_i \quad (50)$$

where k_γ and p_x are the photon momentum and x component of the proton momentum. The second term in (50) describes the interaction of the photon and nucleon spins and interaction of the ϕ meson spin and the orbital momentum in the initial state. The last term describes the ϕ meson and nucleon spins interaction and the interaction of the photon spin with the orbital momentum in the final state. So the second and the last terms are responsible for the spin-flip transitions $\lambda_\gamma \rightarrow \lambda_\phi = 0$. The most contribution is from the second term and it is estimated as

$$\begin{aligned} \rho_{00}^0 &\simeq \frac{k_\gamma^2(|t| + 2p_x^2)}{\bar{s}^2} \\ \bar{s}^2 &= (s - M_N^2)^2 \left(1 - \frac{M_\phi^2 + |t|}{s - M_N^2}\right) \end{aligned} \quad (51)$$

The double spin-flip transition $\lambda_\gamma \rightarrow \lambda_\phi = -\lambda_\gamma$ is connected with the photon spin interaction with the orbital momentum. It generates ρ_{1-1}^0 , which is defined by the interference of the first and the last terms

$$\rho_{1-1}^0 \simeq \frac{p_x^2(M_\phi^2 + |t|)}{\bar{s}^2} \quad (52)$$

In Fig.11 the spin-density matrix ρ^0 elements are plotted as function of $-t$ for $E_\gamma = 2.2$ GeV. This matrix defines the ϕ meson decay product particles angular

distribution in reaction with unpolarized photons. At forward angle photoproduction the spin-density matrix elements are determined by Pomeron exchange processes, but at high momentum transfers mostly the resonance excitations are important.

In Fig.12 the angular distribution function for the unpolarized photons is plotted for three different $|t|$ values. At the small momentum transfers the ϕ mesons are produced with the spins aligned along the quantization axis z' . This is expressed in $W^0 = \sin^2 \Theta$ dependence. As the $|t|$ increases, the spin-flip processes make the produced ϕ mesons longitudinally polarized. At large momentum transfers $W^0 \simeq a + b \cos^2 \Theta$, where $a, b > 0$. The Φ dependence of the W^0 is determined only by spin-flip processes. The amplitude of the oscillations increases with increasing value of $|t|$, reaches the maximal value at $|t| \sim 0.6 \text{ GeV}^2$ and then again decreases. The spin-density matrix elements ρ_{1-1}^0 determined by the azimuthal angle dependences and mostly describe the gluon-exchange processes. At very high momentum transfers the resonant channels play the main role.

Fig.13 represents the ρ_{00}^0 and ρ_{1-1}^0 photon energy dependences at fixed $|t|=0.4 \text{ GeV}^2$ value for the Pomeron-exchange and full amplitudes. The value of ρ_{00}^0 increases with the energy, indicating the increase of longitudinally-polarized ϕ mesons with energy.

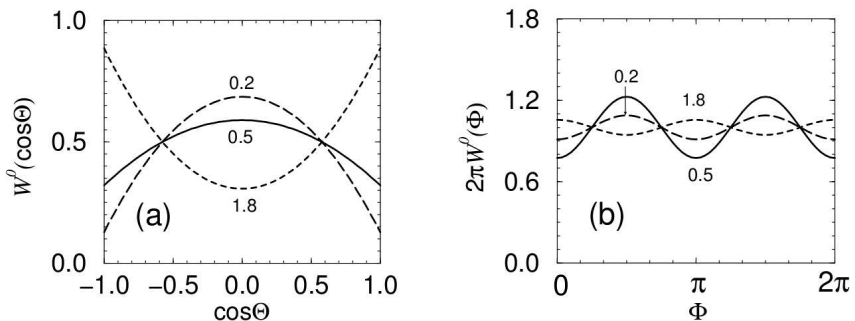


FIG. 12. Angular distribution function at $E_\gamma = 2.2 \text{ GeV}$ and $|t|=0.2,0.5$ and 1.8 GeV^2 as a function of: (a) $\cos \Theta$, (b) Φ . [14]

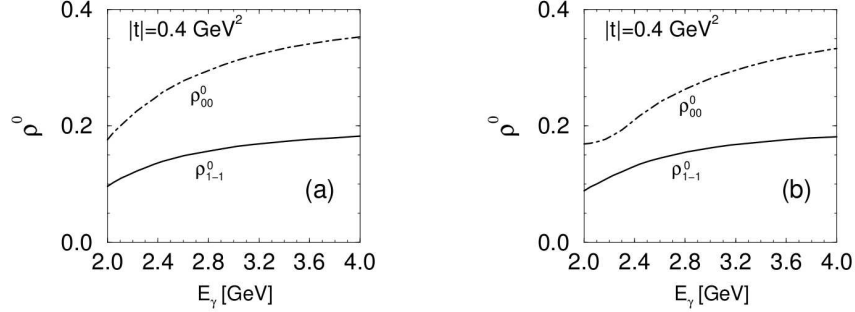


FIG. 13. Spin-density matrix elements as a function of E_γ at $|t|=0.4 \text{ GeV}^2$ for: (a) Pomeron exchange amplitude, (b) full model. [14]

2.6 SUMMARY

The ϕ meson photoproduction in diffractive regime is dominated by Pomeron exchange, π and η pseudoscalar meson exchange process and there is some contribution from exotic channels like f'_2 meson exchange, glueball exchange mechanisms. At high momentum transfers the nuclear resonance excitations start to play the dominant role and there is observed large deviation from OZI rule. The spin-dependent part in Pomeron exchange amplitude is responsible for the spin-flip transitions in ϕ photoproduction process. These transitions have large input in spin-density matrix elements and can be measured from the ϕ meson decay angular distribution data. The double spin-flip transitions are related to the ρ_{1-1}^0 spin-density matrix element and can be obtained from azimuthal angle dependence part of the angular distribution function. More available data and more precise measurements of the cross section and spin observables will allow to study the production mechanisms in more detail.

CHAPTER 3

DATA ANALYSIS

The purpose of this analysis is to study the ϕ meson production in neutral decay mode : $\gamma + p \rightarrow p + \phi \rightarrow p + K_S + K_L$. This channel has a branching fraction of approximately 34% in the total ϕ meson production. The neutral K_S has 8.953×10^{-11} s mean lifetime and is identified using its decay into $\pi^+ \pi^-$ or $\pi^0 \pi^0$ pair. The final particles were detected in CLAS. In this chapter we will describe in detail all steps performed to select data for this analysis as well as cuts and corrections applied to study ϕ meson photoproduction.

3.1 DATA SELECTION

Events were selected with three charged tracks in the final state identified as proton, π^+ and π^- . These particles were selected according to particle id assigned by SEB. To suppress accidental coincidences from different beam bunches, there was a requirement to have only one photon present in the tagger within ± 2 ns time interval between the tagger and the start counter - $|TAG_{time} - ST_{time}| < 2$ (Fig.14). This cut helps to choose the right photon for event in the case of detecting more than one photon with time close to the event start time.

There were minimal momentum cuts on protons and pions: $P_\pi > 0.1(GeV/c)$, $P_p > 0.35(GeV/c)$.

Several other cuts and corrections were applied to raw data to produce the final data set for the analysis. These cuts and corrections are discussed in detail in the following sections.

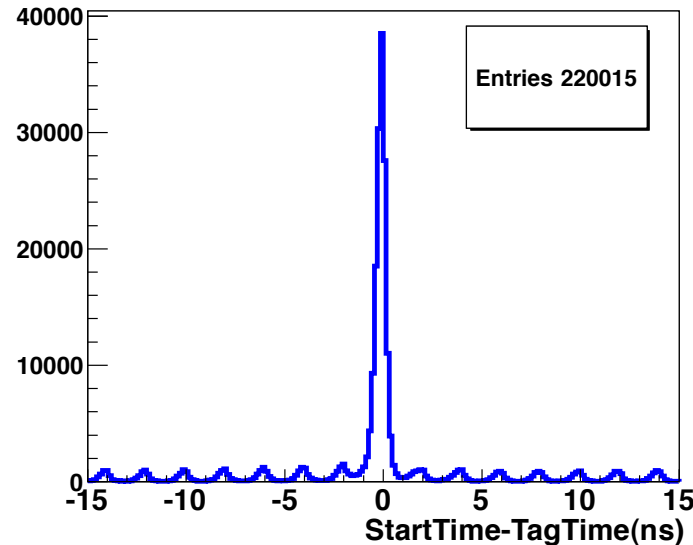


FIG. 14. The tagger time subtracted from event start time. 2 ns cut was used to select good photons.

g11 Tagger Energy Corrections
g11 Particle Energy Loss Corrections
g11 Particle Momentum Corrections
Detector Efficiency Corrections
Detector Acceptance Corrections

TABLE I. Table of corrections applied to data.

3.2 ENERGY AND MOMENTUM CORRECTIONS

Data for the analysis were corrected using the standard g11 energy and momentum correction packages. These corrections included the charged particle energy loss correction [50], tagger energy corrections, and particle momentum correction [49]. Below each of these corrections will be discussed separately.

3.2.1 Tagger Energy Corrections

In the preliminary analysis of g11 data it was observed that there is a deviation between the proton mass and the missing mass of the $\gamma p \rightarrow K^+K^-X$ reaction $\Delta M = M_X - M_{proton}$. This deviation depended on run number (Fig.15(a)). To solve the problem, the electron energy was corrected on run-by-run basis. In average, the correction factor $R = E_{corrected}/E_{initial}$ was equal to 1.005, showing that the detected beam energy was about 0.5% less than the actual one. The correction factor R depending on run number is plotted on Fig.15(b). The corrections were different for the run numbers grater than 44108, where the beam energy was higher.

The photon energy corrections were checked using $\gamma p \rightarrow \pi^+\pi^-X$ reaction. Tagger energy corrections as a function of tagger ID are plotted on Fig.16, where the red points are the corrections before electron energy corrections were applied, and the blue points correspond to the corrections after electron energies were corrected. The several shifted points correspond to the swept wires. This was taken into account during the correction. After these corrections were applied, the missing proton mass was shifted to its correct value. This can be seen from Fig.17, where the missing mass of the proton in $\gamma p \rightarrow \pi^+\pi^-X$ is plotted as a function of tagger ID.

3.2.2 Energy Loss Correction

The charged particles propagating through the detector material lose the energy on the ionization and atomic excitations. The momenta of the proton, π^+ and π^- were corrected for the energy loss using CLAS software Eloss package written by

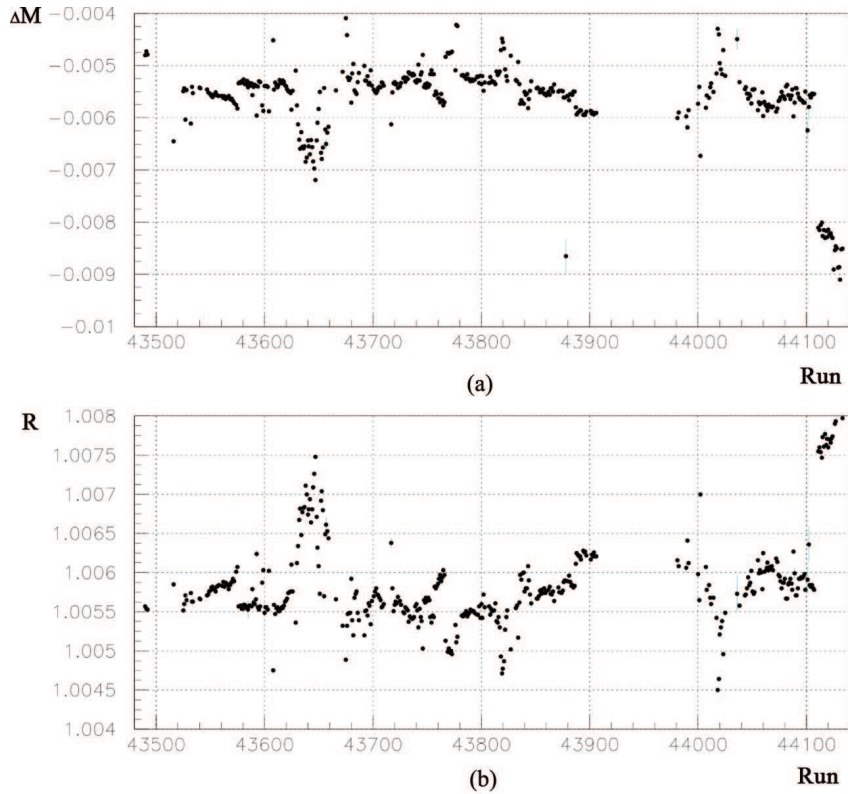


FIG. 15. (a) The missing mass shift in the reaction $\gamma p \rightarrow K^+ K^- X$, $\Delta M = M_X - M_{proton}$, (b) Beam energy correction factor $R = E_{corrected}/E_\gamma$ as a function of run number. [49]

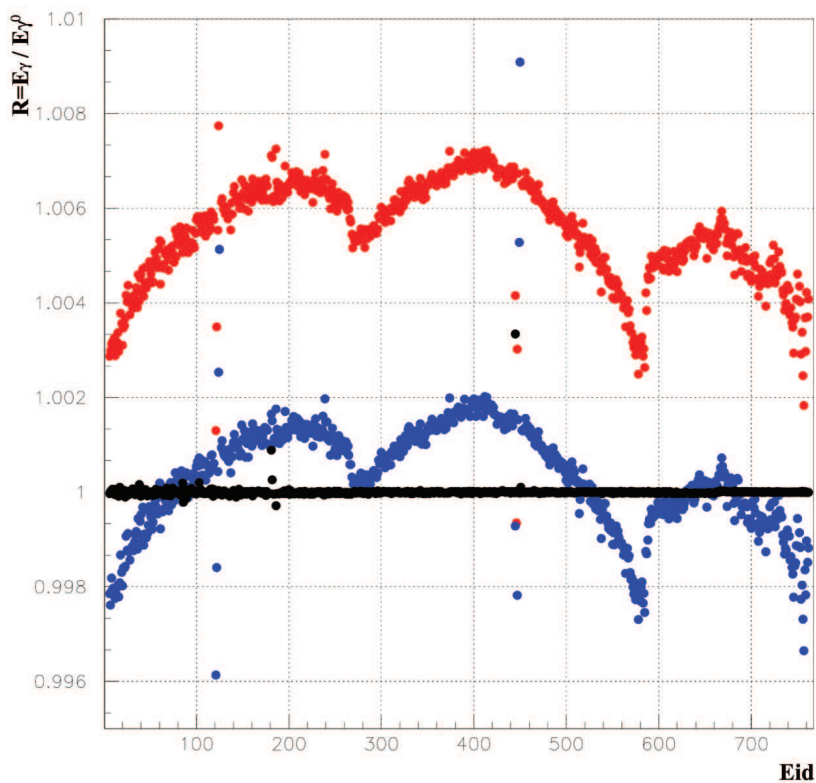


FIG. 16. Tagger energy correction $R = E_\gamma / E_{\gamma 0}$ as a function of tagger ID. The red points are the corrections before the electron energies were corrected, and the blue points show the corrections after the electron energy corrections. [49]

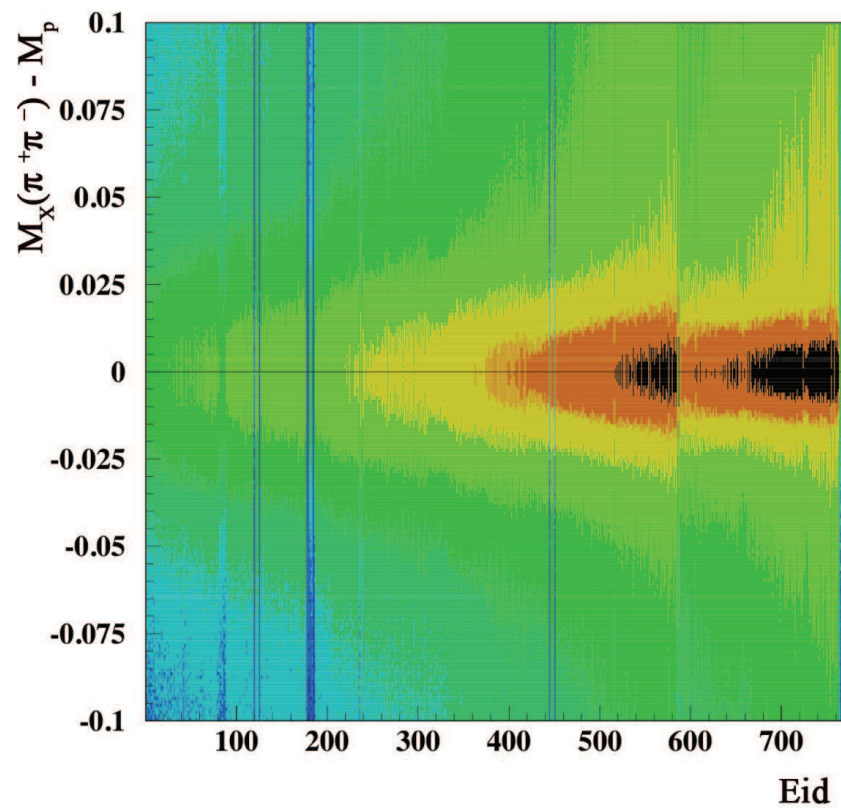


FIG. 17. The difference of the missing mass of the reaction $\gamma p \rightarrow \pi^+\pi^-X$ and the proton mass $\Delta M = M_X - M_p$ as a function of tagger ID after the tagger energy correction. [49]

E. Pasyuk [50]. This correction includes the energy loss in the target material and walls, the beam pipe, the start counter and the air between the start counter and the drift chambers in Region 1. The energy loss was estimated using the momenta and masses of the particles. This correction does not include the energy loss due to the fight of the particle in the magnetic field.

3.2.3 Momentum Corrections

These momentum corrections, obtained by V. Kubarovskiy, were based on the missing mass technique. Two reactions were used to find the corrections: $\gamma p \rightarrow \pi^+ \pi^- p$ and $\gamma p \rightarrow K^+ K^- p$. The missing masses of the proton, pions and kaons were used to correct the momenta. In this procedure only one variable ϕ was used, although it is possible to get corrections using θ , ϕ and P variables together. In this case the corrections for the θ and P variables were very small and could be neglected. The corrections were obtained for π^+ , π^- , K^+ , K^- and protons. The corrections for the π^+ , K^+ and protons were obtained from their missing mass distributions in $\gamma p \rightarrow \pi^+ \pi^- p$ reaction and for the protons - from the $\gamma p \rightarrow K^+ K^- p$ reaction. The corrections $R = P_{\text{corrected}} / P_{\text{measured}} - 1$ for these particles are plotted in Fig.18.

Using the data in these figures the momentum corrections were calculated using extrapolation method. As a function of ϕ the momentum corrections are on the order of about $\pm 1\%$. The missing mass distributions of the protons before and after the corrections are plotted in Fig.20. The missing and invariant masses of some other particles are plotted in Fig.21. After these corrections being applied the mass resolutions of particles have somewhat improved, and the missing mass values are differing from their table values not more than 1MeV.

The momentum corrections for the negative π^- and K^- were also obtained from the above mentioned two reactions and they are plotted in Fig.19.

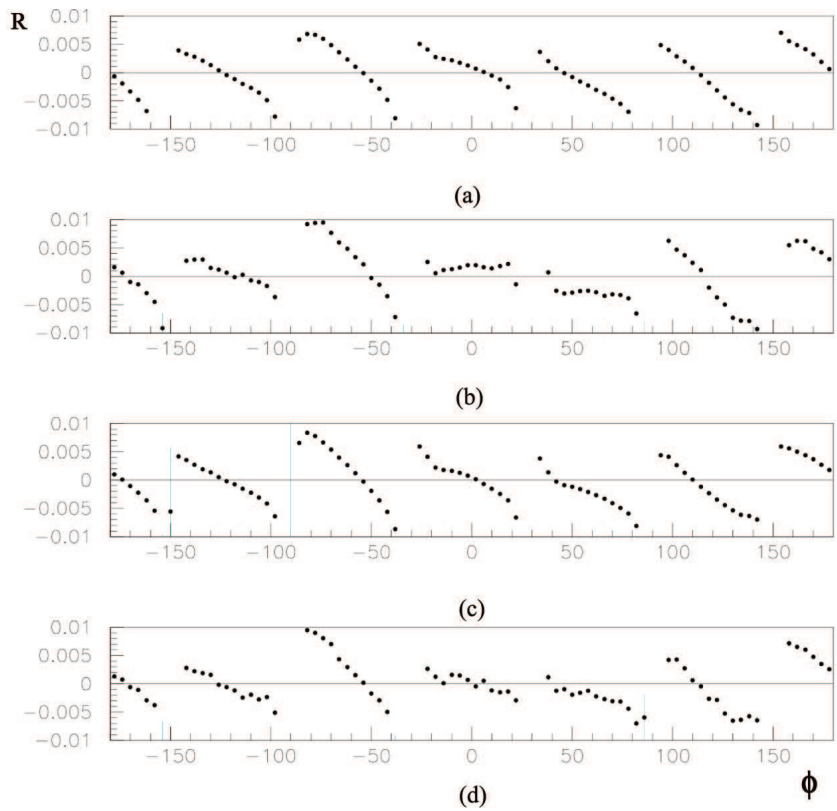


FIG. 18. Momentum corrections for positive particles (π^+, K^+ , protons) $R = P_{\text{corrected}}/P_{\text{measured}} - 1$ estimated from the missing mass distributions in: (a,b,c) $\gamma p \rightarrow \pi^+ \pi^- p$, (d) for protons from the reaction $\gamma p \rightarrow K^+ K^- p$. [49]

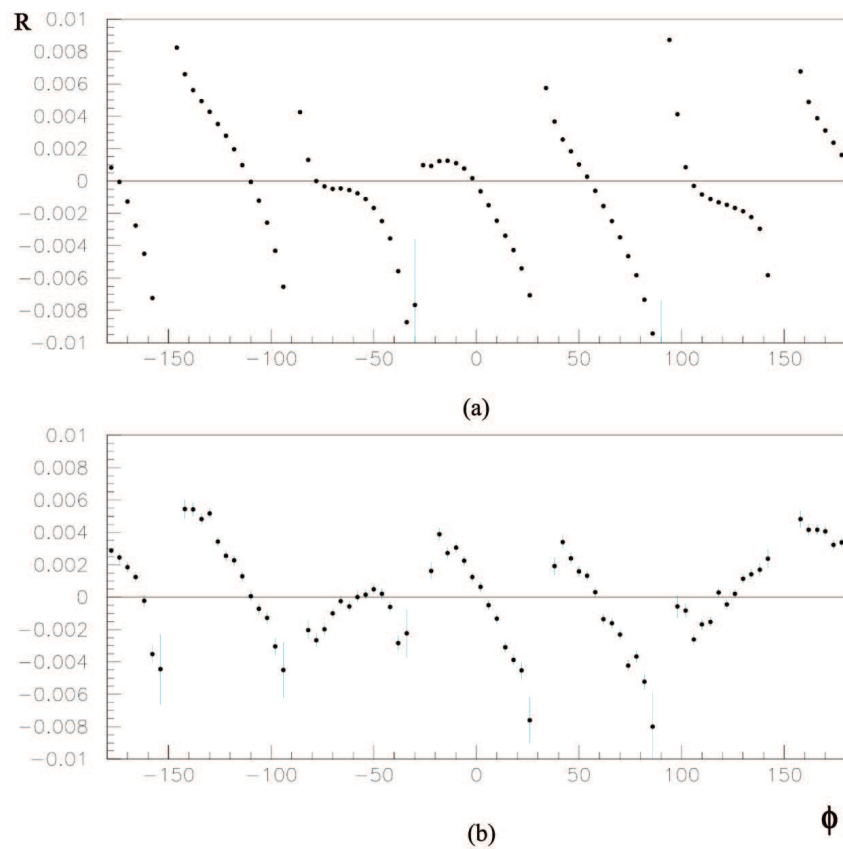


FIG. 19. Momentum corrections for negative particles (π^-, K^-)
 $R = P_{\text{corrected}}/P_{\text{measured}} - 1$. [49]

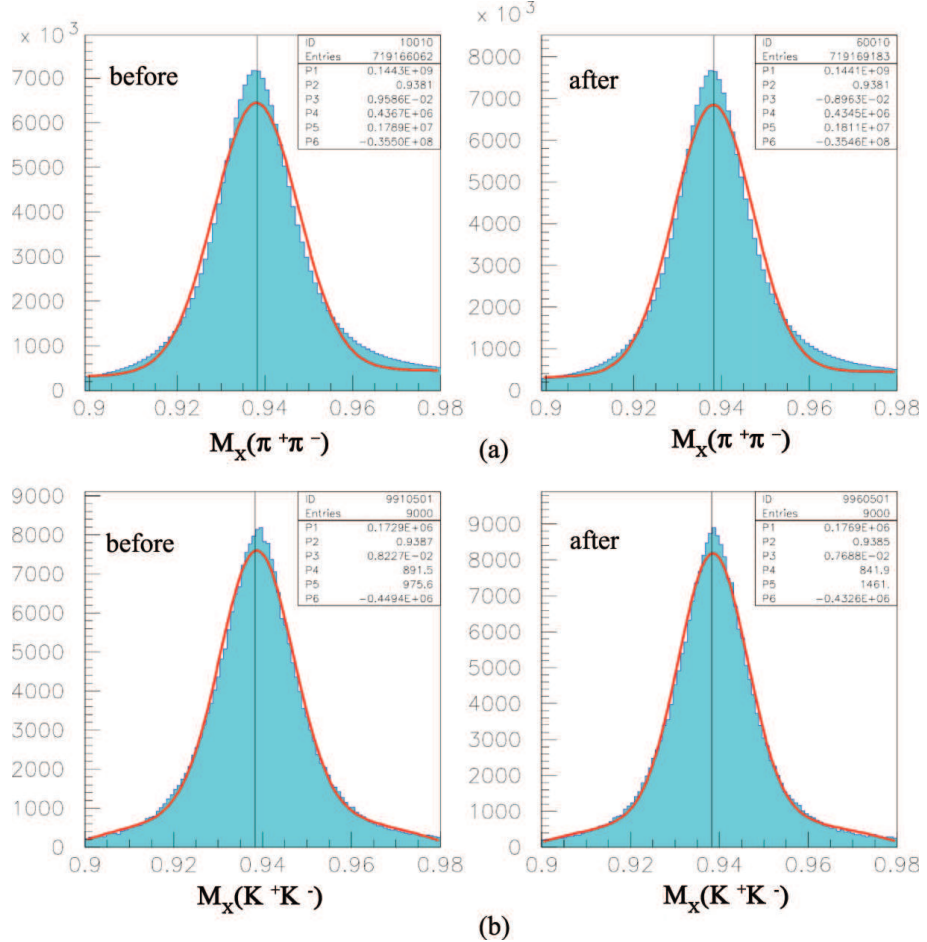


FIG. 20. The mass distributions of missed protons before and after the corrections were applied in two reactions:(a) $\gamma p \rightarrow \pi^+ \pi^- X$, (b) $\gamma p \rightarrow K^+ K^- X$. [49]

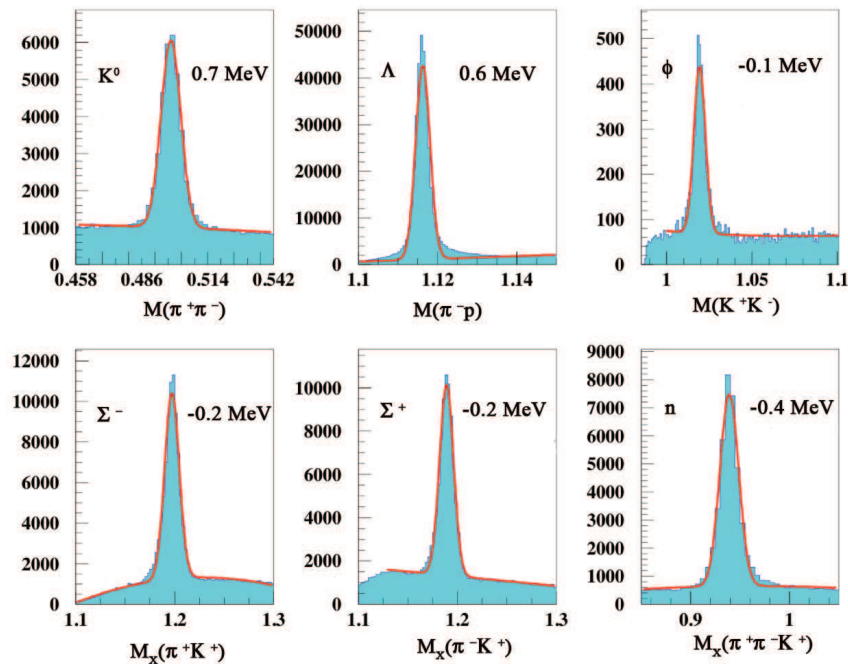


FIG. 21. Invariant and missing masses after all corrections were applied. The deviation from the table value is indicated for each distribution on the right side of the plot. [49]

3.3 THE DETECTOR EFFICIENCY CORRECTIONS

Due to the missing wires in the drift chamber or low pulse gains in phototubes because of high voltages the detector can be less efficient in some regions. To correct data for these effects we must obtain the detector efficiency for particles. In this analysis the proton, π^+ and π^- detection efficiencies were obtained using two reactions: $\gamma p \rightarrow p\pi^+\pi^-$ and $\gamma p \rightarrow p\pi^+\pi^-\pi^+\pi^-$. Events were selected based on complete exclusivity , in case if one particle is missed it is reconstructed by missing mass. The efficiencies were obtained for every θ and ϕ angle.

To obtain efficiencies for protons the available dataset is divided into the following four momentum bins: (0.35 - 0.4) GeV/c, (0.4 - 0.45) GeV/c, (0.45 - 0.55) GeV/c, > 0.55 GeV/c. For each momentum region the efficiencies are calculated using (53) and (54).

$$Ef_p = \frac{N(\gamma p \rightarrow \pi^+\pi^-p)}{N(\gamma p \rightarrow \pi^+\pi^-)p} \quad (53)$$

$$Ef_p = \frac{N(\gamma p \rightarrow \pi^+\pi^-\pi^+\pi^-p)}{N(\gamma p \rightarrow \pi^+\pi^-\pi^+\pi^-)p} \quad (54)$$

In equations (53) and (54) the protons in numerator correspond to detected proton events, and the protons in denominator are obtained from the missing mass of the reactions. In Fig.22 the θ angle is plotted versus the ϕ angle for the detected protons and for the missing protons in two reactions $(\gamma p \rightarrow \pi^+\pi^-)p$ and $(\gamma p \rightarrow \pi^+\pi^-\pi^+\pi^-)p$. Efficiencies are obtained from the ratio of histograms.

Efficiencies for positively charged pions are obtained dividing the dataset into the following four momentum regions: (0.1 - 0.15) GeV/c, (0.15 - 0.2) GeV/c, (0.2 - 0.3) GeV/c, > 0.3 GeV/c. For each momentum region efficiencies are calculated using (55) and (56).

$$Ef_{\pi^+} = \frac{N(\gamma p \rightarrow \pi^+\pi^-p)}{N(\gamma p \rightarrow \pi^-p)\pi^+} \quad (55)$$

$$Ef_{\pi^+} = \frac{N(\gamma p \rightarrow \pi^+\pi^-\pi^+\pi^-p)}{N(\gamma p \rightarrow \pi^+\pi^-\pi^-\pi^-p)\pi^+} \quad (56)$$

In equations (55) and (56) positively charged pions in the numerator correspond to the detected π^+ events, and positively charged pions in the denominator are obtained from the missing mass of reactions. In Fig.23 the θ angle is plotted versus the ϕ angle for the detected π^+ and for the missing π^+ in two reactions: $(\gamma p \rightarrow \pi^- p)\pi^+$ and $(\gamma p \rightarrow \pi^+\pi^-\pi^- p)\pi^+$. The efficiencies are obtained from the ratio of these two histograms.

Efficiencies for negatively charged pions are calculated for the same momentum regions as for positively charged pions: (0.1 - 0.15) GeV/c, (0.15 - 0.2) GeV/c, (0.2 - 0.3) GeV/c, > 0.3 GeV/c. For each momentum region efficiencies are calculated using equations (57) and (58).

$$Ef_{\pi^-} = \frac{N(\gamma p \rightarrow \pi^+\pi^- p)}{N(\gamma p \rightarrow \pi^+ p)\pi^-} \quad (57)$$

$$Ef_{\pi^-} = \frac{N(\gamma p \rightarrow \pi^+\pi^-\pi^+\pi^- p)}{N(\gamma p \rightarrow \pi^+\pi^-\pi^+ p)\pi^-} \quad (58)$$

In equations (57) and (58) the negative pions in numerator correspond to detected π^- events, and the negative pions in denominators are obtained from the missing mass of the reactions. In Fig.24 the θ angle is plotted versus the ϕ angle for the detected π^- and for the missing π^- in the two reactions $(\gamma p \rightarrow \pi^+ p)\pi^-$ and $(\gamma p \rightarrow \pi^+\pi^-\pi^+ p)\pi^-$. The efficiencies are obtained from the histogram ratios.

To include all angles there are 180 θ bins and 360 ϕ bins in all cases.

In Fig.25 (a) protons' polar Θ angles are plotted versus azimuthal angles Φ before the efficiency corrections were applied. The (b) histogram of the same figure is the vertical projection of the histogram in (a). Fig.25 (c) is the proton angular distributions plot after the efficiency corrections were applied, and (d) is projection of (c).

In Fig.26 (a) π^+ mesons' polar Θ angles are plotted versus azimuthal angles Φ before the efficiency corrections were applied. The (b) histogram of the same figure is the vertical projection of the histogram in (a). Fig.26 (c) is the positive pion angular distributions plot after the efficiency corrections were applied, and (d) is projection of (c).

In Fig.27 (a) polar Θ angles of π^+ mesons are plotted versus azimuthal angles Φ before the efficiency corrections were applied. The (b) histogram of the same figure is

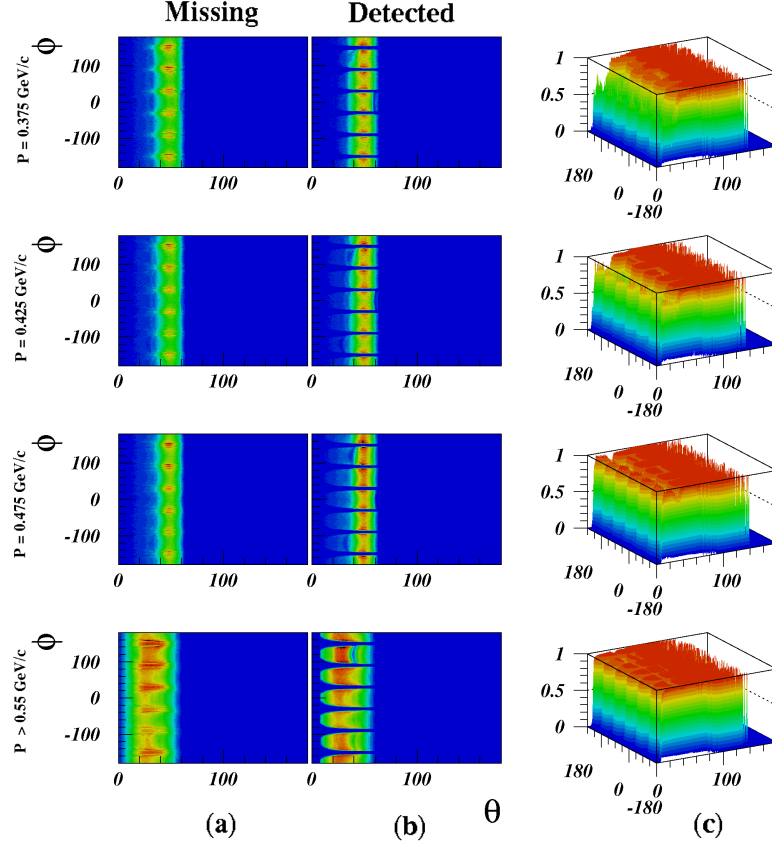


FIG. 22. The calculation of efficiency coefficients for the protons. (a) The missing protons θ angle vs ϕ angle; (b) The detected protons θ angle vs ϕ ; (c) The 3D plots of efficiency coefficients for the protons plotted versus θ and ϕ angles in different momentum ranges.

the vertical projection of the histogram in (a). Fig.27 (c) is the negative pion angular distributions plot after the efficiency corrections were applied, and (d) is projection of (c).

The holes at $\Phi = 300$ degrees (Sector 6) is because of dead drift chamber wires and scintillators, which significantly decrease the efficiency. Events from these bad paddles were cut out in data and correspondingly were excluded during the acceptance calculations.

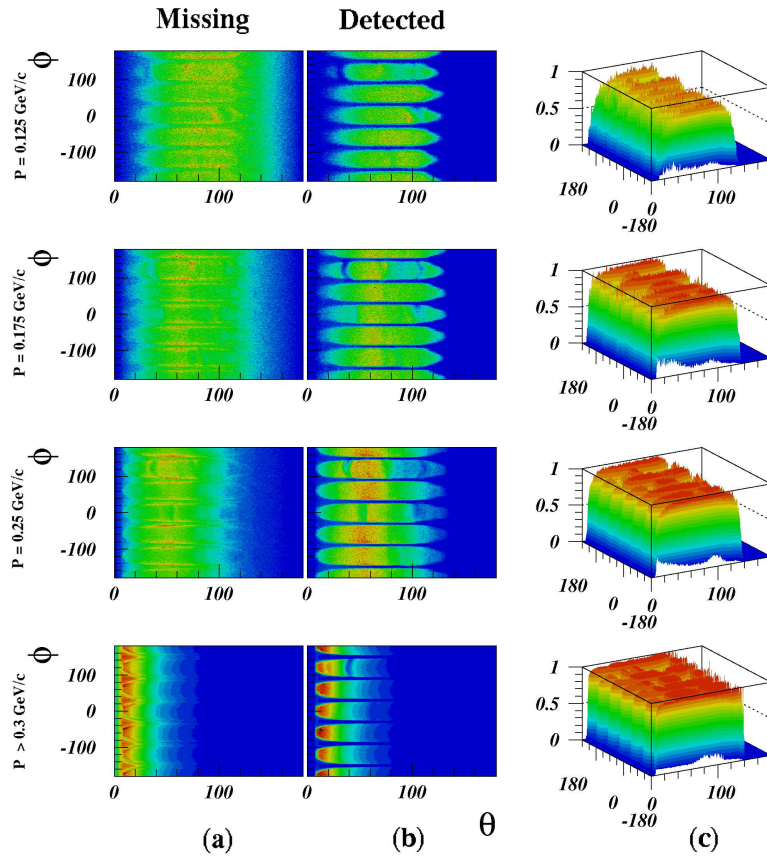


FIG. 23. The calculation of efficiency coefficients for the positive pions. (a) The missing π^+ θ angle vs ϕ angle; (b) The detected π^+ θ angle vs ϕ ; (c) The 3D plots of efficiency coefficients for the positive pions plotted versus θ and ϕ angles in different momentum ranges.

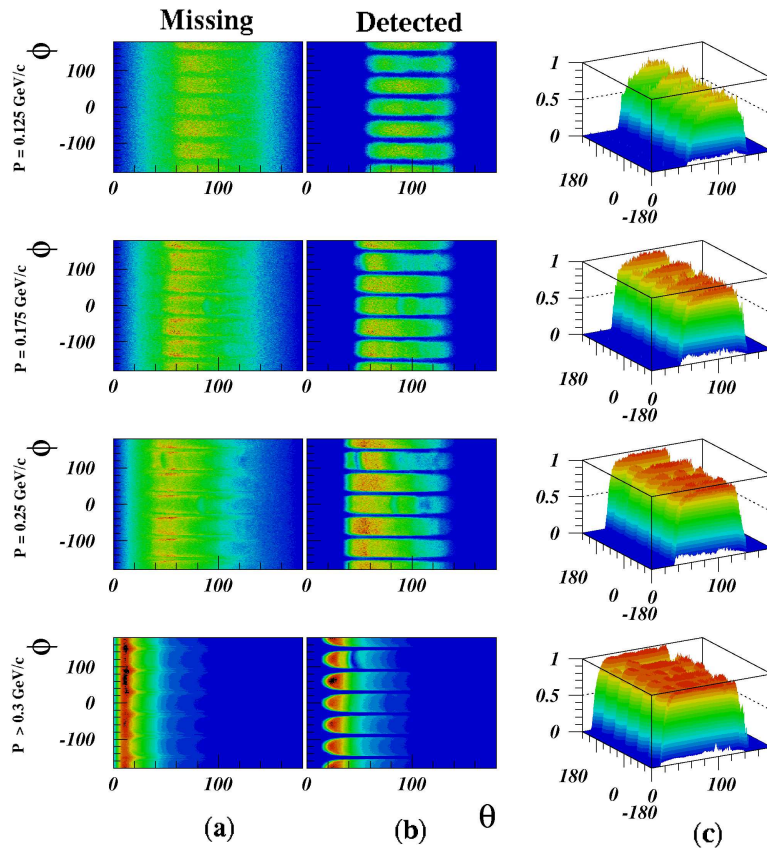


FIG. 24. The calculation of efficiency coefficients for the negative pions. (a) The missing $\pi^- \theta$ angle vs ϕ angle; (b) The detected $\pi^- \theta$ angle vs ϕ ; (c) The 3D plots of efficiency coefficients for the protons plotted versus θ and ϕ angles in different momentum ranges.

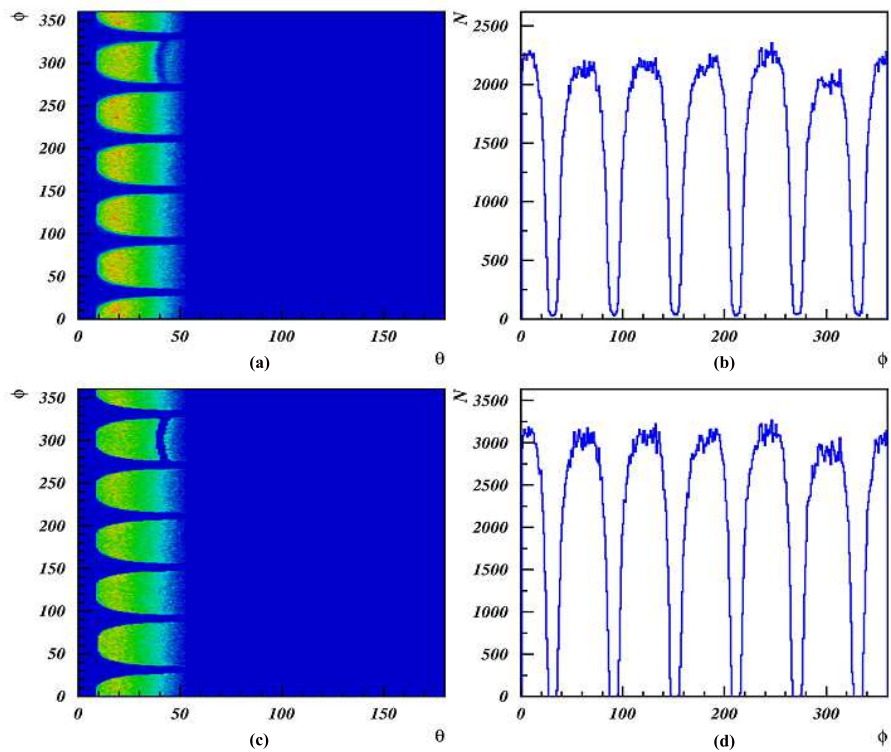


FIG. 25. Proton angular distributions:(a),(b) before efficiency corrections, (c),(d) after efficiency corrections.

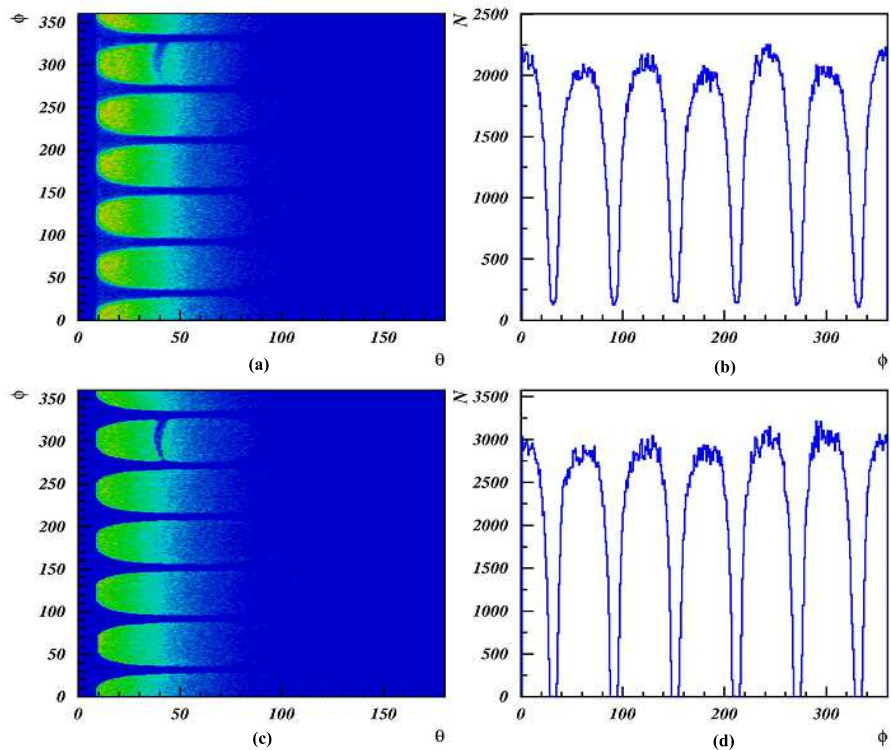


FIG. 26. π^+ meson angular distributions: (a),(b) before efficiency corrections, (c),(d) after efficiency corrections.

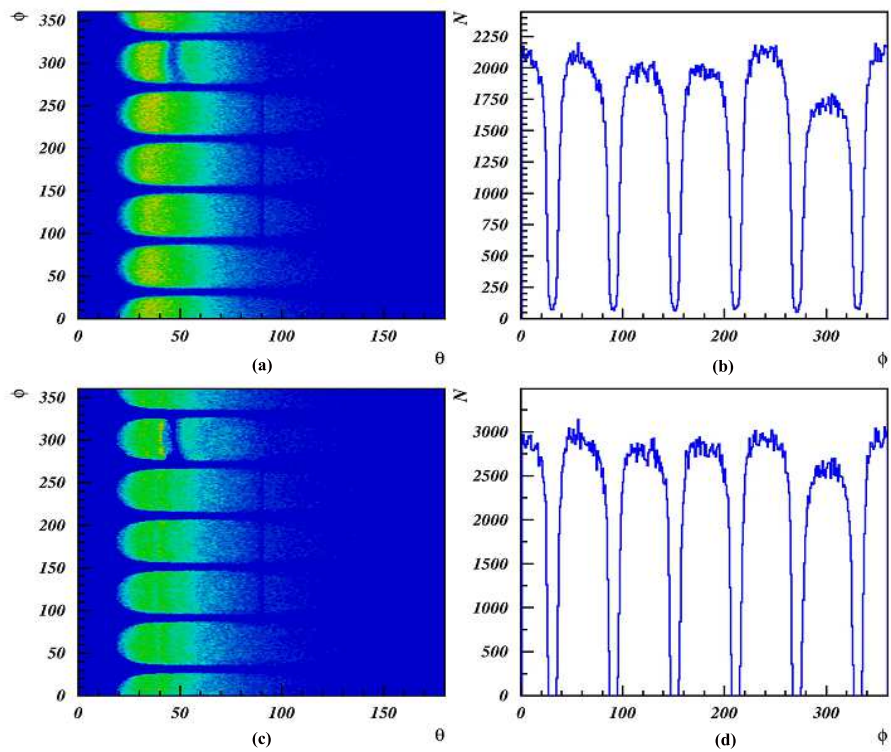


FIG. 27. π^- meson angular distributions: (a),(b) before efficiency corrections, (c),(d) after efficiency corrections.

3.4 FIDUCIAL CUTS

The fiducial cuts are applied to eliminate the detector bad regions, where the efficiency changes rapidly. For this reason an efficiency cut of 40% is applied both to data and generated events. Also we put cuts on dead scintillator paddles . The following paddles were eliminated:

Sect	SPID
1	18,26,27,33
3	11,24,25
4	26
5	20,23
6	25,30,34

TABLE II. Removed problematic scintillator paddles.

3.5 PARTICLE IDENTIFICATION

To reconstruct ϕ mesons for the analysis the neutral kaons K_S and K_L should be identified. The K_s particle is identified through its $\pi^+\pi^-$ decay mode ($\sim 68.6\%$ b.r.). The invariant mass of π^+ and π^- is taken to be the mass of $K_S \pm 2\sigma$ ($M(K_S) = 0.49765 \pm 0.008(GeV/c^2)$). The missing mass of $\gamma p \rightarrow p'\pi^+\pi^-X$ is required to be the mass of $K_L \pm 2\sigma$ ($M(K_L) = 0.49765 \pm 0.015(GeV/c^2)$). The ϕ mesons are reconstructed in the invariant mass of K_SK_L system.

Fig.30 shows the invariant mass of $\pi^+\pi^-$ system with a cut on invariant mass of K_SK_L to be less than $1.07\text{ GeV}/c^2$ (in blue), and the same distribution with an additional cut on missing mass of $\gamma p \rightarrow \pi^+\pi^-p(X)$ to be within $30\text{ MeV}/c^2$ interval around K_L mass (in red). Fig.31 shows the missing mass of $\gamma p \rightarrow \pi^+\pi^-p(X)$, requiring the invariant mass of $\pi^+\pi^-$ to be the mass of K_S . The peaks of several possible

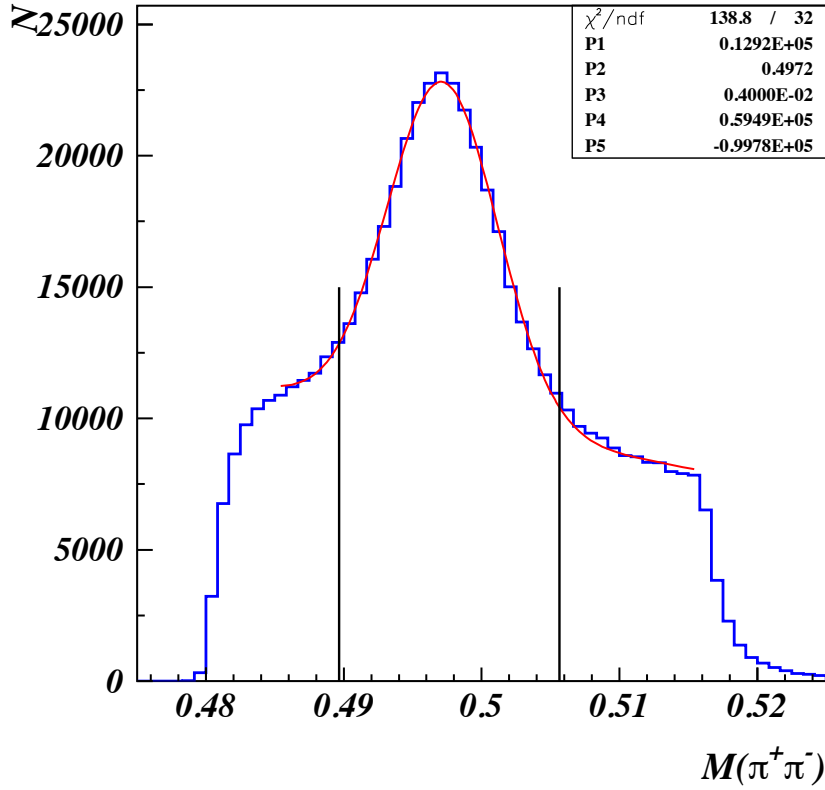


FIG. 28. The invariant mass of the $\pi^+\pi^-$ system with a very broad cut on K_L mass $M(K_L) = 0.49765 \pm 0.1(\text{GeV}/c^2)$ and a cut $M(K_SK_L) < 1.07\text{GeV}/c^2$. The distribution was fit with Gaussian+first order Polynomial function to obtain the peak parameters.

final particles can be identified from this histogram, including the K_L mesons. Figure 32 shows the missing mass of $\gamma p \rightarrow \pi^+\pi^- p(X)$ plotted in mass range 0.45-0.55 GeV/c^2 , requiring the invariant mass of K_SK_L to be less than $1.07\text{GeV}/c^2$ (in blue), and with an additional cut on invariant mass of $\pi^+\pi^-$ to be within $16\text{MeV}/c^2$ interval around K_S mass (in red).

Fig.33 shows the missing mass of $\gamma p \rightarrow p(X)$ system after 2σ cuts are applied to K_S and K_L masses.

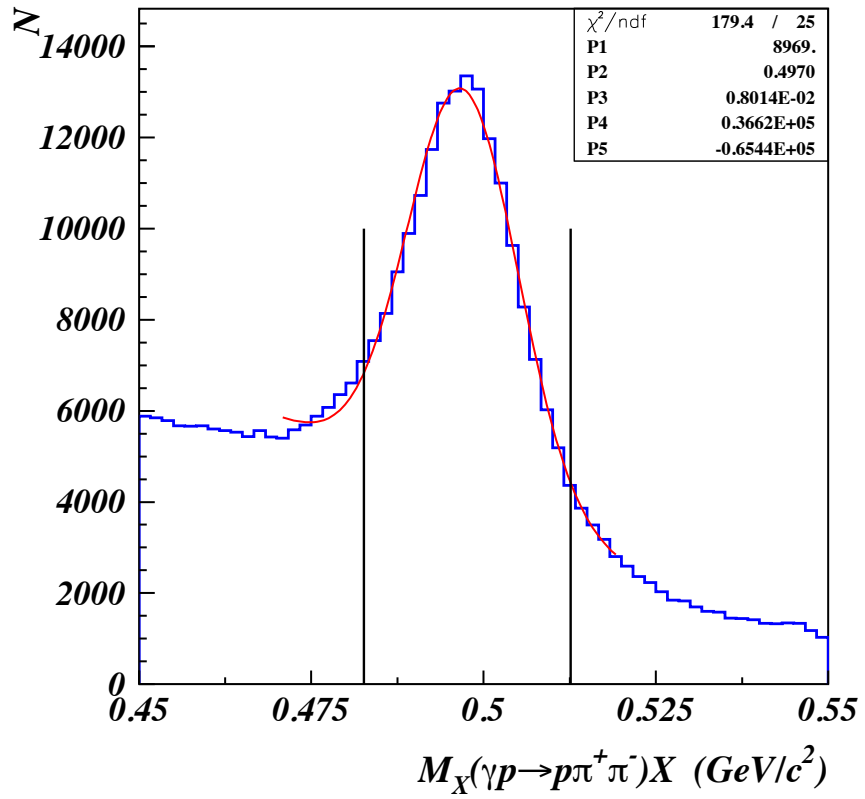


FIG. 29. The missing mass of $\gamma p \rightarrow p\pi^+\pi^-(X)$ with a cut $M(K_S) = 0.49765 \pm 0.035(\text{GeV}/c^2)$ and a cut $M(K_SK_L) < 1.07\text{GeV}/c^2$. The distribution was fit with Gaussian + first order Polynomial function to obtain the peak parameters.

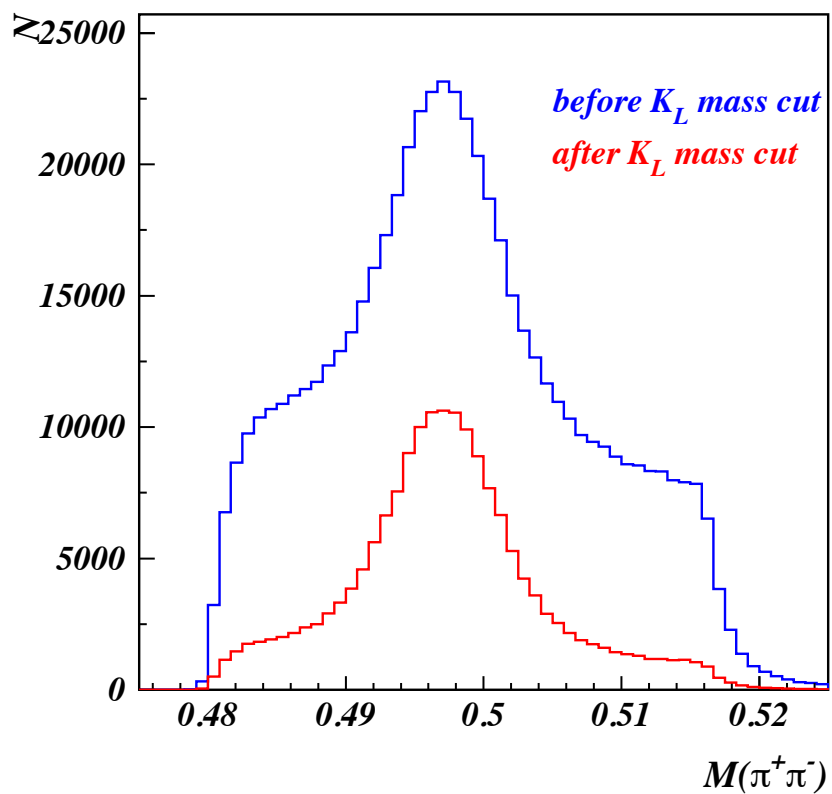


FIG. 30. Invariant mass of $\pi^+\pi^-$ system with a cut on mass of missing K_L from $\gamma p \rightarrow p\pi^+\pi^-(X)$ reaction: $\Delta M(K_L) = 30\text{MeV}/c^2$.

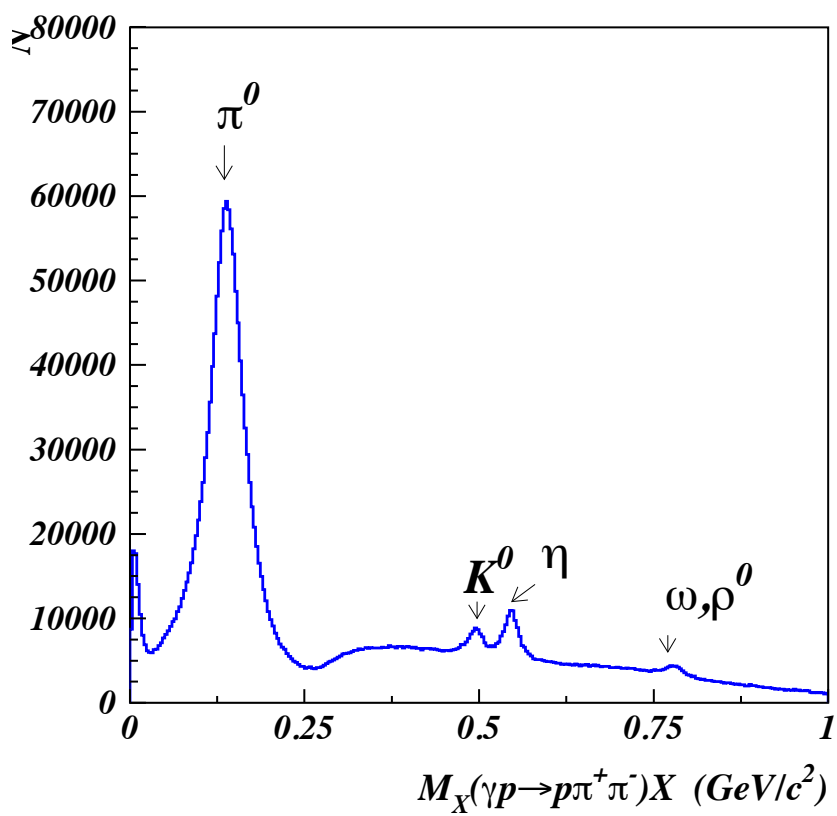


FIG. 31. Missing mass of $\gamma p \rightarrow p\pi^+\pi^-(X)$ reaction, with a cut on invariant mass of $\pi^+\pi^-$: $|M(\pi^+\pi^-) - 0.49765| < 0.015 GeV/c^2$.

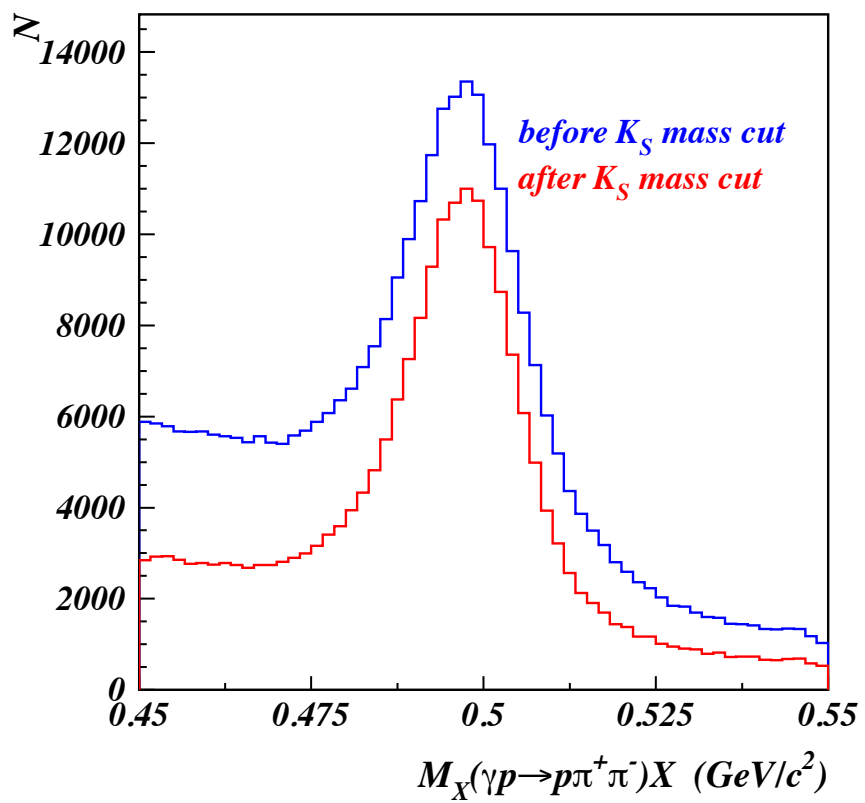


FIG. 32. Missing mass of $\gamma p \rightarrow p\pi^+\pi^-(X)$ reaction in $0.45-0.55$ GeV/c^2 range, with cuts: $\Delta M(K_S) = 16 MeV/c^2$ and $M(K_SK_L) < 1.07 GeV/c^2$.

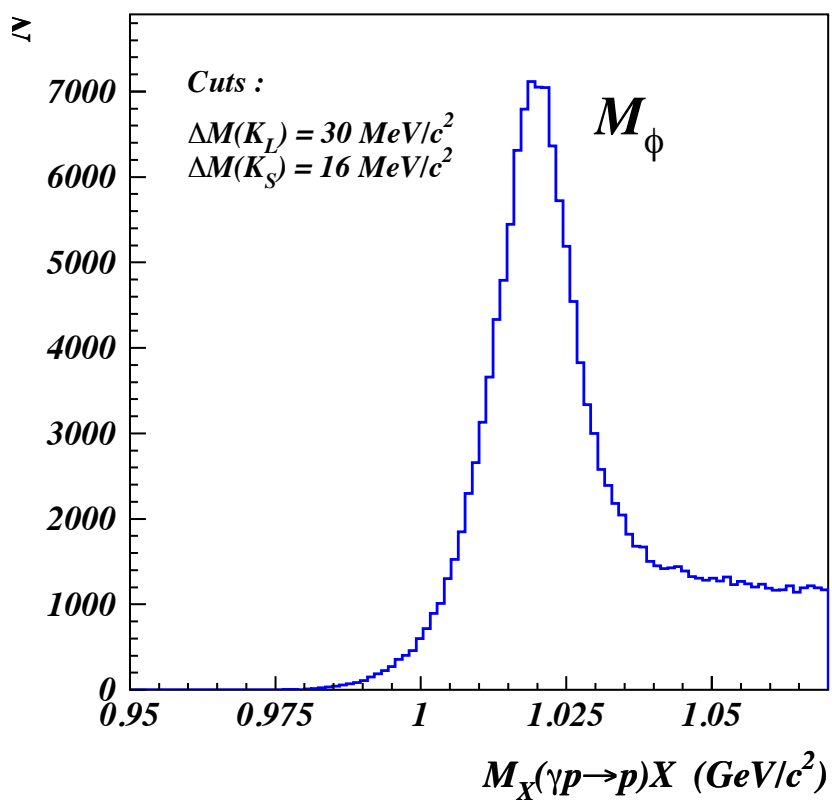


FIG. 33. Invariant mass of K_SK_L with cuts: $\Delta M(K_S) = 16\text{MeV}/c^2$ and $\Delta M(K_L) = 30\text{MeV}/c^2$.

Low momentum cuts	$P_{\pi^+, \pi^-} > 0.1(\text{GeV}/c)$, $P_p > 0.35(\text{GeV}/c)$
K_S selection	$M(\pi^+ \pi^-) = 0.49765 \pm 0.008(\text{GeV}^2/c^2)$
K_L selection	$MM(\gamma p \rightarrow p \pi^+ \pi^-) = 0.49765 \pm 0.015(\text{GeV}^2/c^2)$
ϕ meson selection	$MM(p) = 1.02 \pm 0.02(\text{GeV}^2/c^2)$
Efficiency cut	$\mathcal{E}_{p, \pi^+, \pi^-} > 40\%$

TABLE III. Table of kinematic cuts applied for data selection.

3.6 BACKGROUND SUBTRACTION

The Fig.33 shows that even after the application of cuts described above, there is still some amount of the background left. The background distribution is uneven around the $\phi(1020)$ peak and significant part of it is concentrated in the right side of the MM(p) mass spectrum. This, and also the unknown line-shape of ϕ makes the side-band subtraction method less reliable for signal-background separation. For that reason, the background subtraction method is modified to event based weighting with the probability coefficient of the particular event to be a signal or background event. The probability coefficients are obtained by the fit of MM(p) mass distributions in narrow photon energy and $\cos\theta_{c.m.}^\phi$ bins to a signal plus background fit function using MINUIT minimization package to obtain better agreement between the fit function and the actual data distribution. As a signal function we take relativistic Breit-Wigner function of the form

$$S(m, \zeta) = F(E, \zeta) \frac{\Gamma(E, \zeta)}{(m - \mu(E, \zeta))^2 + \Gamma(E, \zeta)/2^2} \quad (59)$$

where Γ is the width, μ is the mean of the mass distributions, $\zeta = \cos[\theta]_{c.m.}^\phi$, E is the photon energy.

Three different background functions were used for the fit: $f(x) = a\sqrt{x^2 - 4m_K^2} + b(x^2 - 4m_K^2)$, $x > 2m_K$, $g(x) = a(x - 2m_K) + b(x - 2m_K)^2$ and third order polynomial.

The differences of the results depending on the choice of the background fit function are used to evaluate the systematic errors due to background subtraction.

The weight factor for each event is obtained as a ratio

$$W_i = \frac{S_i(m_i, E, \zeta)}{S_i(m_i, E, \zeta) + B_i(m_i, E, \zeta)} \quad (60)$$

where $S_i(m_i, E, \zeta)$ and $B_i(m_i, E, \zeta)$ are the values of the signal and background functions, respectively, for the given i-th event mass m_i , photon energy E and $\cos \theta_{c.m.}^\phi$ value.

Figures 34-51 show the results of fits of MM(p) distributions in different photon energy and $\cos \theta_{c.m.}^\phi$ bins. The black histograms are unweighted distributions from data. The red histograms are the signal distributions weighted by the weight factor W. The blue histograms are the background distributions weighted by (1-W). The fit quality is limited for the very backward angle regions, where there is a very small to almost no statistics depending on energy and angular bins.

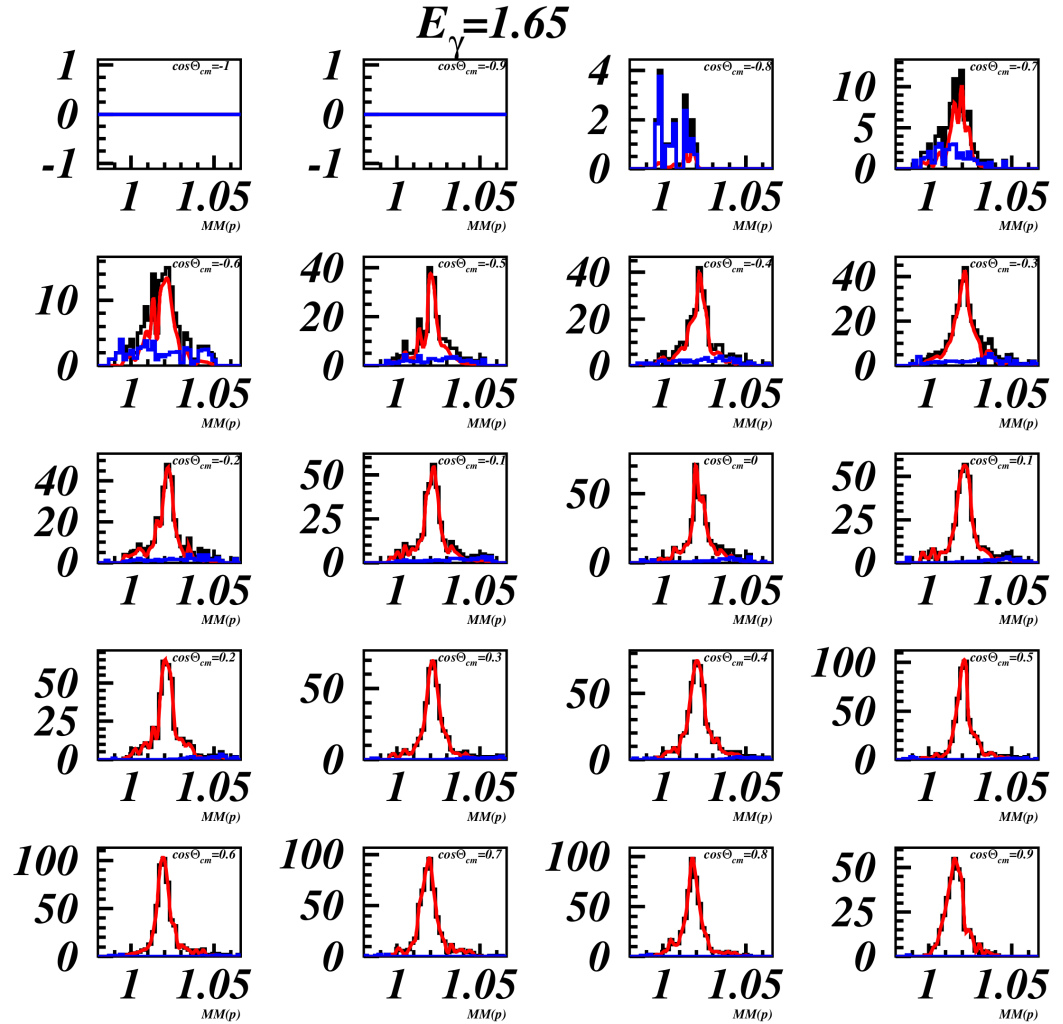


FIG. 34. Signal and background separation for $1.6 \geq E_\gamma < 1.7$ GeV and different $\cos \theta_{c.m.}^\phi$ bins. The black histograms are the unweighted distributions from data. The red histograms are the signal distributions weighted by W . The blue histograms are the background distributions weighted by $(1-W)$.

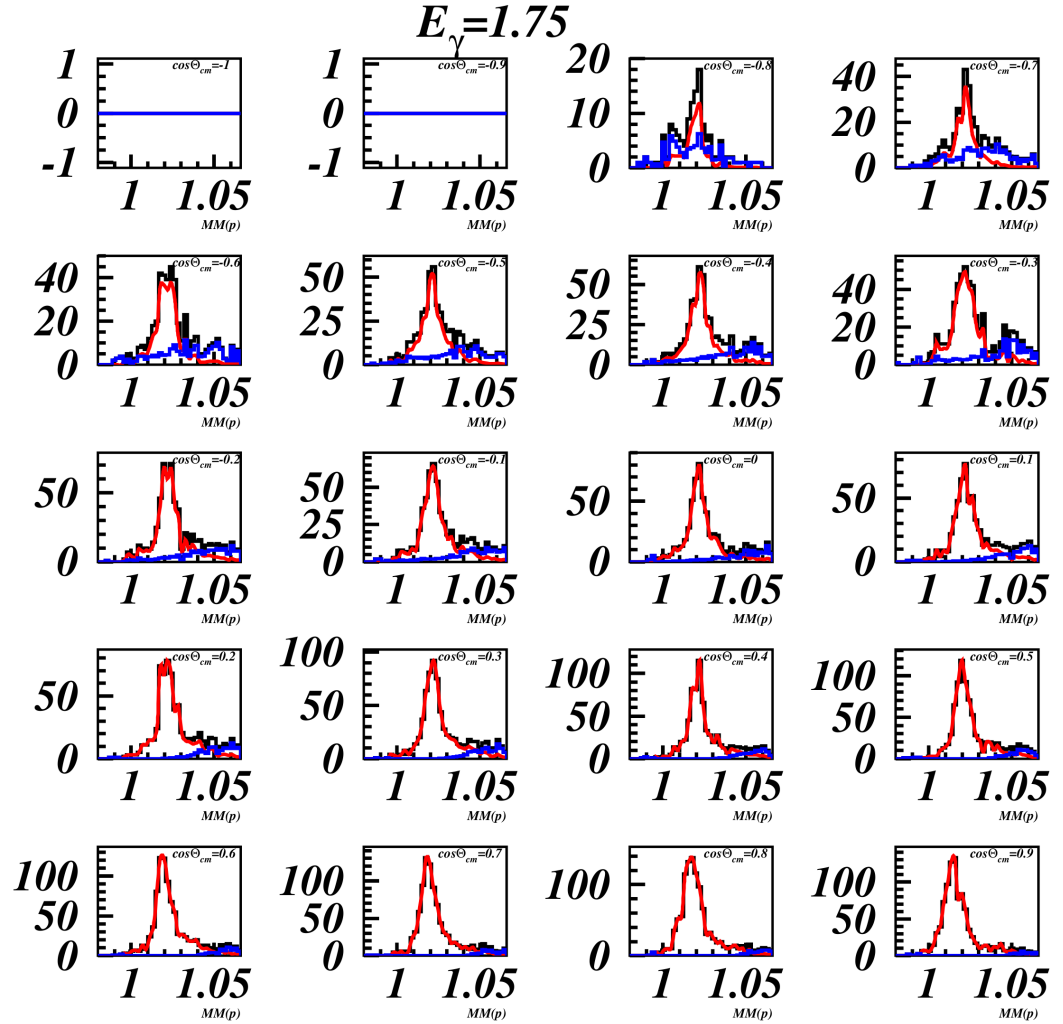


FIG. 35. Signal and background separation for $1.7 \geq E_\gamma < 1.8$ GeV and different $\cos \theta_{c.m.}^\phi$ bins. The black histograms are the unweighted distributions from data. The red histograms are the signal distributions weighted by W . The blue histograms are the background distributions weighted by $(1-W)$.

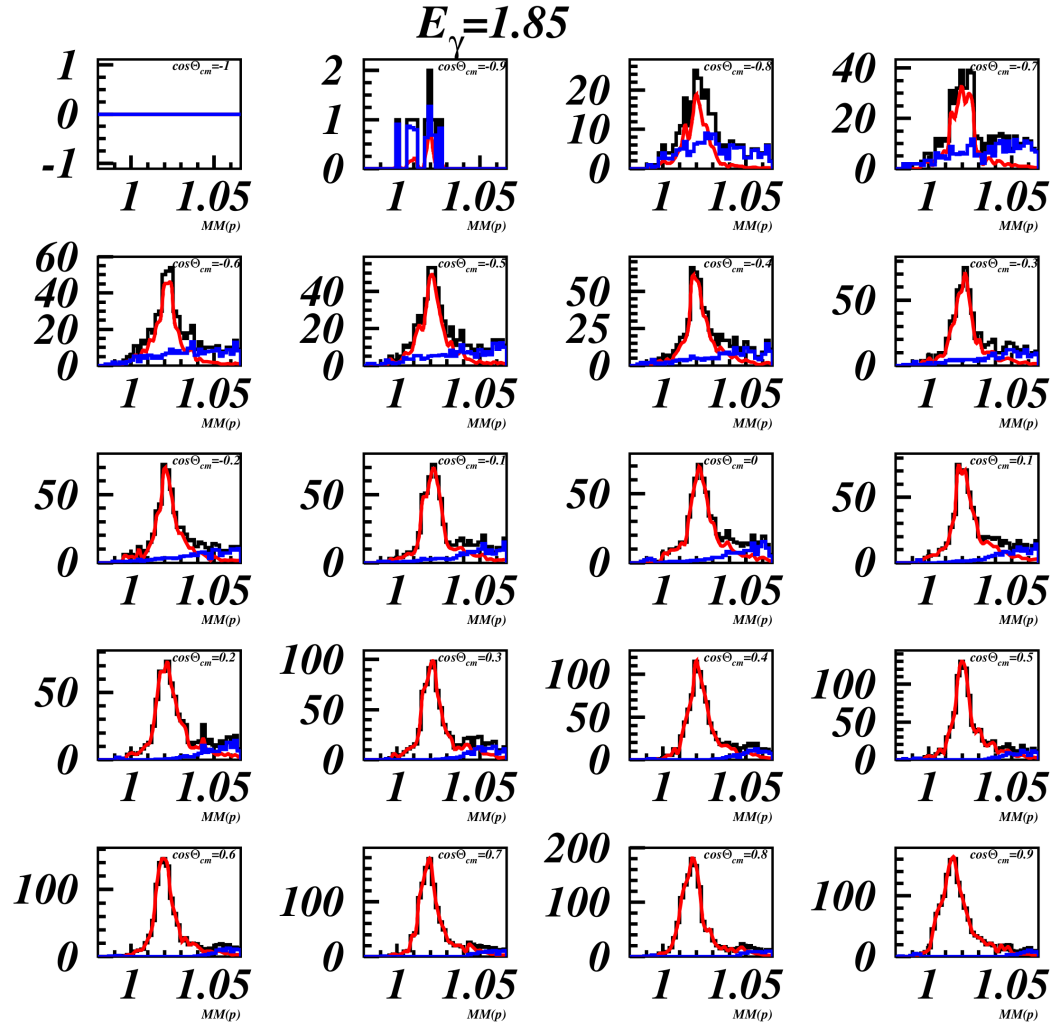


FIG. 36. Signal and background separation for $1.8 \geq E_\gamma < 1.9$ GeV and different $\cos \theta_{c.m.}^\phi$ bins. The black histograms are the unweighted distributions from data. The red histograms are the signal distributions weighted by W . The blue histograms are the background distributions weighted by $(1-W)$.

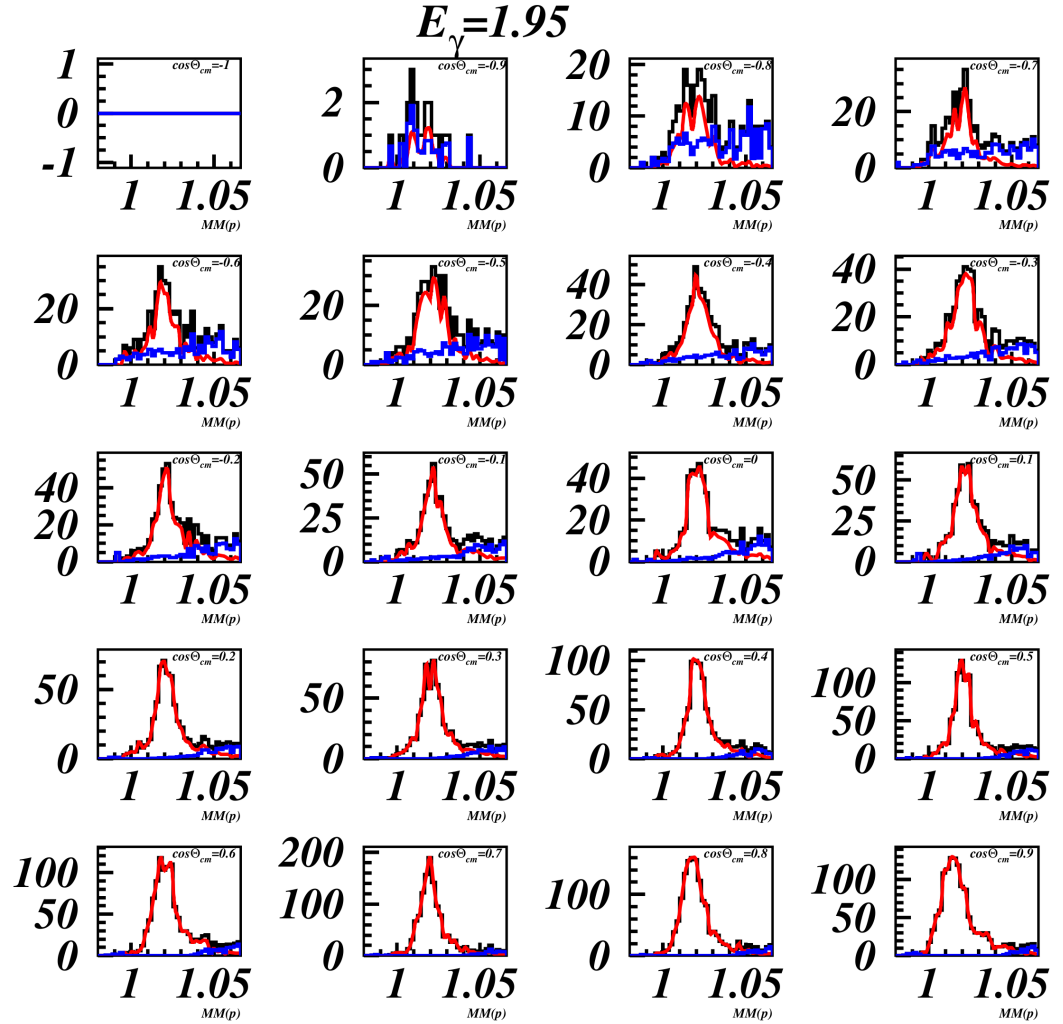


FIG. 37. Signal and background separation for $1.9 \geq E_\gamma < 2.0$ GeV and different $\cos \theta_{c.m.}^\phi$ bins. The black histograms are the unweighted distributions from data. The red histograms are the signal distributions weighted by W . The blue histograms are the background distributions weighted by $(1-W)$.

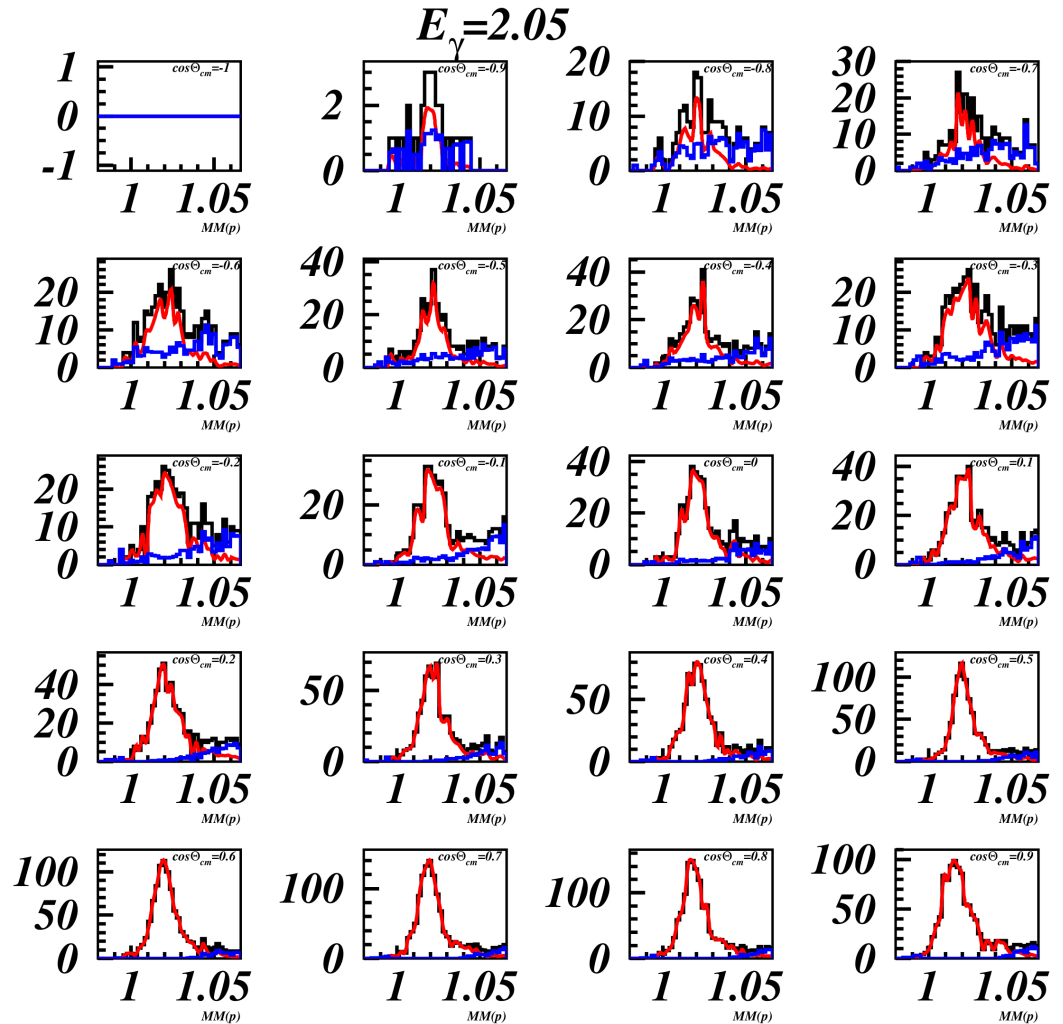


FIG. 38. Signal and background separation for $2.0 \geq E_\gamma < 2.1$ GeV and different $\cos \theta_{c.m.}^\phi$ bins. The black histograms are the unweighted distributions from data. The red histograms are the signal distributions weighted by W . The blue histograms are the background distributions weighted by $(1-W)$.

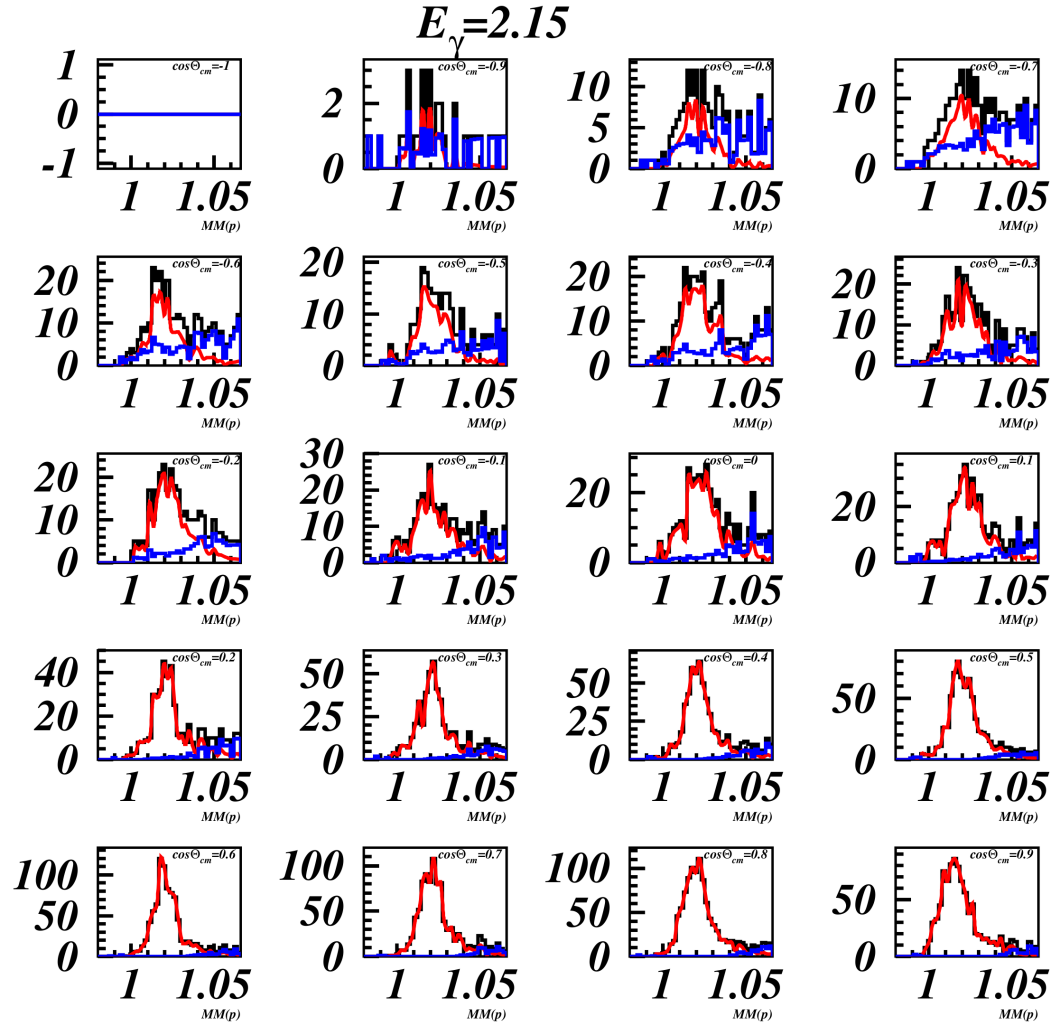


FIG. 39. Signal and background separation for $2.1 \geq E_\gamma < 2.2$ GeV and different $\cos \theta_{c.m.}^\phi$ bins. The black histograms are the unweighted distributions from data. The red histograms are the signal distributions weighted by W . The blue histograms are the background distributions weighted by $(1-W)$.

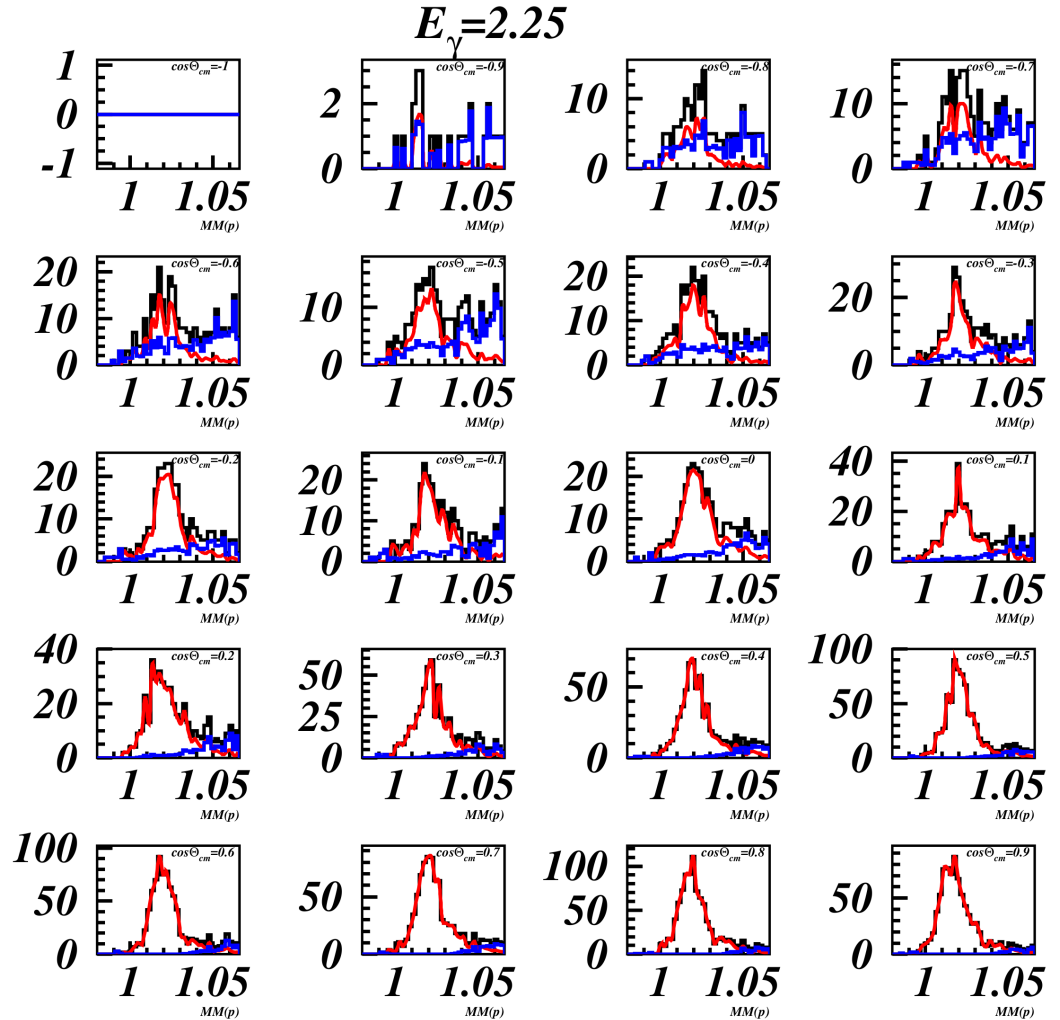


FIG. 40. Signal and background separation for $2.2 \geq E_\gamma < 2.3$ GeV and different $\cos \theta_{c.m.}^\phi$ bins. The black histograms are the unweighted distributions from data. The red histograms are the signal distributions weighted by W . The blue histograms are the background distributions weighted by $(1-W)$.

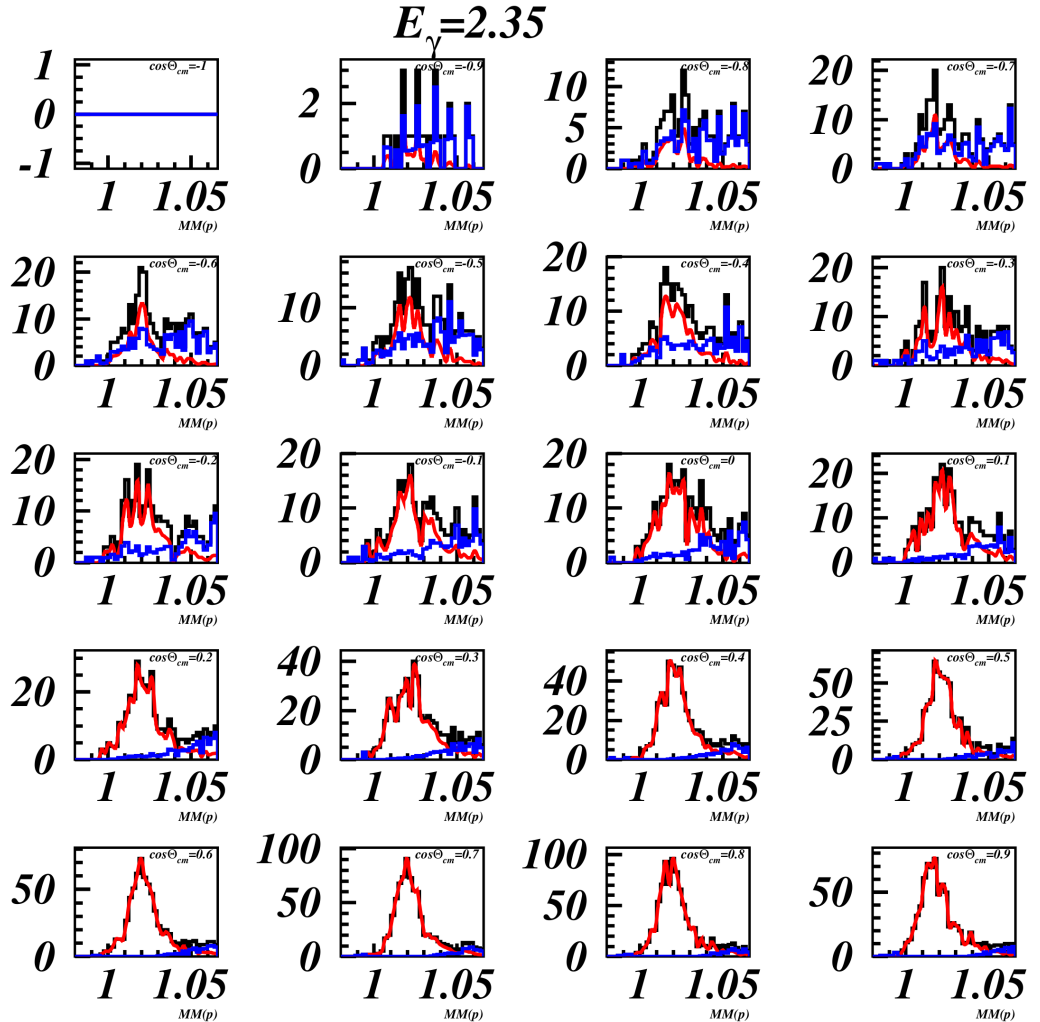


FIG. 41. Signal and background separation for $2.3 \geq E_\gamma < 2.4$ GeV and different $\cos \theta_{c.m.}^\phi$ bins. The black histograms are the unweighted distributions from data. The red histograms are the signal distributions weighted by W . The blue histograms are the background distributions weighted by $(1-W)$.

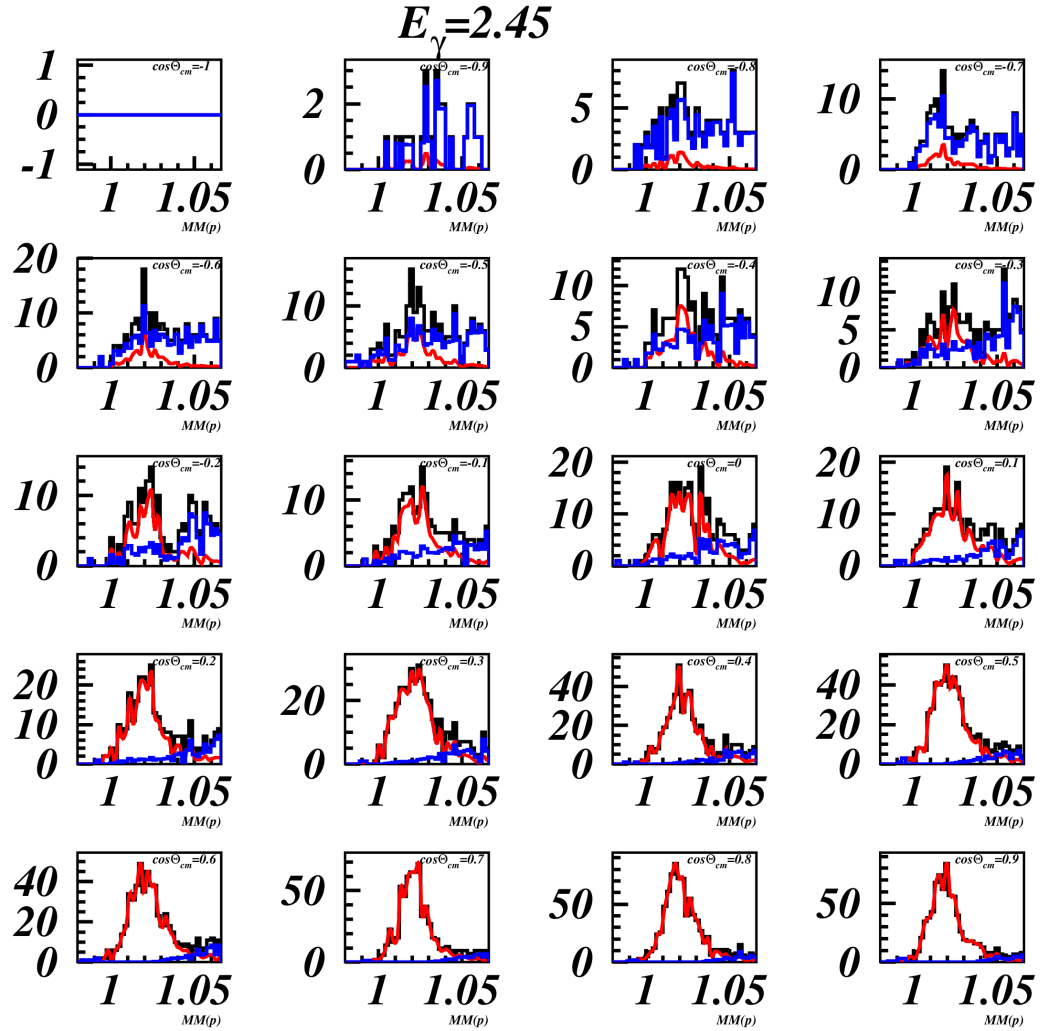


FIG. 42. Signal and background separation for $2.4 \geq E_\gamma < 2.5$ GeV and different $\cos\theta_{c.m.}^\phi$ bins. The black histograms are the unweighted distributions from data. The red histograms are the signal distributions weighted by W . The blue histograms are the background distributions weighted by $(1-W)$.

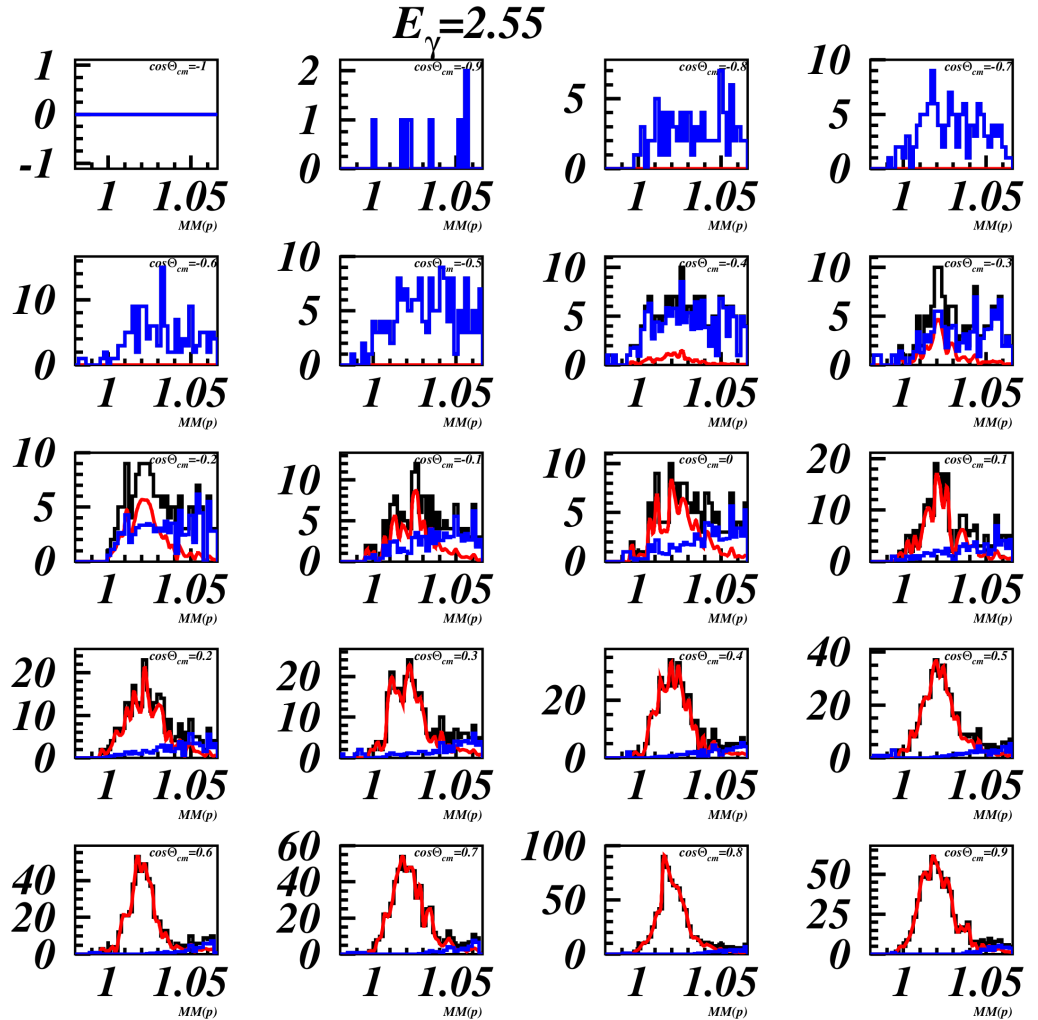


FIG. 43. Signal and background separation for $2.5 \geq E_\gamma < 2.6$ GeV and different $\cos \theta_{c.m.}^\phi$ bins. The black histograms are the unweighted distributions from data. The red histograms are the signal distributions weighted by W . The blue histograms are the background distributions weighted by $(1-W)$.

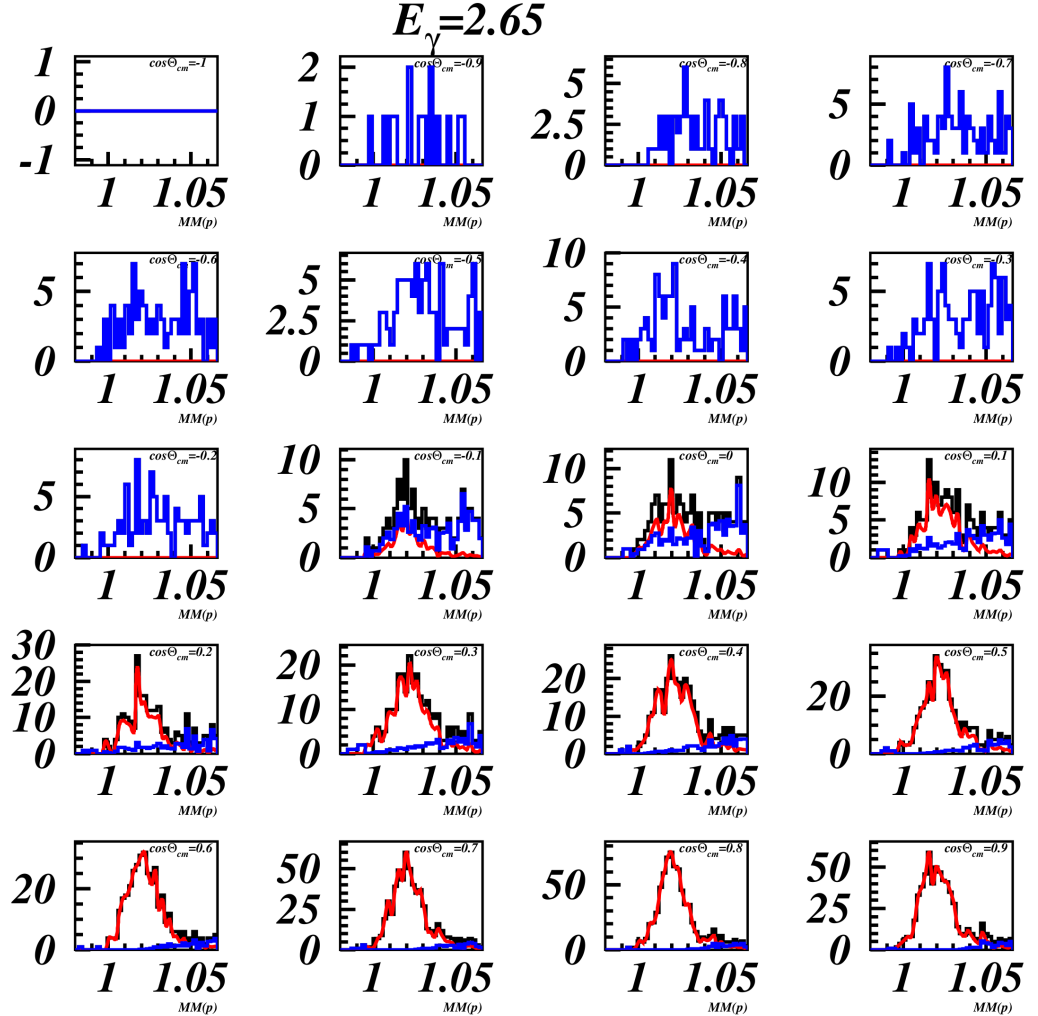


FIG. 44. Signal and background separation for $2.6 \geq E_\gamma < 2.7$ GeV and different $\cos \theta_{c.m.}^\phi$ bins. The black histograms are the unweighted distributions from data. The red histograms are the signal distributions weighted by W . The blue histograms are the background distributions weighted by $(1-W)$.

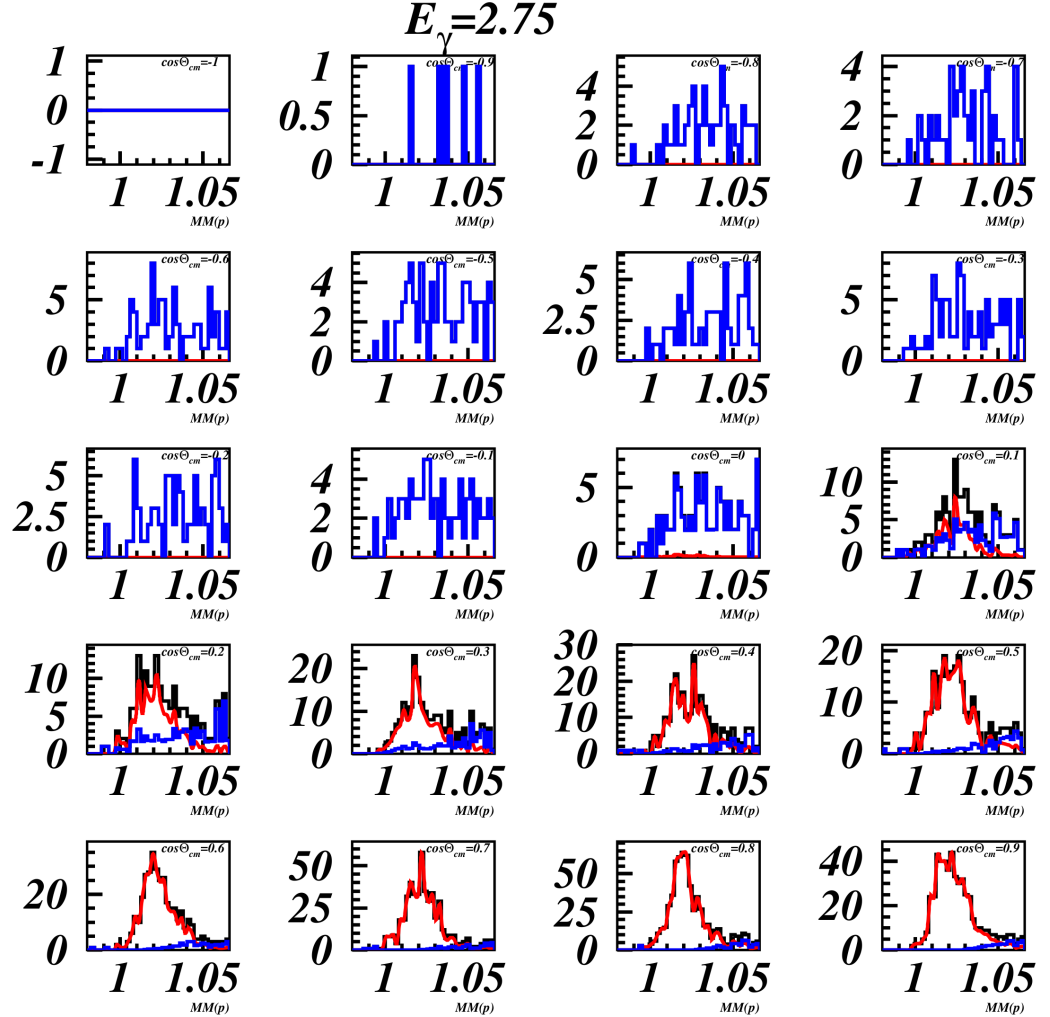


FIG. 45. Signal and background separation for $2.7 \geq E_\gamma < 2.8$ GeV and different $\cos \theta_{c.m.}^\phi$ bins. The black histograms are the unweighted distributions from data. The red histograms are the signal distributions weighted by W . The blue histograms are the background distributions weighted by $(1-W)$.

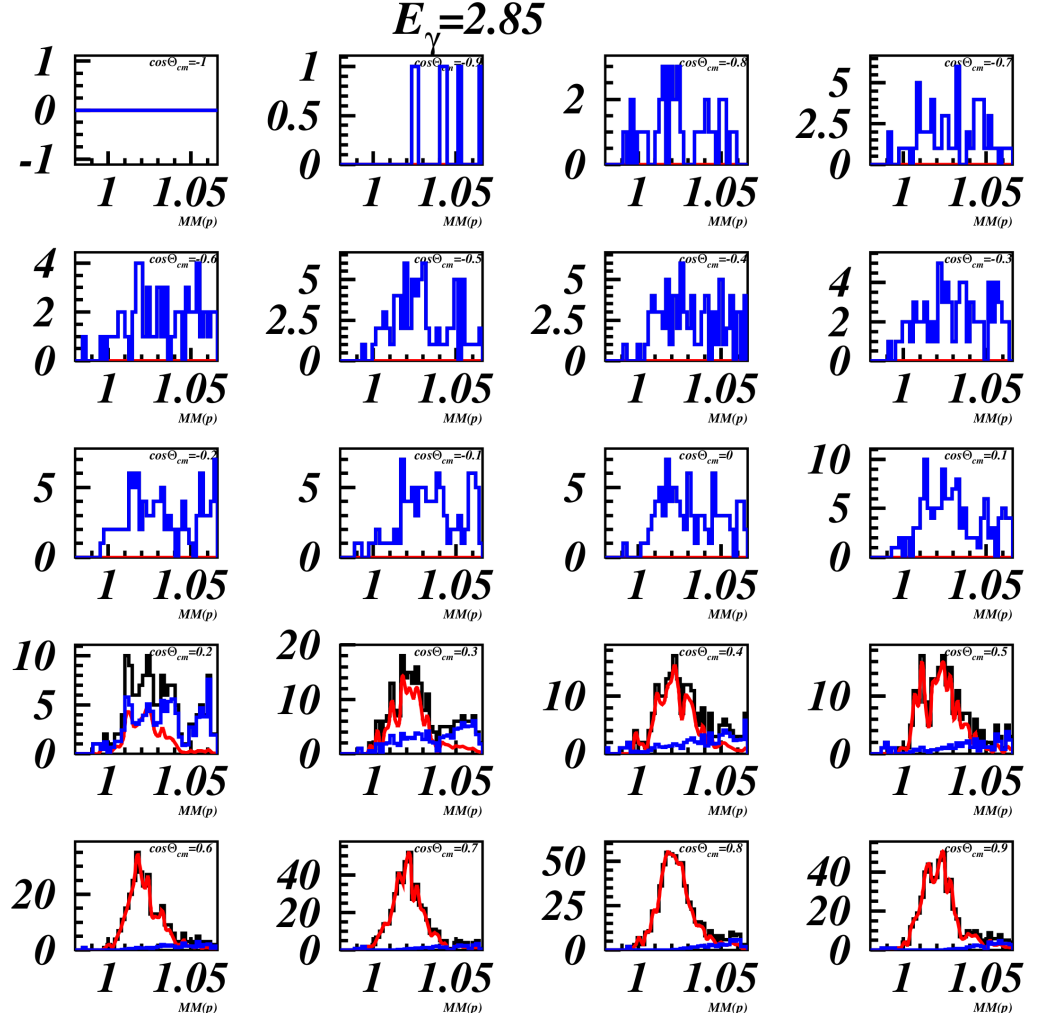


FIG. 46. Signal and background separation for $2.8 \geq E_\gamma < 2.9$ GeV and different $\cos \theta_{c.m.}^\phi$ bins. The black histograms are the unweighted distributions from data. The red histograms are the signal distributions weighted by W . The blue histograms are the background distributions weighted by $(1-W)$.

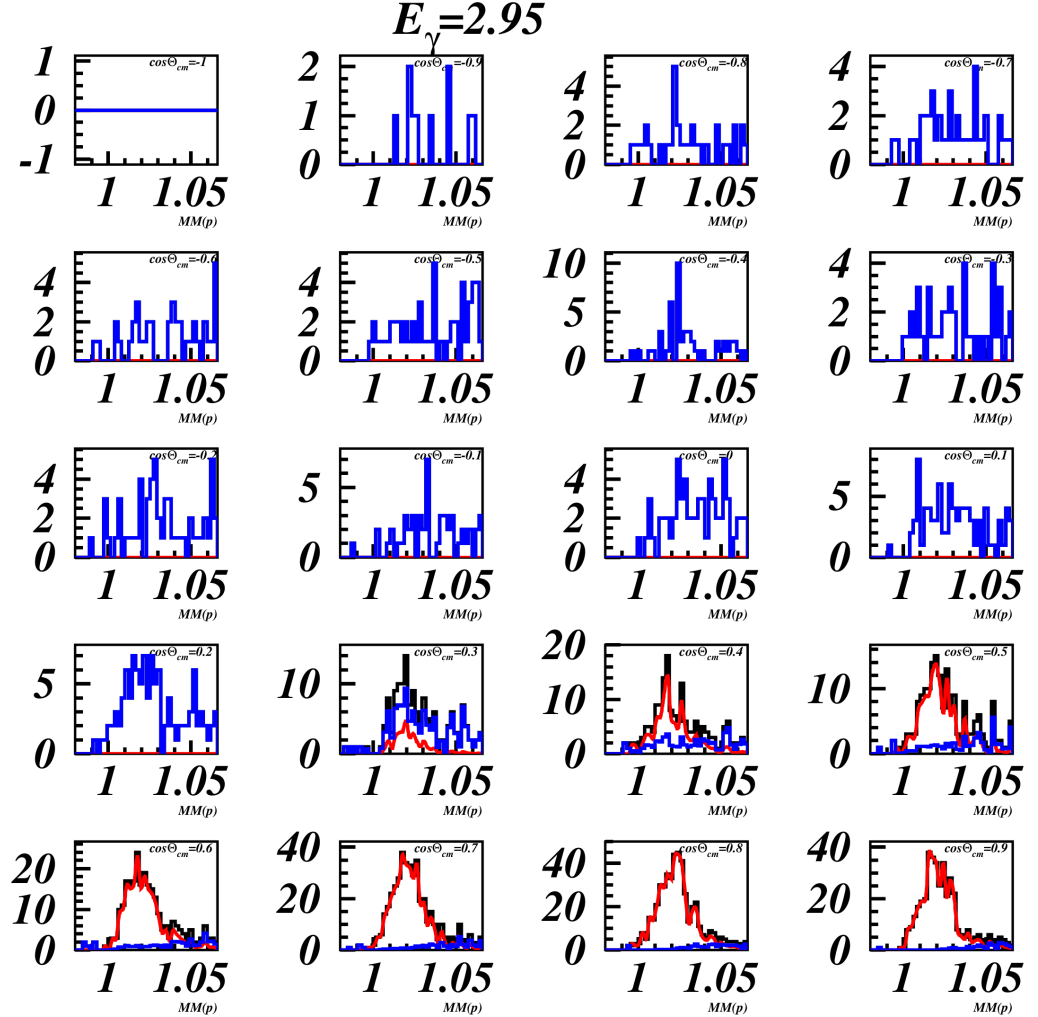


FIG. 47. Signal and background separation for $2.9 \geq E_\gamma < 3.0$ GeV and different $\cos \theta_{c.m.}^\phi$ bins. The black histograms are the unweighted distributions from data. The red histograms are the signal distributions weighted by W . The blue histograms are the background distributions weighted by $(1-W)$.

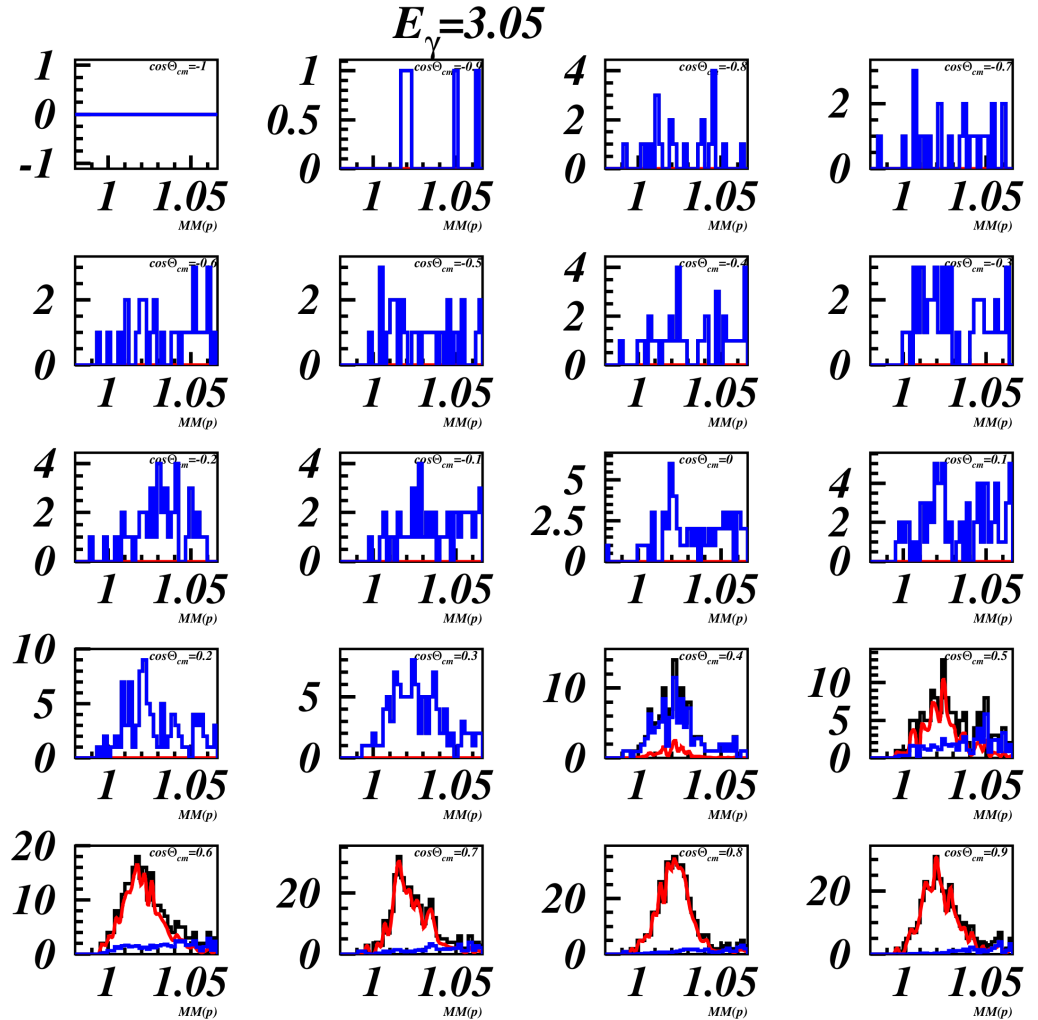


FIG. 48. Signal and background separation for $3.0 \geq E_\gamma < 3.1$ GeV and different $\cos\theta_{c.m.}^\phi$ bins. The black histograms are the unweighted distributions from data. The red histograms are the signal distributions weighted by W . The blue histograms are the background distributions weighted by $(1-W)$.

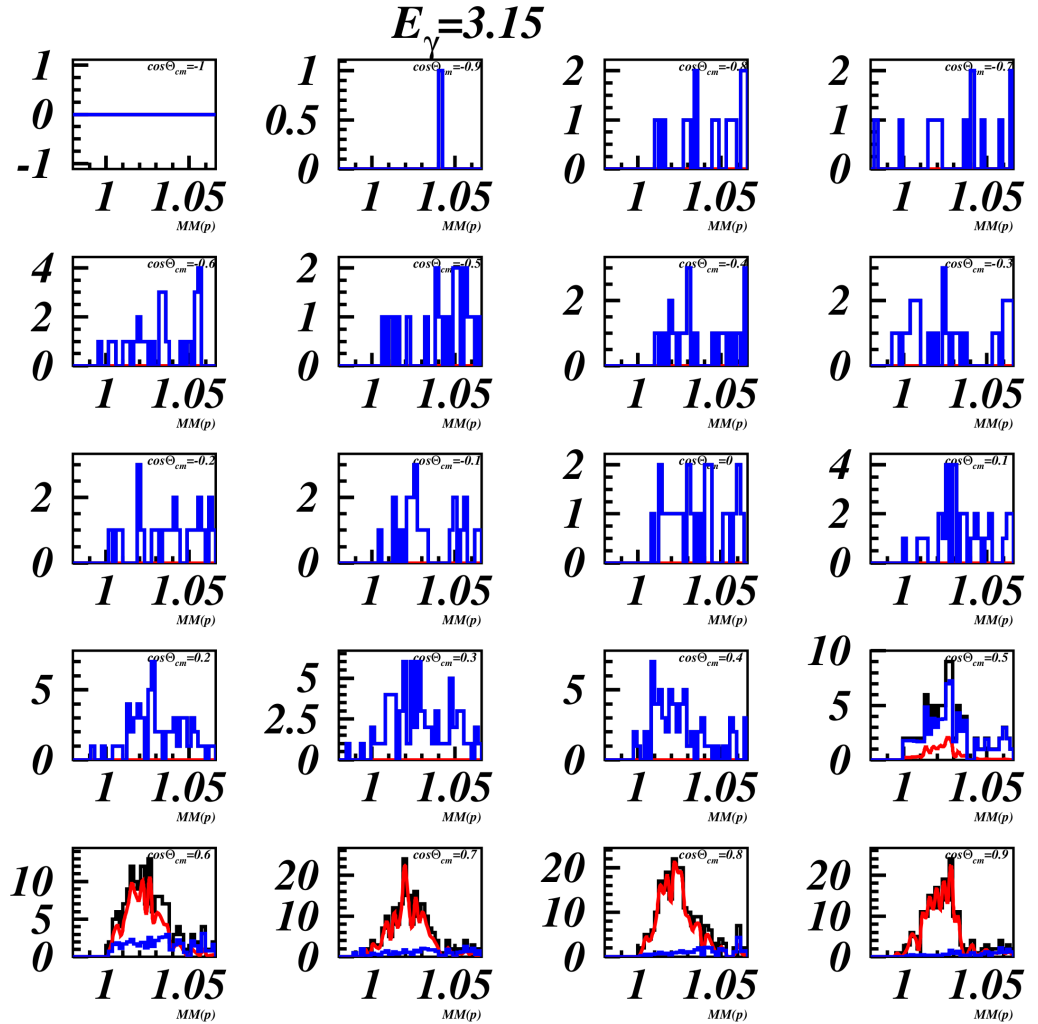


FIG. 49. Signal and background separation for $3.1 \geq E_\gamma < 3.2$ GeV and different $\cos \theta_{c.m.}^\phi$ bins. The black histograms are the unweighted distributions from data. The red histograms are the signal distributions weighted by W . The blue histograms are the background distributions weighted by $(1-W)$.

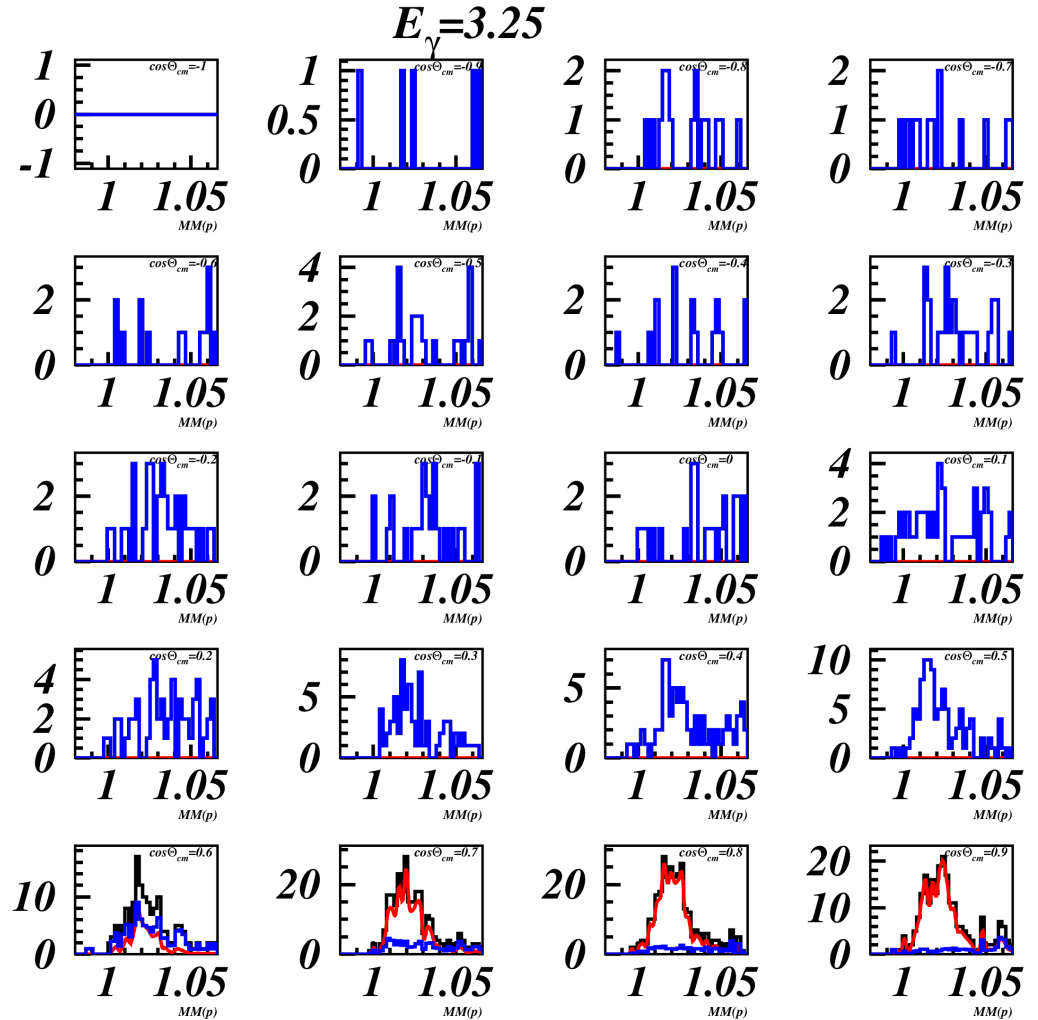


FIG. 50. Signal and background separation for $3.2 \geq E_\gamma < 3.3$ GeV and different $\cos \theta_{c.m.}^\phi$ bins. The black histograms are the unweighted distributions from data. The red histograms are the signal distributions weighted by W . The blue histograms are the background distributions weighted by $(1-W)$.

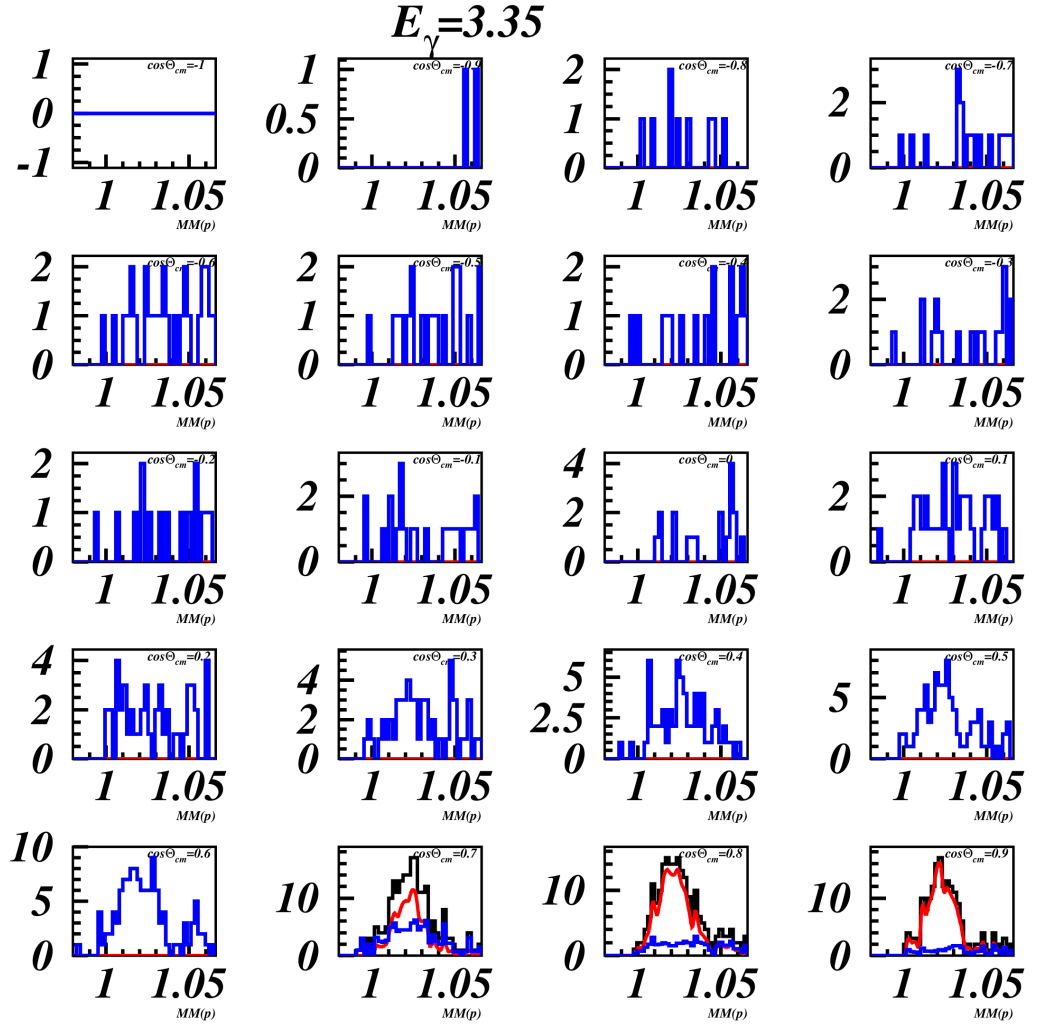


FIG. 51. Signal and background separation for $3.3 \geq E_\gamma < 3.4$ GeV and different $\cos \theta_{c.m.}^\phi$ bins. The black histograms are the unweighted distributions from data. The red histograms are the signal distributions weighted by W . The blue histograms are the background distributions weighted by $(1-W)$.

3.7 ACCEPTANCE CORRECTION AND NORMALIZATION

3.7.1 Monte Carlo generator

Some of the particles fly into regions not covered by CLAS at all, and it is not possible to detect them. And in general the acceptance of the CLAS is not flat. To be able to convert experimental data into measured cross sections acceptance corrections must be applied. To obtain the acceptance for the reaction of interest ϕ meson Monte Carlo generator was used along with CLAS GSIM and RECSIS packages.

In this analysis we use ϕ meson Monte-Carlo generator developed by G. Gavalian. The MC events are generated using the Titov and Lee theoretical model for photo-production of ϕ mesons [14], with no adjustable parameters, which well describes the existing data in a wide range of photon energies and t_ϕ covered by this experiment. The Monte-Carlo simulation of ϕ -meson production was used, with a subsequent decay chain: $\phi \rightarrow K_S + K_L$ and K_S decay $K_S \rightarrow \pi^+ \pi^-$. The simulated final state of p, π^+, π^- was then run through the GEANT Simulation program (GSIM) for the CLAS detector and was reconstructed with CLAS standard reconstruction code (RECSIS). In this analysis only the normalization constant may be used as a free parameter of the MC spectrum. It is adjusted to describe the data in the range of photon energies $E_\gamma = (2.2 - 2.6)$ GeV. After that, the same normalization constant is used to generate events for the photon energy interval of $E_\gamma = (1.6 - 2.6)$ GeV. All other MC generator parameters were taken from the published model without alteration.

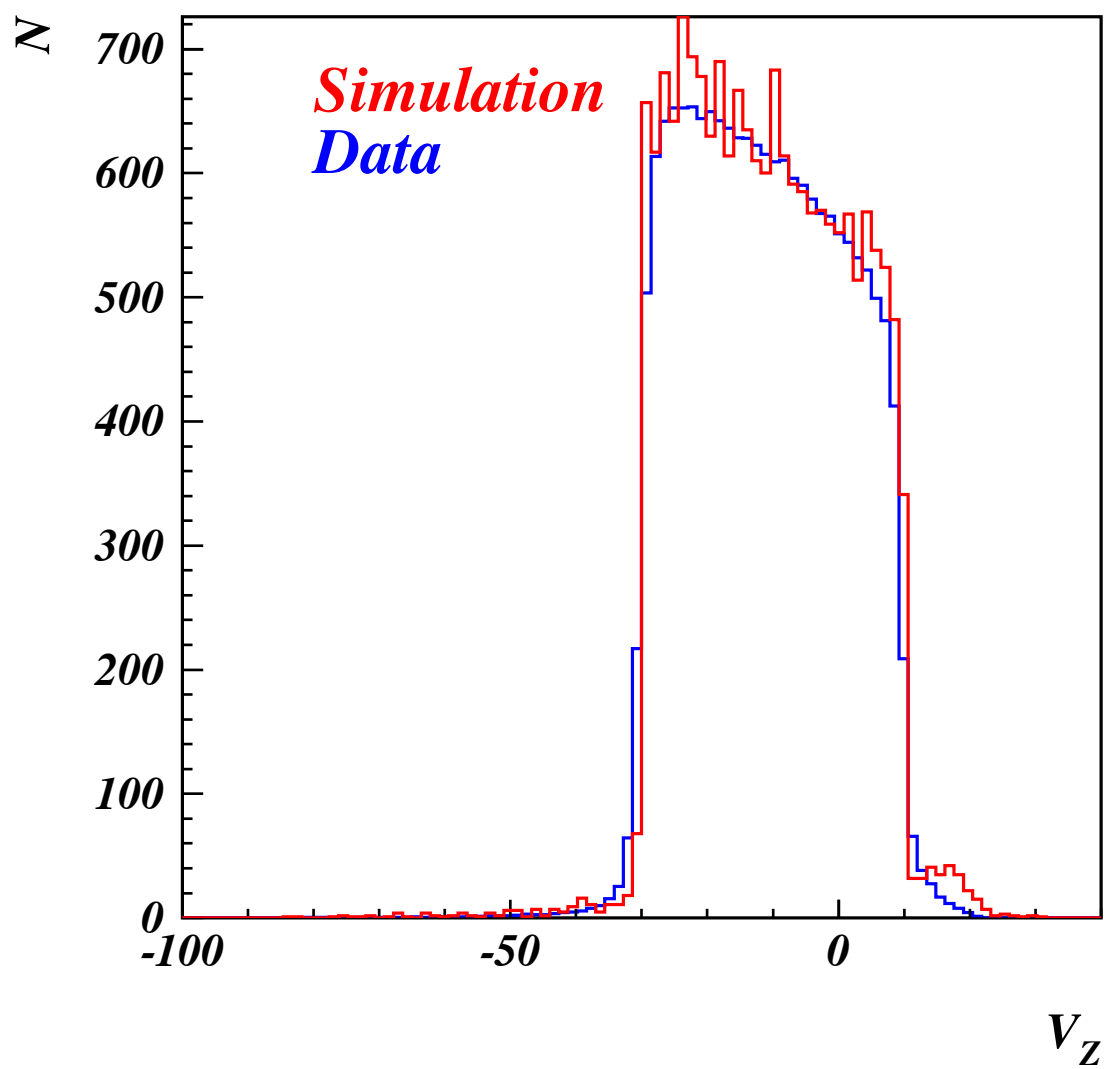


FIG. 57. The z component of proton vertex for data (blue) and simulation (red).

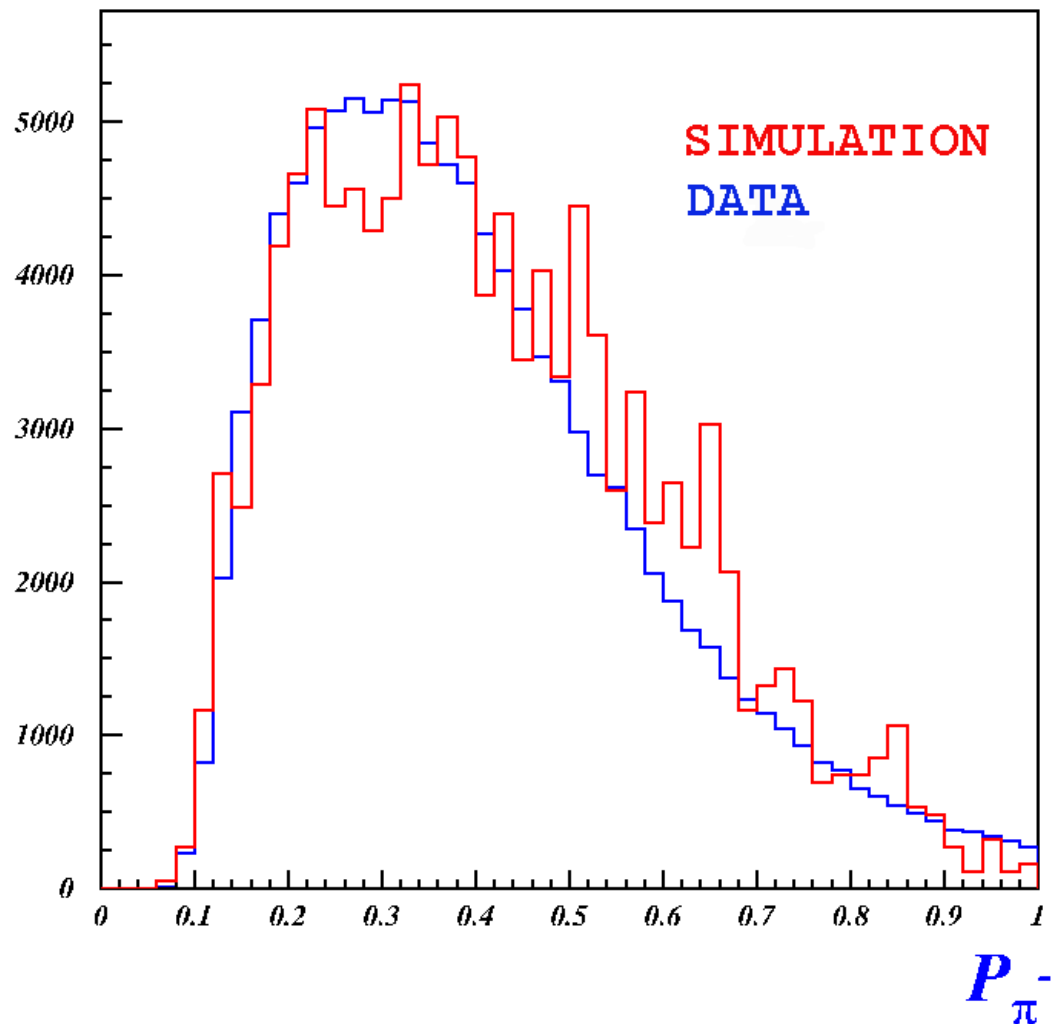


FIG. 58. Momentum of π^- meson for data (blue) and simulation (red).

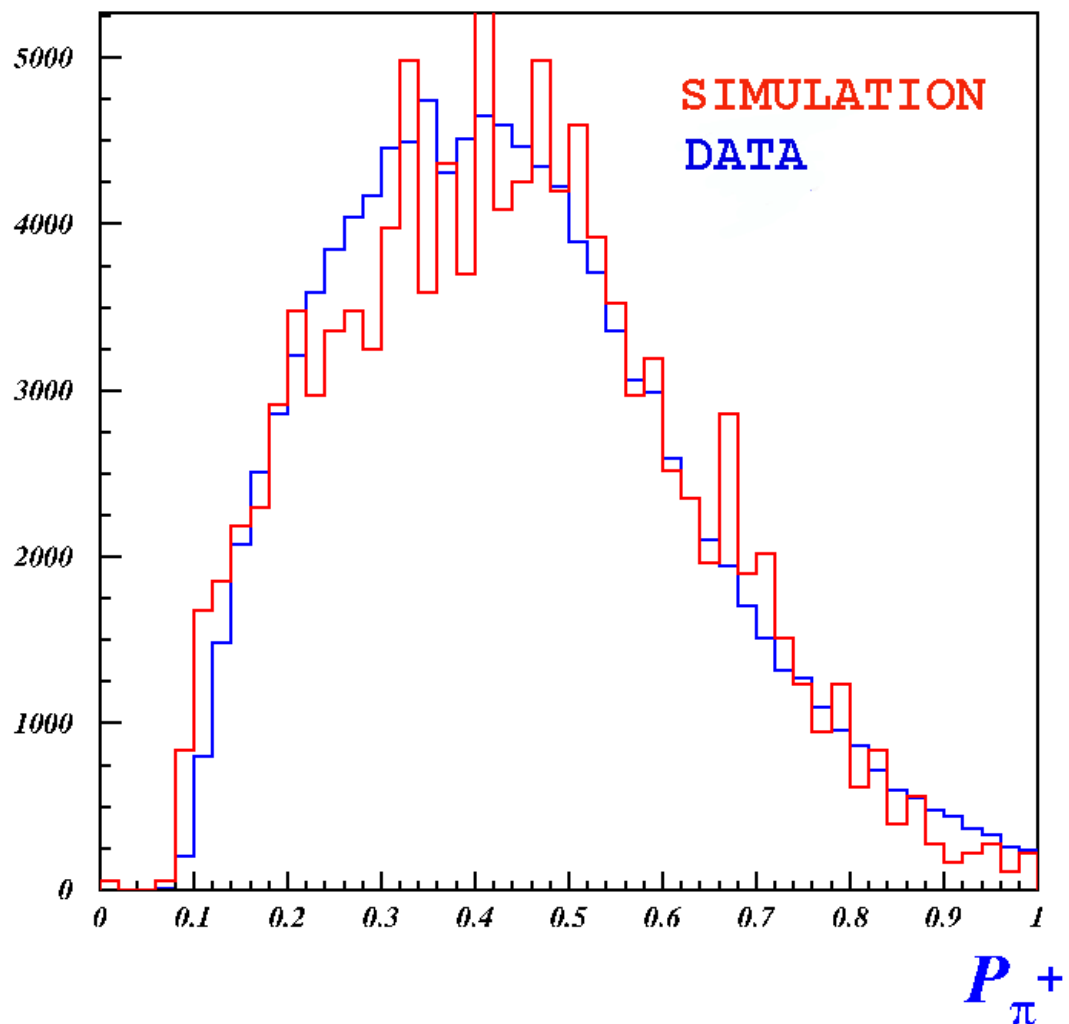


FIG. 59. Momentum of π^+ meson for data (blue) and simulation (red).

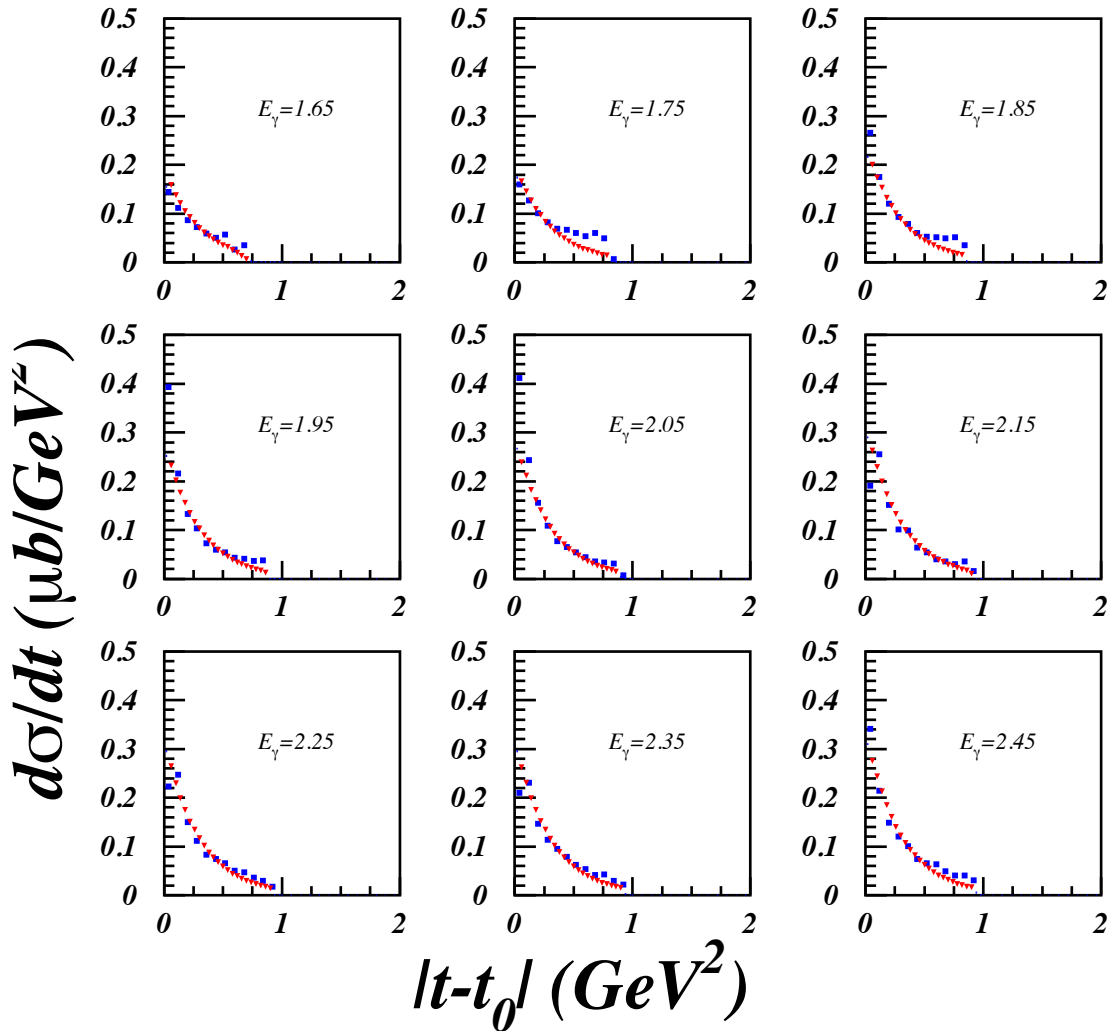


FIG. 60. $|t - t_0|$ dependences of differential cross section $d\sigma/dt$ for ϕ mesons from data (blue) compared to normalized MC distributions (red).

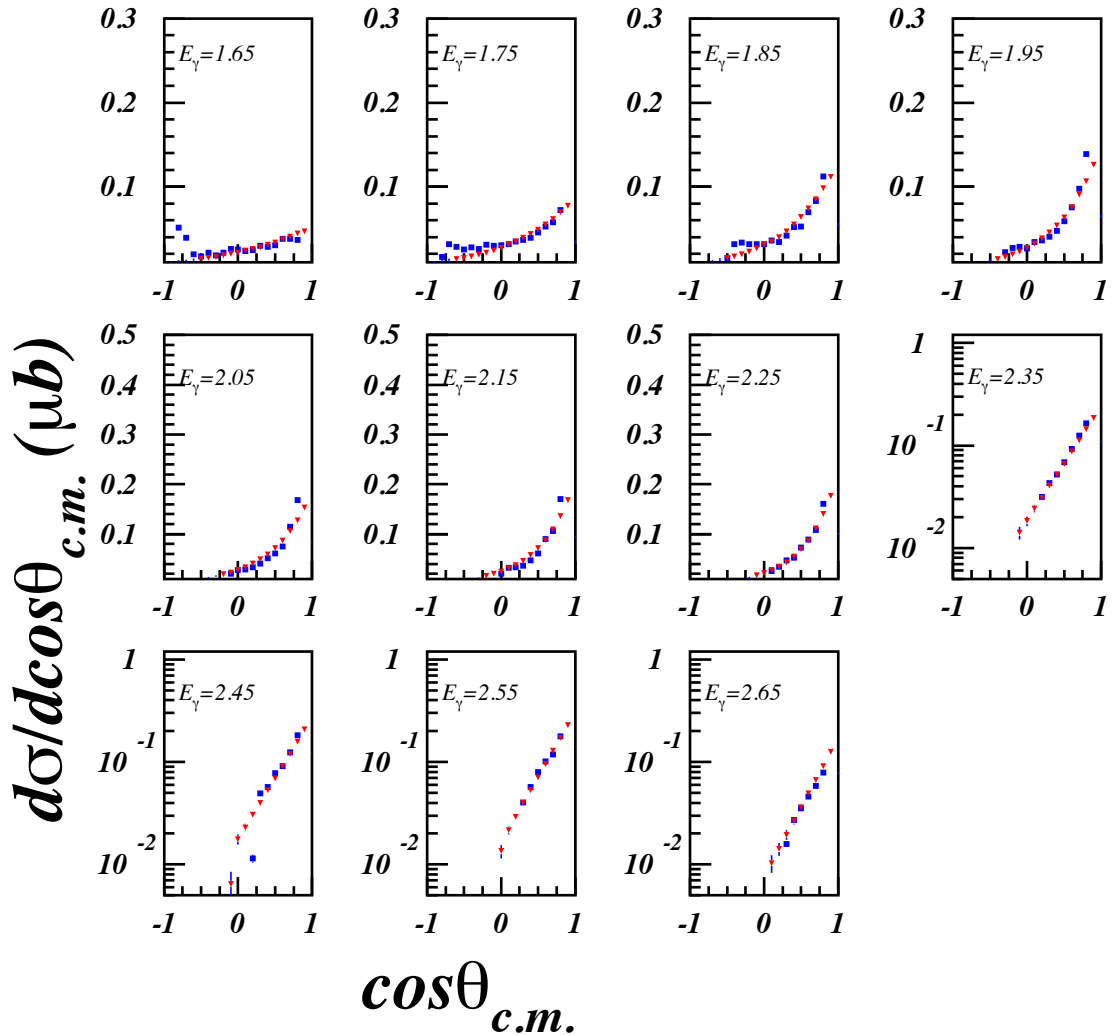


FIG. 61. $\cos\theta_{c.m.}$ dependences of differential cross section $d\sigma/d\cos\theta_{c.m.}$ for ϕ mesons from data (blue) compared to normalized MC distributions (red).

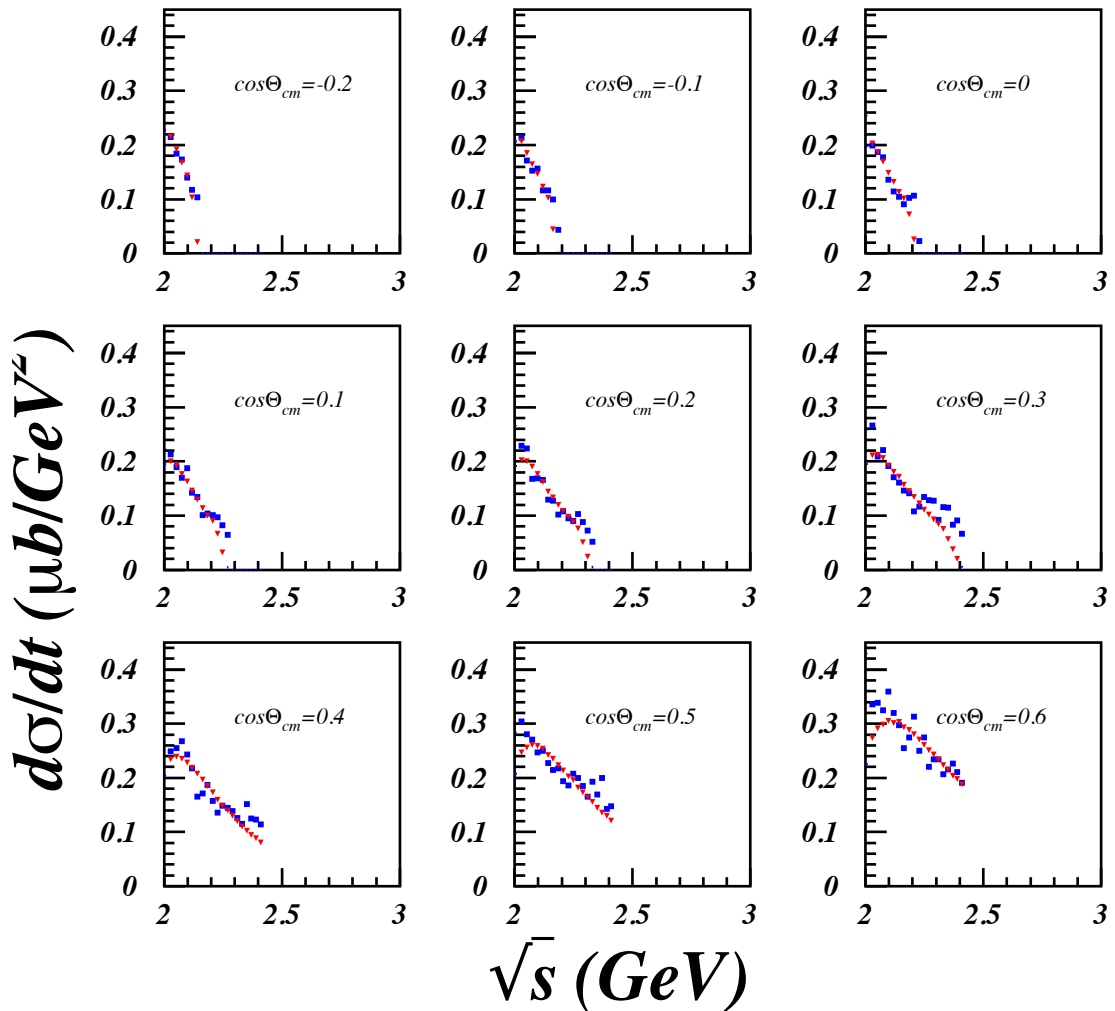


FIG. 62. \sqrt{s} dependences of differential cross section $d\sigma/dt$ for ϕ mesons from data (blue) compared to normalized MC distributions (red).

3.7.2 Acceptance

To obtain the acceptances for the current analysis, first events are uniformly generated in a phase space with the Monte Carlo generator. Then generated events are processed through GSIM package, which is based on GEANT and simulates the CLAS detector. The software imitates the particle propagation through the CLAS detector and simulates detection signals. In particular, GSIM simulates processes affecting the particles in detector, like the energy losses of the particles in the detector, any possible particle decays and multiple scattering effects.

Finally, RECSIS reconstruction program is used to cook GSIM output, in the manner raw experimental data are cooked.

We apply the same cuts to MC that are applied to data to select the events. Also CLAS Eloss package corrections are applied to reconstructed momenta of p, π^+ and π^- .

The acceptance is calculated as

$$\text{Acceptance} = \frac{\text{Reconstructed events(with corrections and cuts)}}{\text{Generated events}} \quad (61)$$

The acceptances for each $t - t_{min}$ bin and different photon energy ranges are plotted in Fig.52.

The acceptances are also obtained to normalize the ϕ meson decay angular distributions. The acceptances for different $\cos\theta$ bins and different photon energy regions are obtained for the Helicity frame (Fig.53) and for the Gottfried-Jackson frame (Fig.54). The acceptances for the azimuthal angle Φ distributions are plotted on Fig.55 for the Helicity frame and on Fig.56 for the Gottfried-Jackson frame.

To eliminate the bin migration problems, the number of energy bins and $t - t_{min}$ bins are chosen to be twice the number of bins used for data. For $\cos\Theta$ distributions the number of energy bins is also taken two times grater than the number of bins for data, and the number of angle bins is the same as for data. For azimuthal angle Φ distributions the number of energy bins and angle bins are the same for MC and

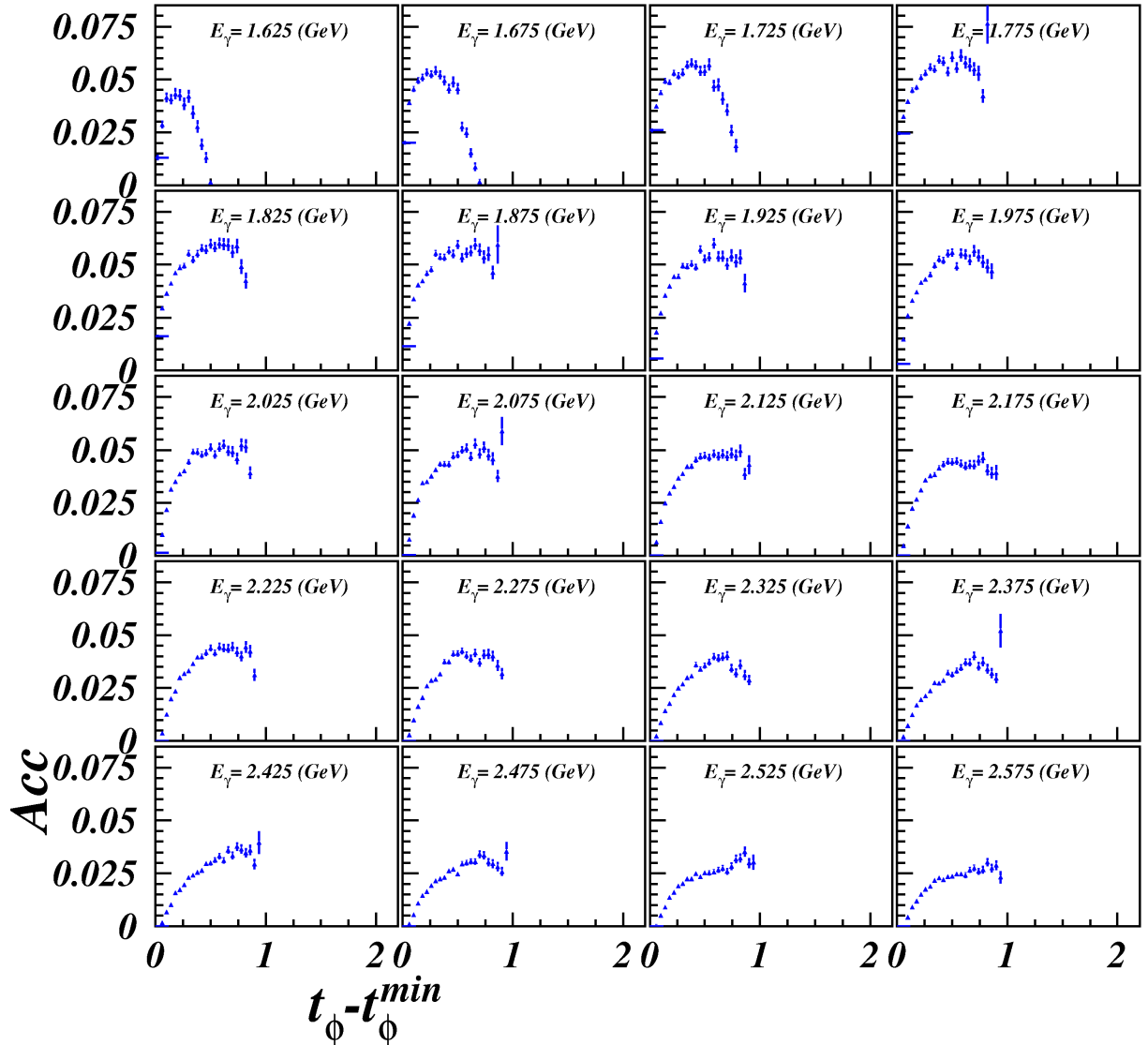


FIG. 52. Calculated acceptances for different $t - t_{min}$ bins and different photon energy ranges.

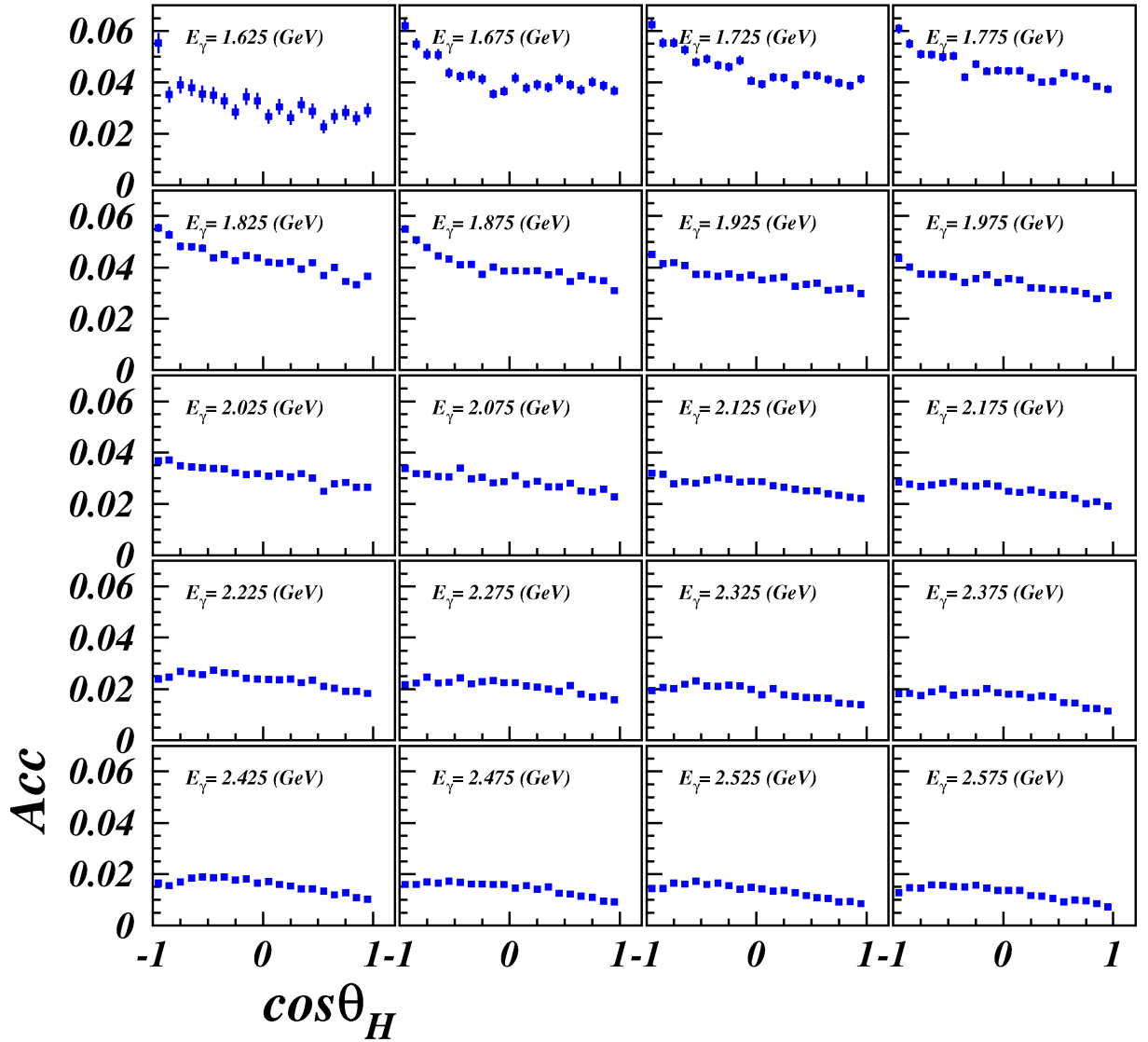


FIG. 53. Calculated acceptances for different $\cos\theta$ bins in Helicity frame and different photon energy ranges.

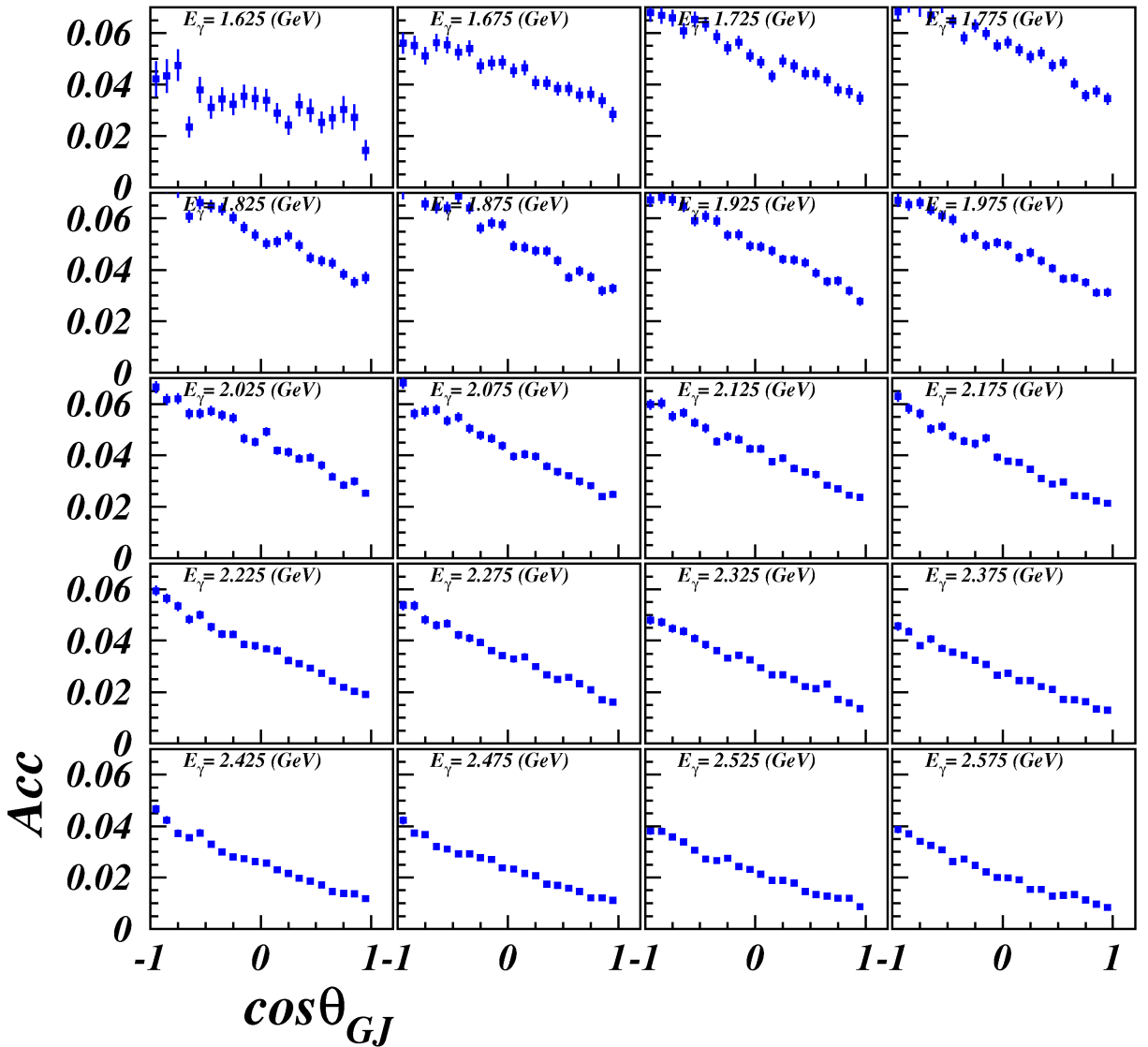


FIG. 54. Calculated acceptances for different $\cos\Theta$ bins in Gottfried-Jackson frame and different photon energy ranges.

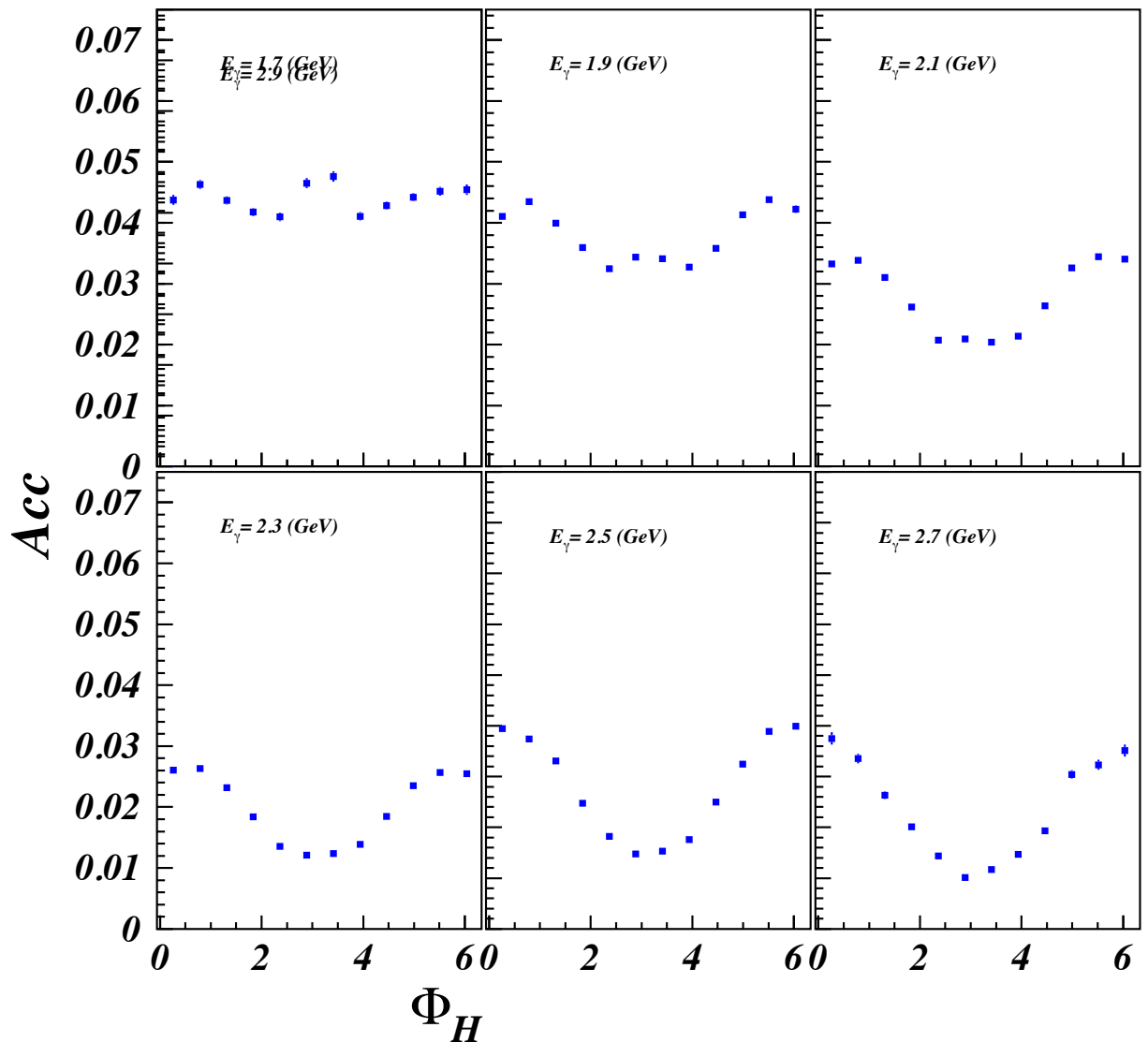


FIG. 55. Calculated acceptances for different azimuthal angle Φ bins in Helicity frame and different photon energy ranges.

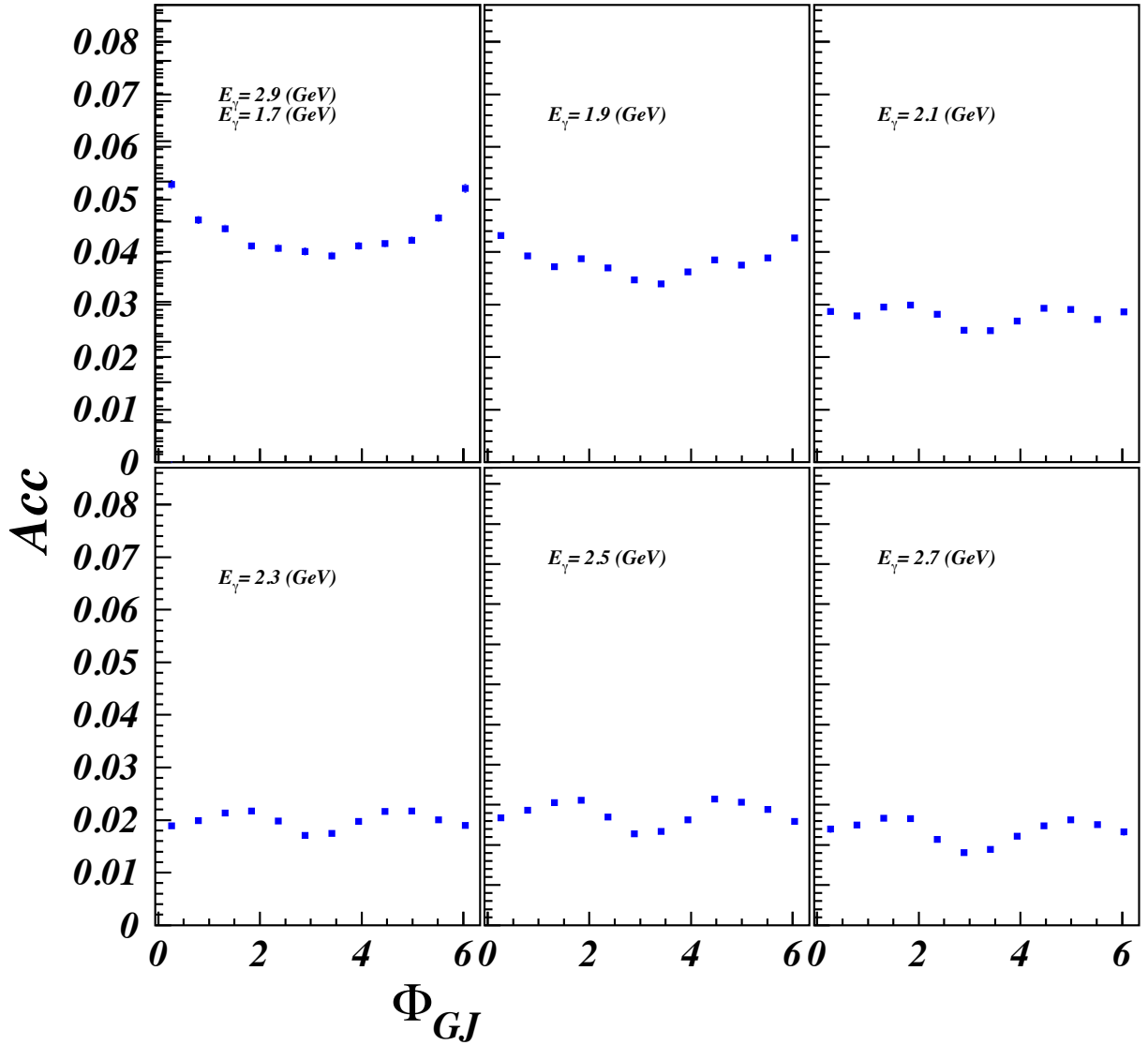


FIG. 56. Calculated acceptances for different azimuthal angle Φ bins in Gottfried–Jackson frame and different photon energy ranges.

data.

3.7.3 The Target Density

To measure the cross sections we must know the density of the target used in the experiment. The g11 experiment used a liquid hydrogen as a target, the density of which can be obtained from the following expression

$$\rho = a_1 T^2 + a_2 P + a_3 \quad (62)$$

where T is the temperature, P is the pressure and the values of a_1, a_2, a_3 parameters are given in Table 3.7.3

Parameter	Value
a_1	$-2.89 \times 10^{-5} g/cm^3 K^2$
a_2	$1.0 \times 10^{-7} g/cm^3 mbar$
a_3	$8.249 \times 10^{-2} g/cm^3$

TABLE IV. The parameter values, used to calculate liquid hydrogen target density [55].

The average target density for all g11 runs used in this analyses is approximately $0.0718 \frac{g}{cm^3}$, with variance $\sigma^2 \approx 0.678 \times 10^{-8} \frac{g^2}{cm^6}$. The relative fluctuations of the density are about 0.1%.

3.7.4 Normalization to the Flux

The photon flux for the experiment is obtained using 'gflux' package of CLAS ([56]). The photon flux for each tagger T-counter and for each g11 run are obtained using the rates at which the electrons hit the given T-counter in a fixed time interval. The number of electrons hitting the T-counter is obtained taking into account the detector live time. Then the T-counter flux is used to obtain the flux for different photon energy bins ([57],[58]). In the g11 experiment some dependence of normalized yield on the beam current was observed. The CLAS Collaboration Genova group

derived a correction factor by fitting the dependence with a line. The correction at 65 nA was 1.187. A possible explanation of the reason for such a problem is suggested by CMU group to arise due to the inaccurate estimate of DAQ dead time. Events associated with a beam trip are excluded from the analysis ([59]). In Fig. 63 the photon flux is plotted as a function of photon beam energy for 50 MeV energy bins.

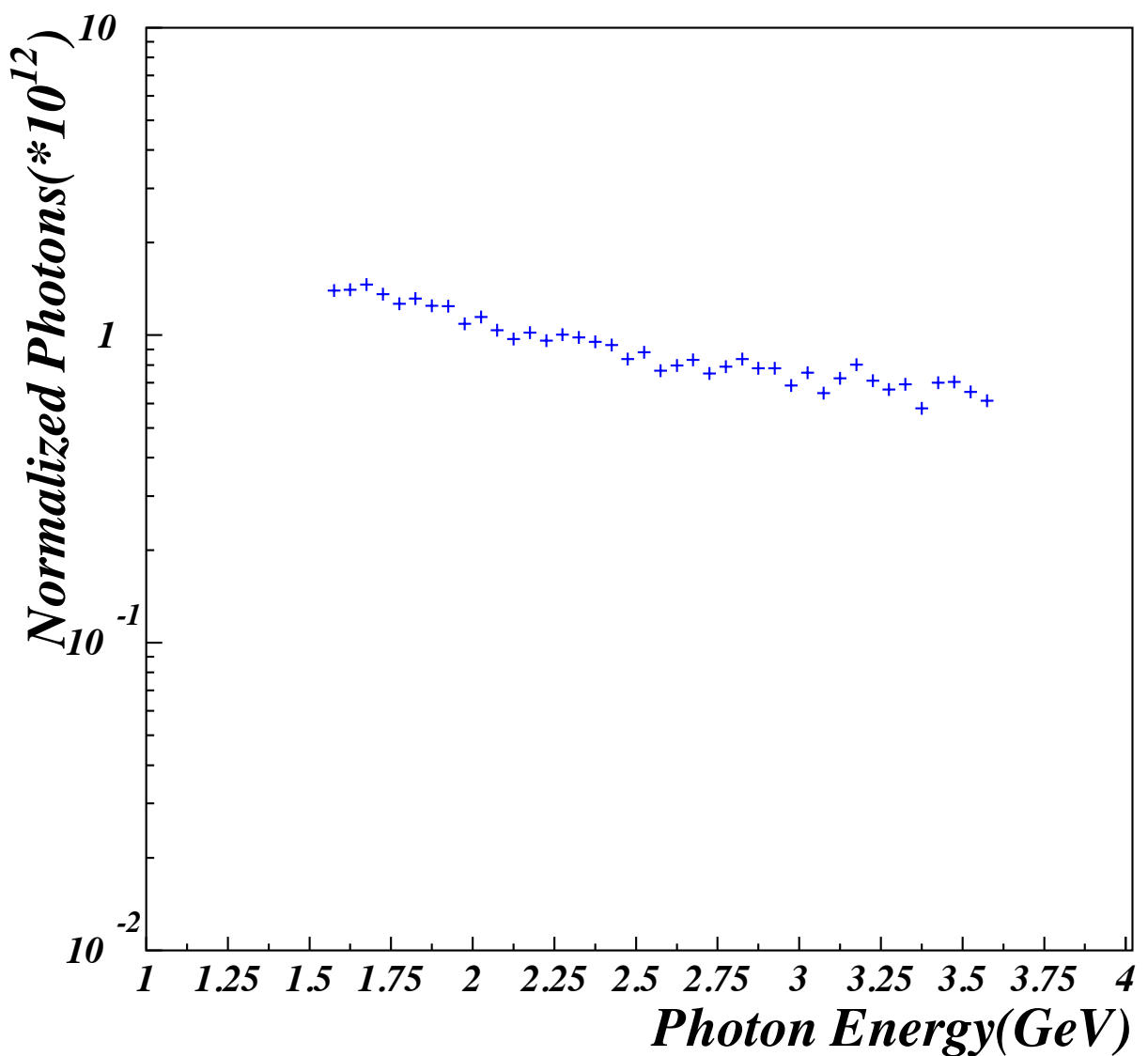


FIG. 63. Photon flux as a function of photon beam energy.

CHAPTER 4

PHYSICS RESULTS

The purpose of this analysis is to measure the differential cross sections and spin observables of ϕ meson photoproduction in 'Neutral' decay mode $\gamma + p \rightarrow p' + K_S + K_L$. In this chapter the preliminary results of the analysis will be described and compared with previous results obtained for the 'Charged' decay channel of ϕ meson $\gamma + p \rightarrow p' + K^+ + K^-$.

4.1 DIFFERENTIAL CROSS SECTIONS

In this section we present preliminary results for the differential cross sections. The *cross section* is defined as the probability that the particular interaction will take place between particles. The differential cross section values are obtained for different $t - t_{min}$ bins and for 100 MeV photon energy bins in photon energy range 1.6-2.6 GeV. For the measurement the following expression for the differential cross section is used:

$$\frac{d\sigma}{dt} = \left(\frac{A_{target}}{\mathcal{F}(E_\gamma)\rho_{target}L_{target}N_A} \right) \times \frac{\mathcal{Y}(E_\gamma, t^\phi - t_{min}^\phi)}{\Delta(t^\phi - t_{min}^\phi)\eta(E_\gamma, t^\phi - t_{min}^\phi)\mathcal{E}} \frac{1}{BR(\gamma p \rightarrow p' K_S K_L)}$$

Here N_{target} , ρ_{target} and L_{target} are the atomic weight, density and the length of the target, respectively. N_A is the Avogadro number and $\mathcal{F}(E_\gamma)$ is the total number of photons incident on a target in a given photon energy bin. $\Delta(t^\phi - t_{min}^\phi)$ is the $t^\phi - t_{min}^\phi$ bin size, which was selected to be 0.08. $BR \approx 0.34$ is the branching ratio of the ϕ meson production in Neutral channel. $\mathcal{Y}(E_\gamma, t^{phi} - t_{min}^{phi})$ is the data signal yield in given photon energy and $t^\phi - t_{min}^\phi$ bin , after the background subtraction (

see 3.6). $\eta(E_\gamma, t^\phi - t_{min}^\phi)$ is the acceptance in $(E_\gamma, t^\phi - t_{min}^\phi)$ bin (see 3.7.2) and \mathcal{E} is the efficiency for every data event in the given bin (3.3).

There is a cut applied to the acceptance to be $\eta(E_\gamma, t^\phi - t_{min}^\phi) < 0.001$.

The fig.64 shows results for the $|t - t_{min}|$ dependence of differential cross section $d\sigma/dt$ for 100 MeV wide photon energy bins in energy range 1.6-2.6 GeV. At lower values of the four momentum transfer the cross section drops exponentially with $|t - t_{min}|$. This is expected by the ruling Pomeron exchange mechanism of ϕ meson photoproduction in this regime. At higher values of t there some local increase and drop in differential cross section is observed that distorts the exponential behavior. This might be because of N/N^* exchange contributions in the cross section. We did not include the data for the first bin of very low t , because of problems related to GSIM to describe this forward angle region of the detector.

Fig.65 presents the preliminary results for the differential cross section $d\sigma/d\cos\theta_{c.m.}$ plotted as a function of $\cos\theta_{c.m.}$, where $\theta_{c.m.}$ is the ϕ meson polar angle in the center-of-mass system of $\gamma p \rightarrow \phi p$. The results are plotted for 100 Mev photon energy bins in 1.6-2.6 GeV range. The bin size of x axis is 0.1.

Fig.66 and 67 show the \sqrt{s} dependence of the differential cross section $d\sigma/dt$ in different $\cos\theta_{c.m.}^\phi$ bins. First, $d\sigma/dt$ is measured at different photon energies E_γ (for 50 MeV wide bins of E_γ in 1.6-2.6 GeV energy range), then the result is plotted as a function of s , converting E_γ into \sqrt{s} with $s = M_p^2 + 2M_p E_\gamma$ relation ($M_p = 0.93828$ is the proton mass). The cross sections are measured using the following relation:

$$\frac{d\sigma}{dt} = \frac{1}{2} \left(\frac{1}{E_\gamma |\vec{p}_\phi|} \right)_{c.m.} \left(\frac{d\sigma}{d\cos\theta_{c.m.}^\phi} \right) \quad (63)$$

Fitting the $|t - t_{min}|$ dependence of the differential cross section $d\sigma/dt$ with an exponential function of $A e^{-\beta|t-t_{min}|}$ form the differential cross section at $t = t_{min}$ point (fig. 68(a)) and the β slopes of the $|t - t_{min}|$ distributions (fig. 68(b)) are measured for 100 MeV wide energy bins in 1.6-2.6 GeV range. The differential cross section still has some local structure at about 1.8-2.4 GeV as the one observed in 'Charged' decay mode, although in this case the peak is smaller. The slope also has some local enhancement in the energy range of 1.6-2.3 GeV. These results strongly depend on the fit region of $t - t_{min}$ distribution of the cross section. The higher t

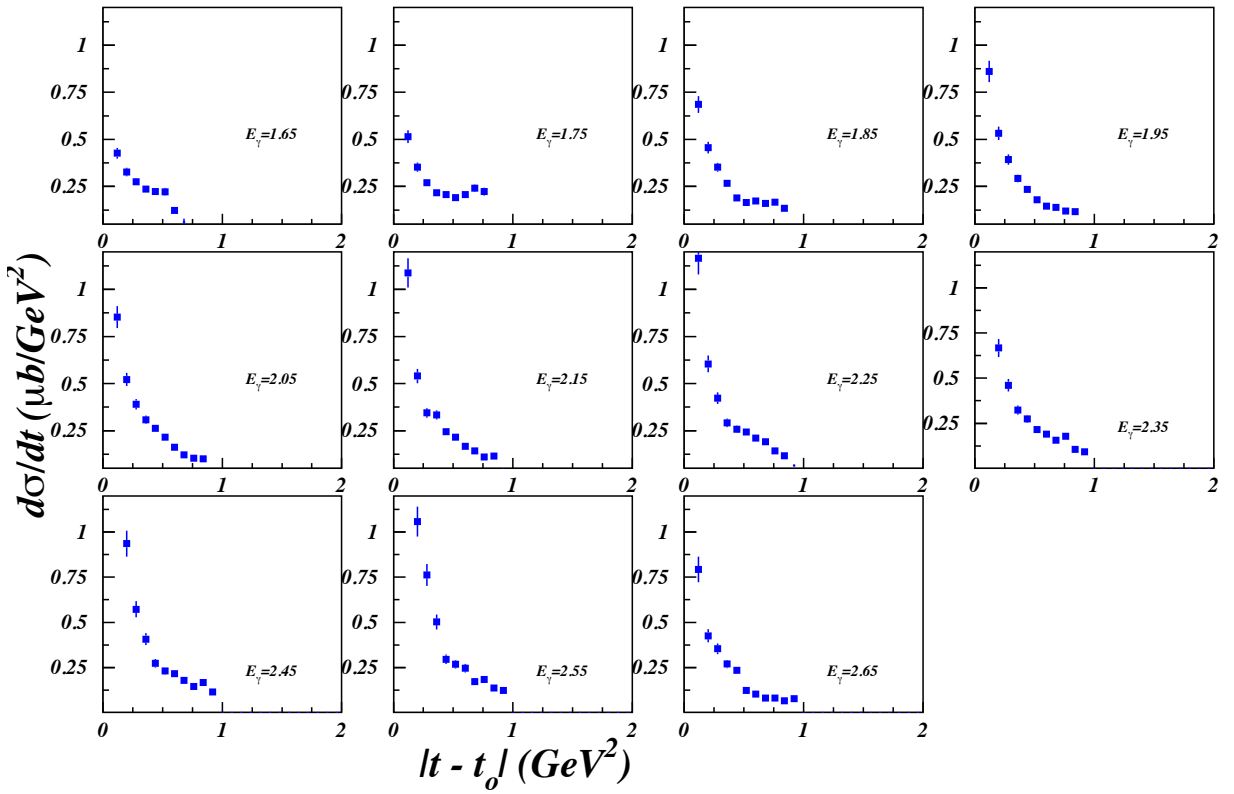


FIG. 64. The $|t - t_{min}|$ dependence of the ϕ meson differential cross section $d\sigma/dt$ in different photon beam energy bins of 1.6-2.6 GeV energy range.

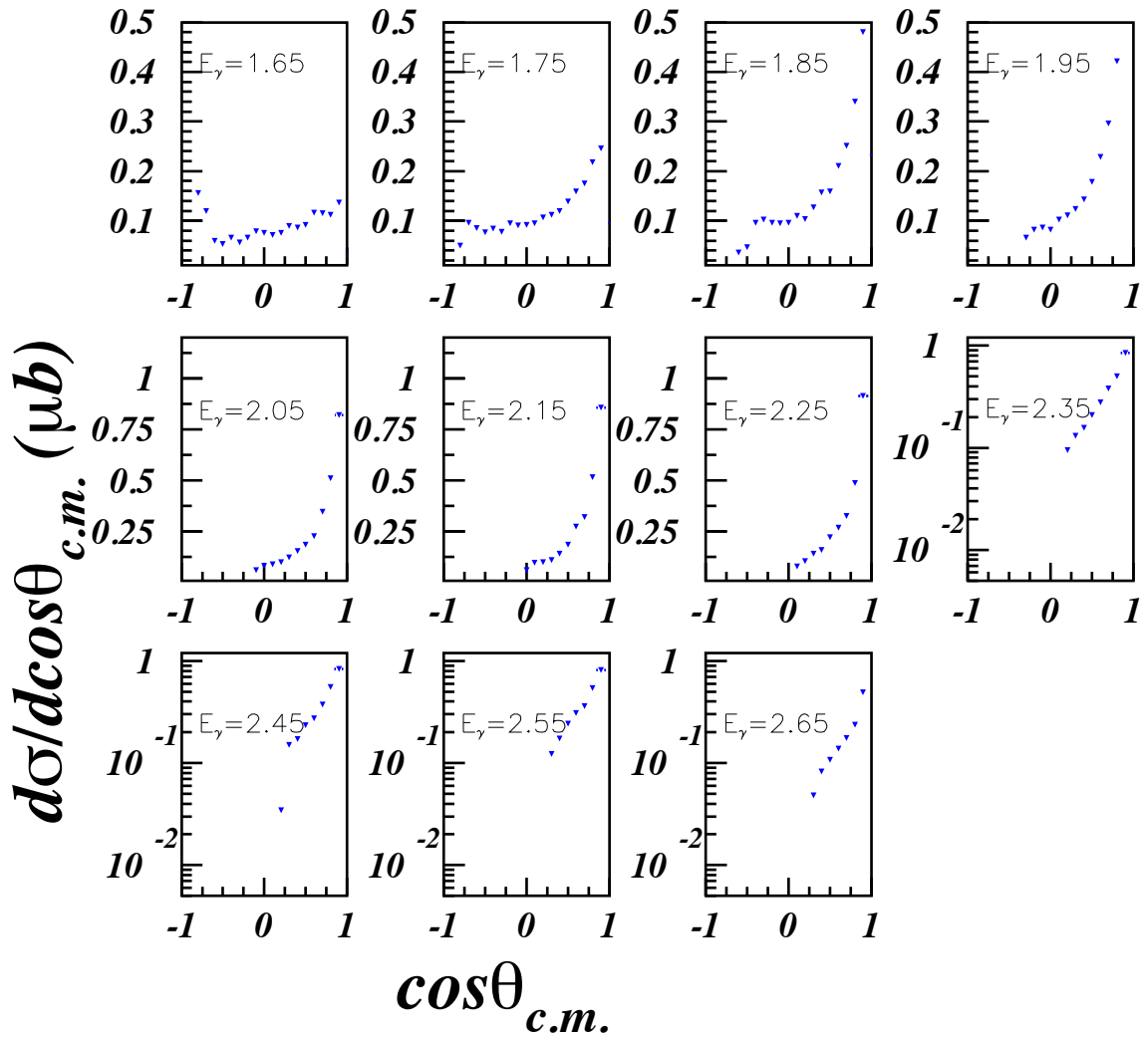


FIG. 65. The $\cos\theta_{c.m.}^\phi$ dependence of the ϕ meson differential cross section $d\sigma/d\cos\theta_{c.m.}$ for different photon beam energy bins of 1.6-2.6 GeV energy range.

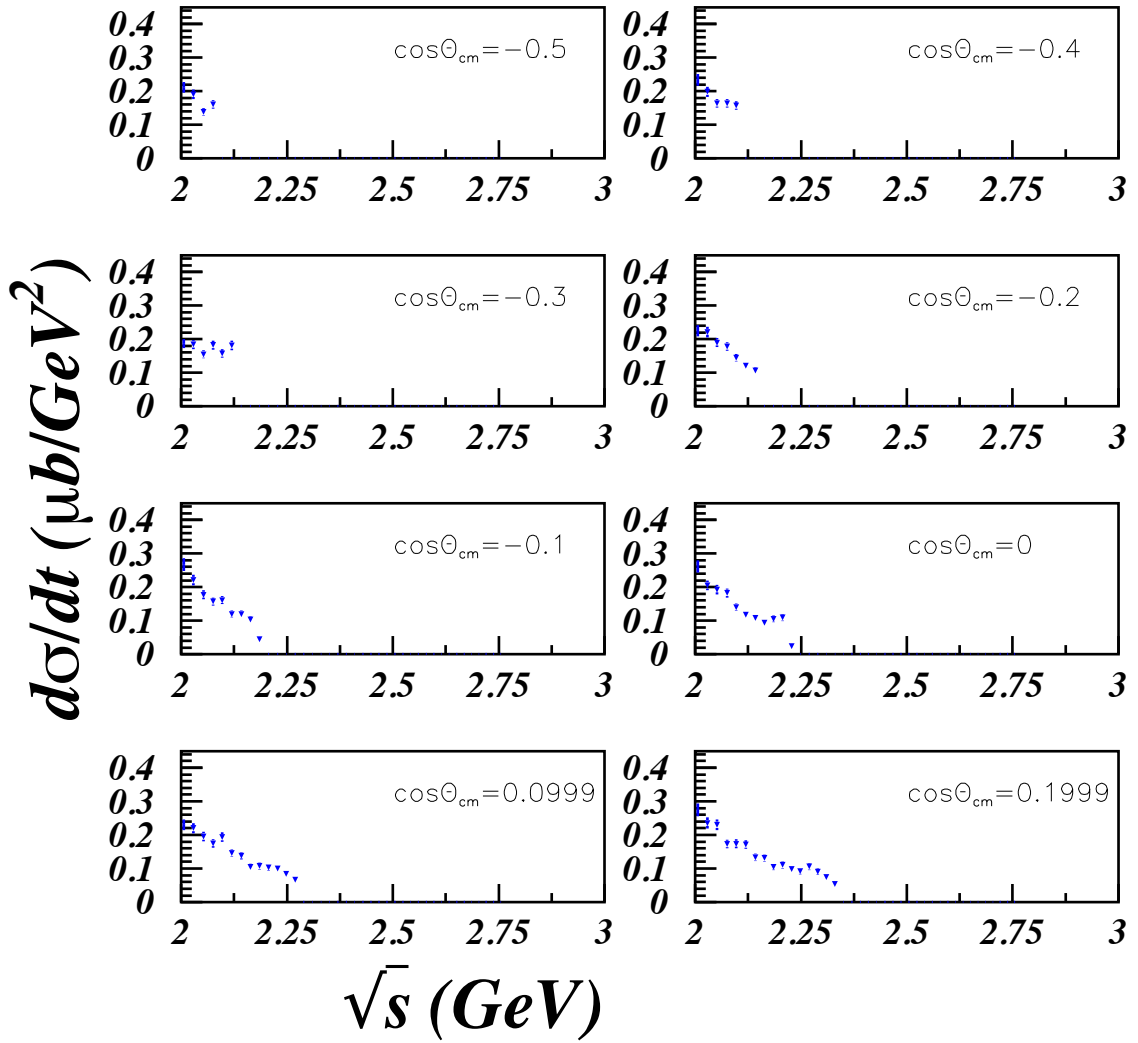


FIG. 66. The \sqrt{s} dependence of the ϕ meson differential cross section $d\sigma/dt$ in different $\cos\theta_{c.m.}$ bins for $-0.55 < \cos\theta_{c.m.} < 0.25$ range.

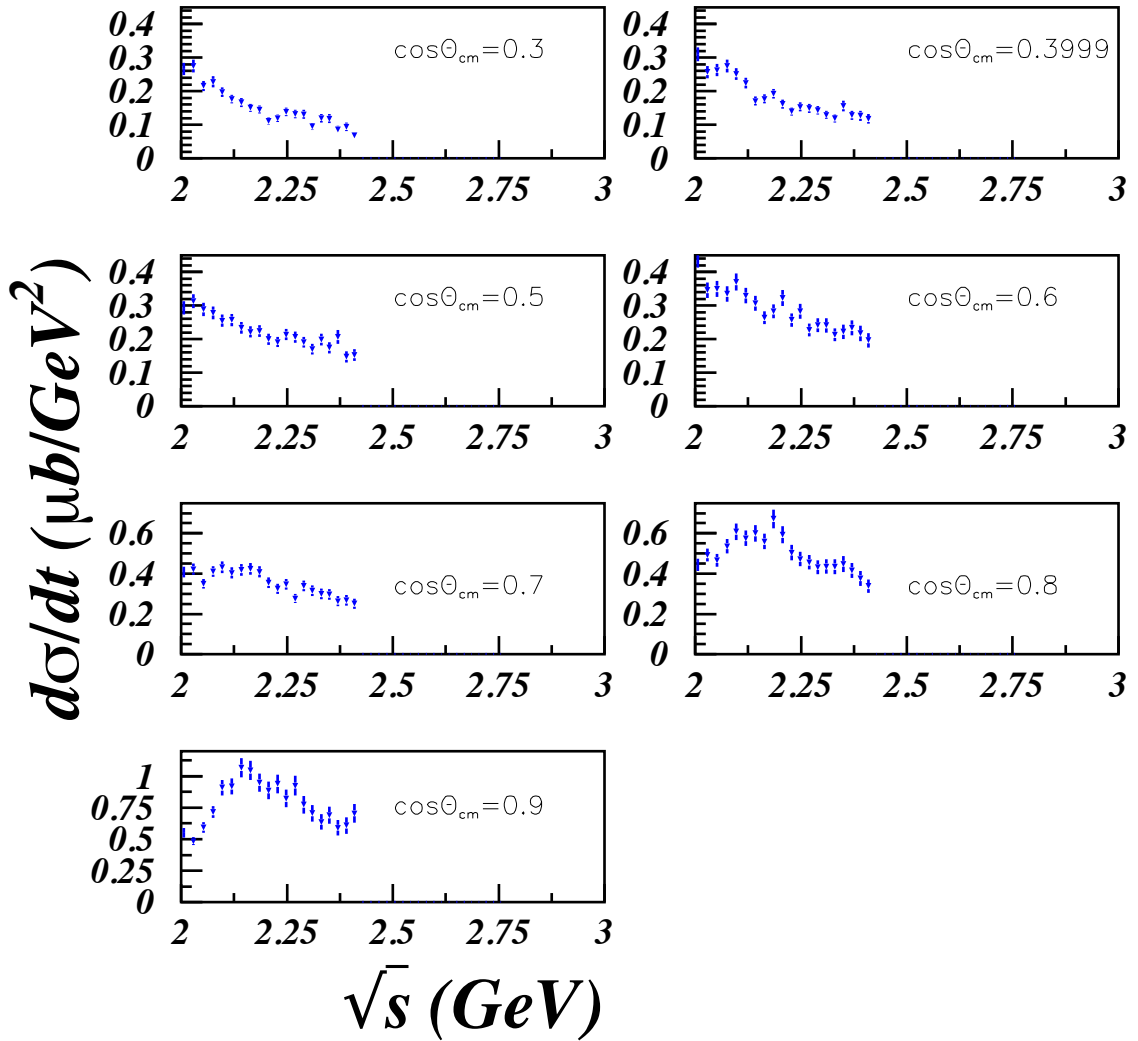


FIG. 67. The \sqrt{s} dependence of the ϕ meson differential cross section $d\sigma/dt$ in different $\cos\theta_{c.m.}$ bins for $0.25 < \cos\theta_{c.m.} < 0.95$ range.

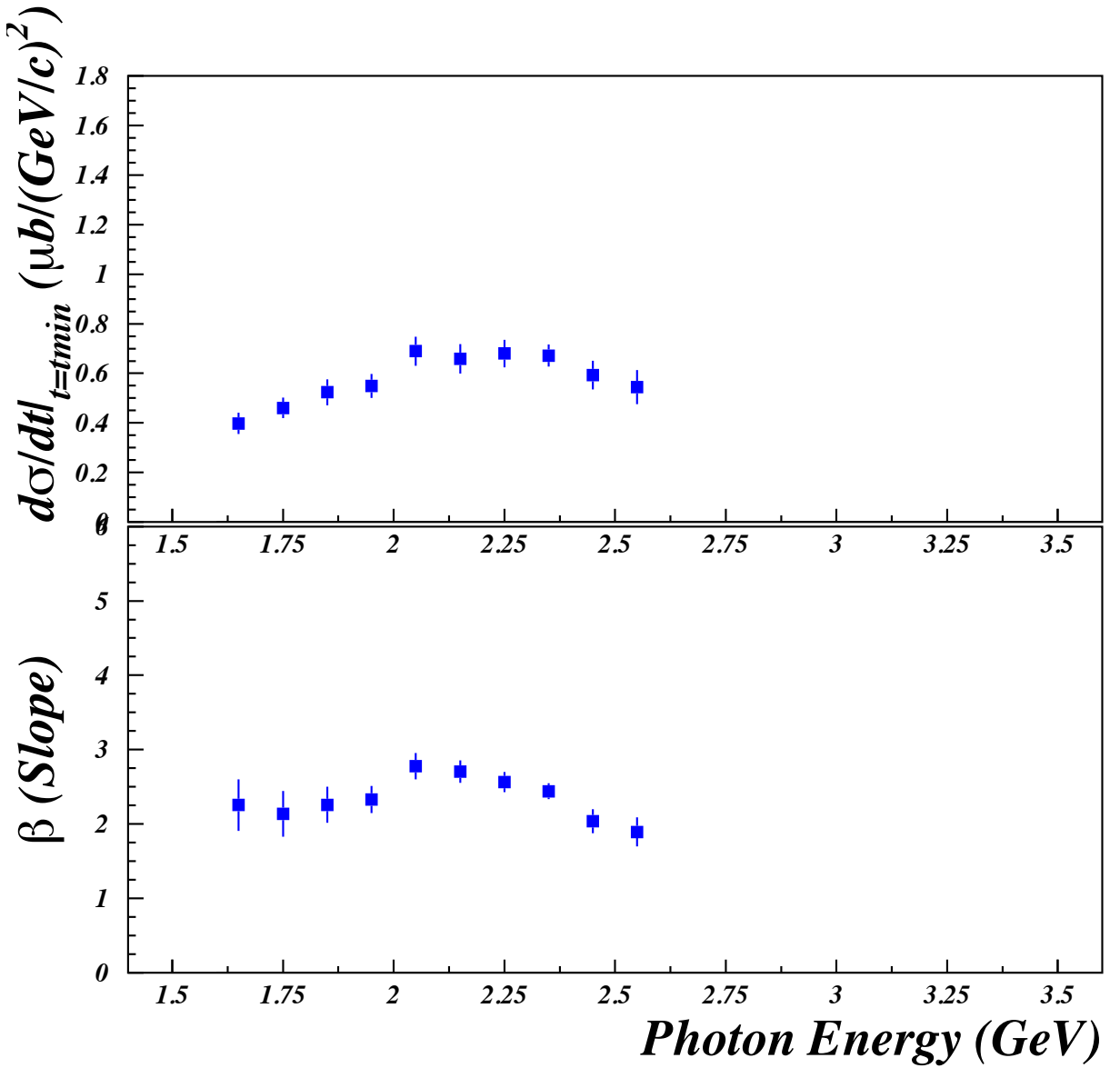


FIG. 68. Differential cross section $d\sigma/dt$ at $t = t_{min}$ (a) and ϕ meson photoproduction slope β (b) for the Neutral decay channel plotted as functions of photon beam energy E_γ in 1.6-2.6 GeV energy range. The error bars represent the statistical errors, errors of the flux calculation, efficiency error at 40% efficiency cut, acceptance errors. The systematic errors are included as dashed pink regions at horizontal axis.

regions, where the cross sections increase and deviate from exponential behavior, are not included in fits.

All presented cross section results are measured with a 40% efficiency cut.

4.2 ANGULAR DISTRIBUTION FUNCTIONS AND SPIN OBSERVABLES

For unpolarized beam the $\phi \rightarrow K_S K_L$ decay angular distribution in the rest frame of ϕ meson is described as a function of polar(Θ) and azimuthal(Φ) angles by equation (17). Below we present the decay angular distribution of $\phi(1020)$ meson in polar and azimuthal angles and spin-density matrix element ρ^0 measured for Neutral decay channel of ϕ in two frames - Helicity and Gottfried-Jackson (see 2.2).

Fig. 69 shows the decay angular distribution of ϕ as a function of polar angle Θ in Helicity frame for 100 MeV wide photon energy bins. The binning size of the x axis is 0.1. The decay has quadratic dependence on $\cos\Theta$ function in lower photon energy bins 1.6 - 2.2 GeV and bends towards the forward angles in higher photon energies.

Fig. 70 describes the decay angular distribution of ϕ as a function of polar angle Θ in Gottfried-Jackson frame with a cut $-0.2 < t + |t|_{min}$. The bin sizes are kept the same as for the Helicity frame. Green points in 2.2-2.4 GeV energy interval are the results of LEPS collaboration (SPring-8) analysis [2]. The current analysis distribution is much different from the LEPS result in the two bins. The $\cos^2\Theta$ dependence of the decay distribution at lower energies bends towards the forward angles as the energy grows. This might be due to the possible interference of S and P waves or signal-background interference.

Fig. 71 and 72 show the ϕ meson decay distributions in azimuthal angle Φ in Helicity and GJ frames. In both cases $-0.2 < t + |t|_{min}$ cut is applied on four momentum transfer. The distributions are measured for 200 MeV wide energy bins in 1.6-2.6 GeV photon energy interval. The Φ angle is converted to radians and the x axis has 12 bins in (0-6.3) interval. In fig.72 the green points in two energy bins correspond to LEPS results for the charged decay channel of ϕ [2]. The distributions

measured by LEPS and the current analysis result differ for this energy interval.

The spin-density matrix element components ρ_{00}^0 and ρ_{1-1}^0 were measured for different photon energies from the fits of polar and azimuthal angle dependence parts of decay distributions. For Helicity frame ρ_{00}^0 was obtained fitting figure 69 distributions with $a[1 - b + (3b - 1)x^2]$ function and ρ_{1-1} was extracted fitting the decay distributions in azimuthal angle (fig. 71) with function $a(1 - 2b \cos 2x)$ (see fig. 73). To be able to extract the ρ_{00}^0 in GJ frame we had to modify the fit function for the Helicity frame adding a linear term. In GJ frame the ρ_{00}^0 was measured fitting fig. 70 distributions with $a[1 - b + (3b - 1)x^2 + cx]$ function. The ρ_{1-1}^0 component in GJ frame was measured fitting fig. 72 distributions with the same function as for the Helicity frame. Figure 74 shows this analysis results for ρ_{00}^0 and ρ_{1-1}^0 as functions of photon beam energy E_γ in GJ frame. In both frames the ρ_{00}^0 components are much higher than the ρ_{1-1}^0 components, which is expected by theory (see fig. 13 in 2.5.2).

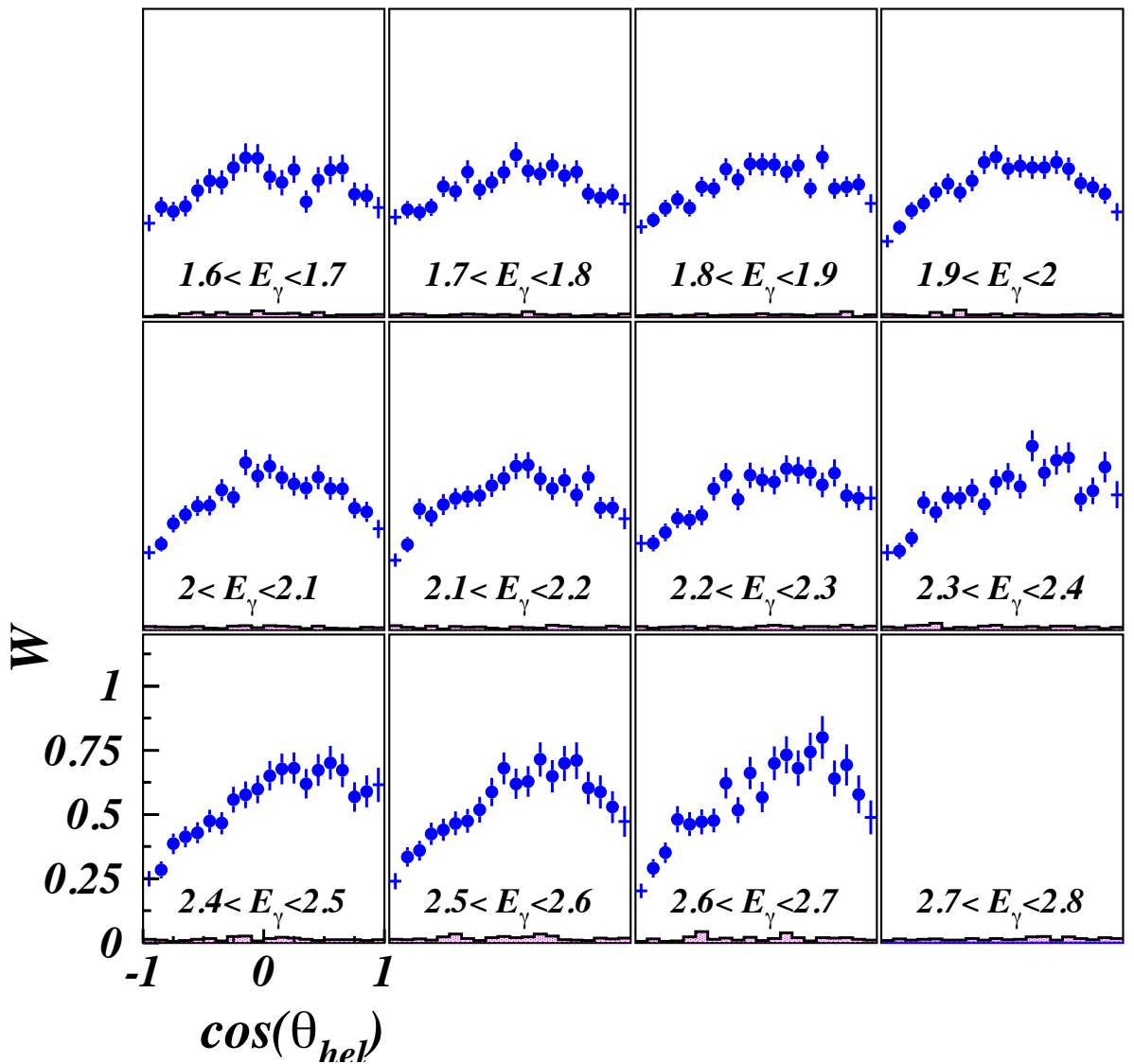


FIG. 69. The decay distribution of ϕ meson as a function of polar angle Θ in Helicity frame for the 'neutral' decay channel of $\phi(1020)$ meson.

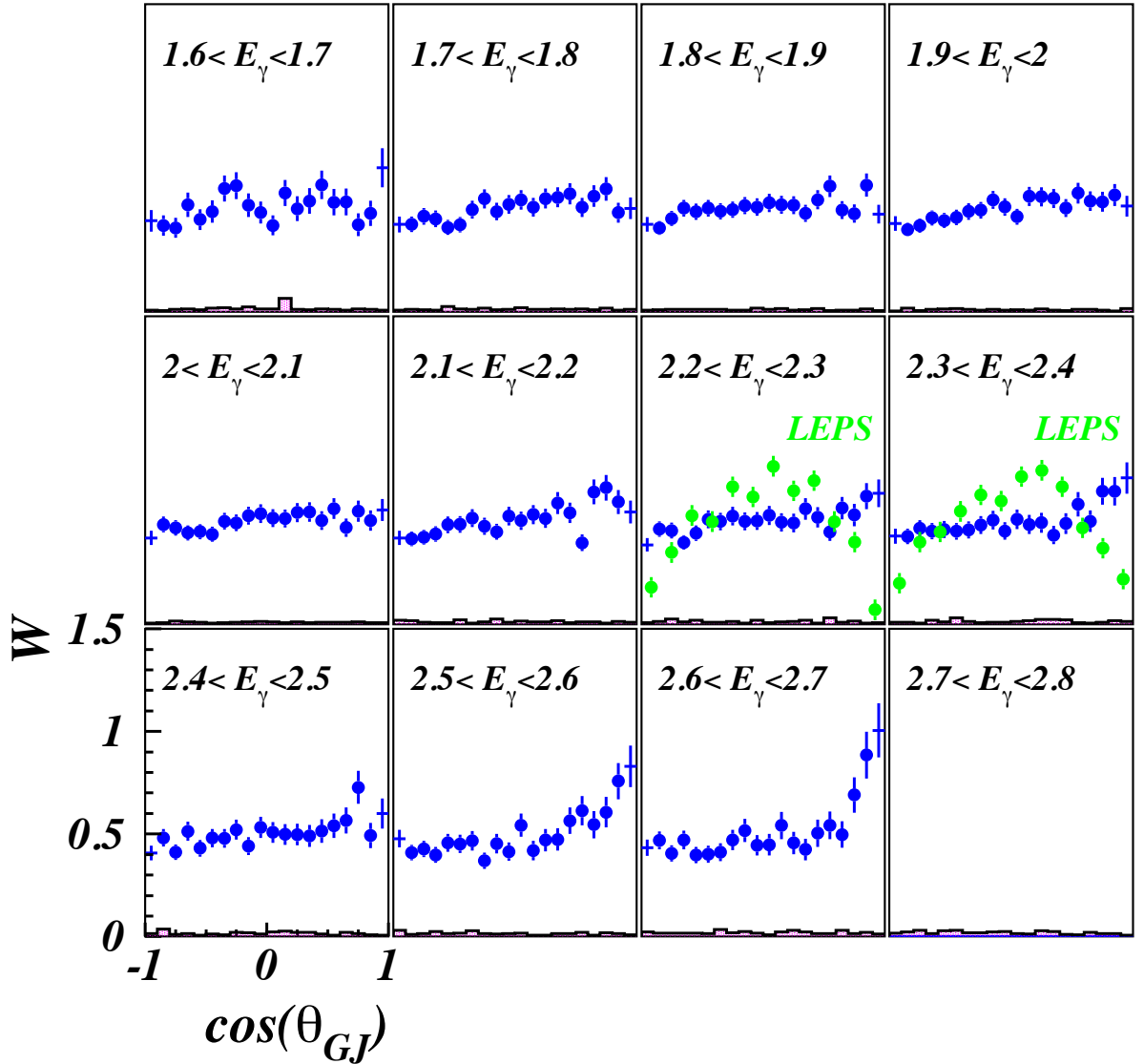


FIG. 70. The decay distribution of ϕ meson as a function of polar angle Θ in Gotfried-Jackson frame for the 'neutral' decay channel of $\phi(1020)$ meson.

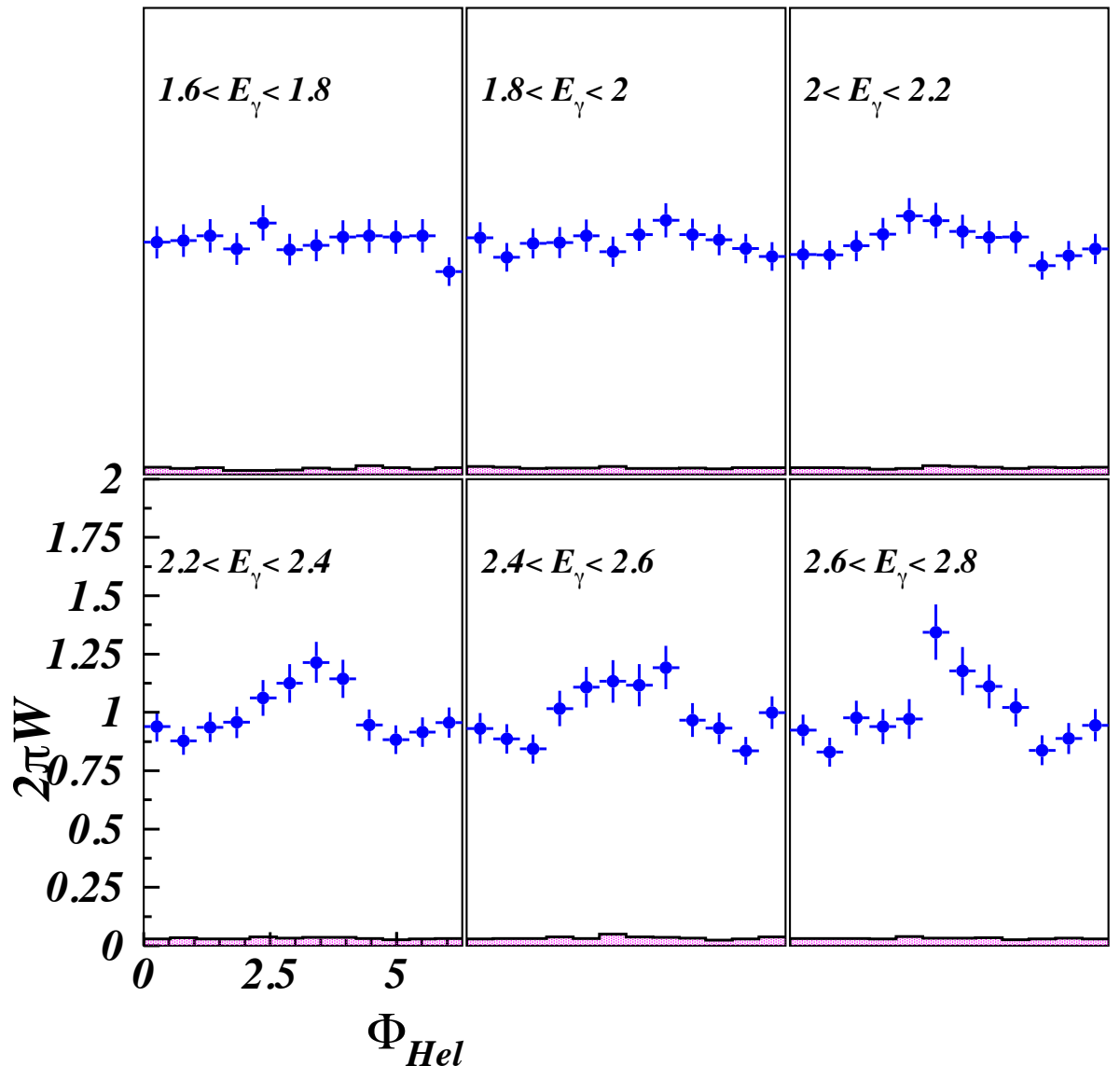


FIG. 71. The decay distribution of ϕ meson as a function of azimuthal angle Φ in Helicity frame for the 'neutral' decay channel of $\phi(1020)$ meson.

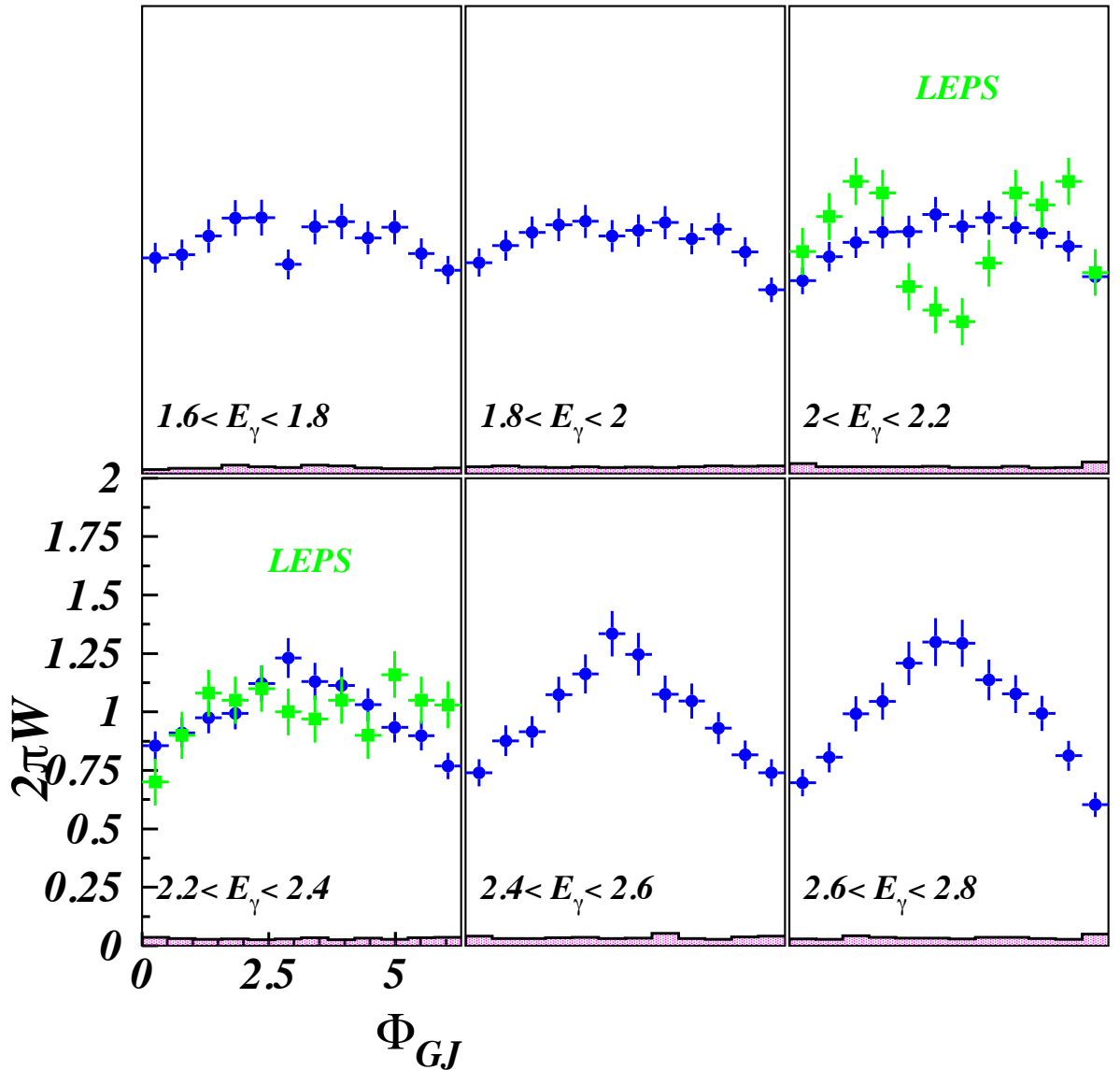


FIG. 72. The decay distribution of ϕ meson as a function of azimuthal angle Φ in Gottfried-Jackson frame for the 'neutral' decay channel of $\phi(1020)$ meson.

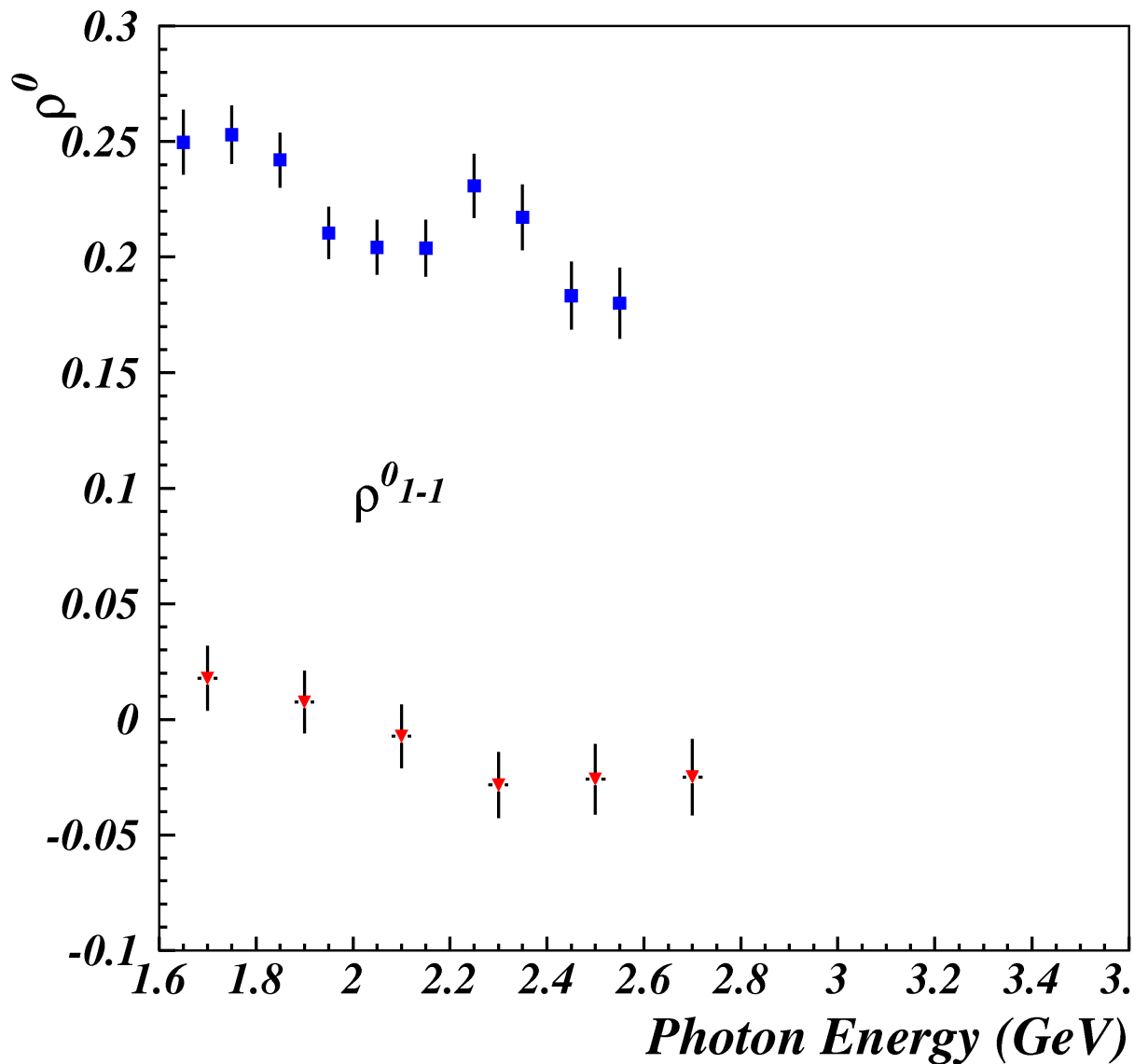


FIG. 73. Spin-density matrix element components ρ_{00}^0 (blue) and ρ_{1-1}^0 (red) for different photon beam energies in 1.6-2.6 GeV range in Helicity frame.

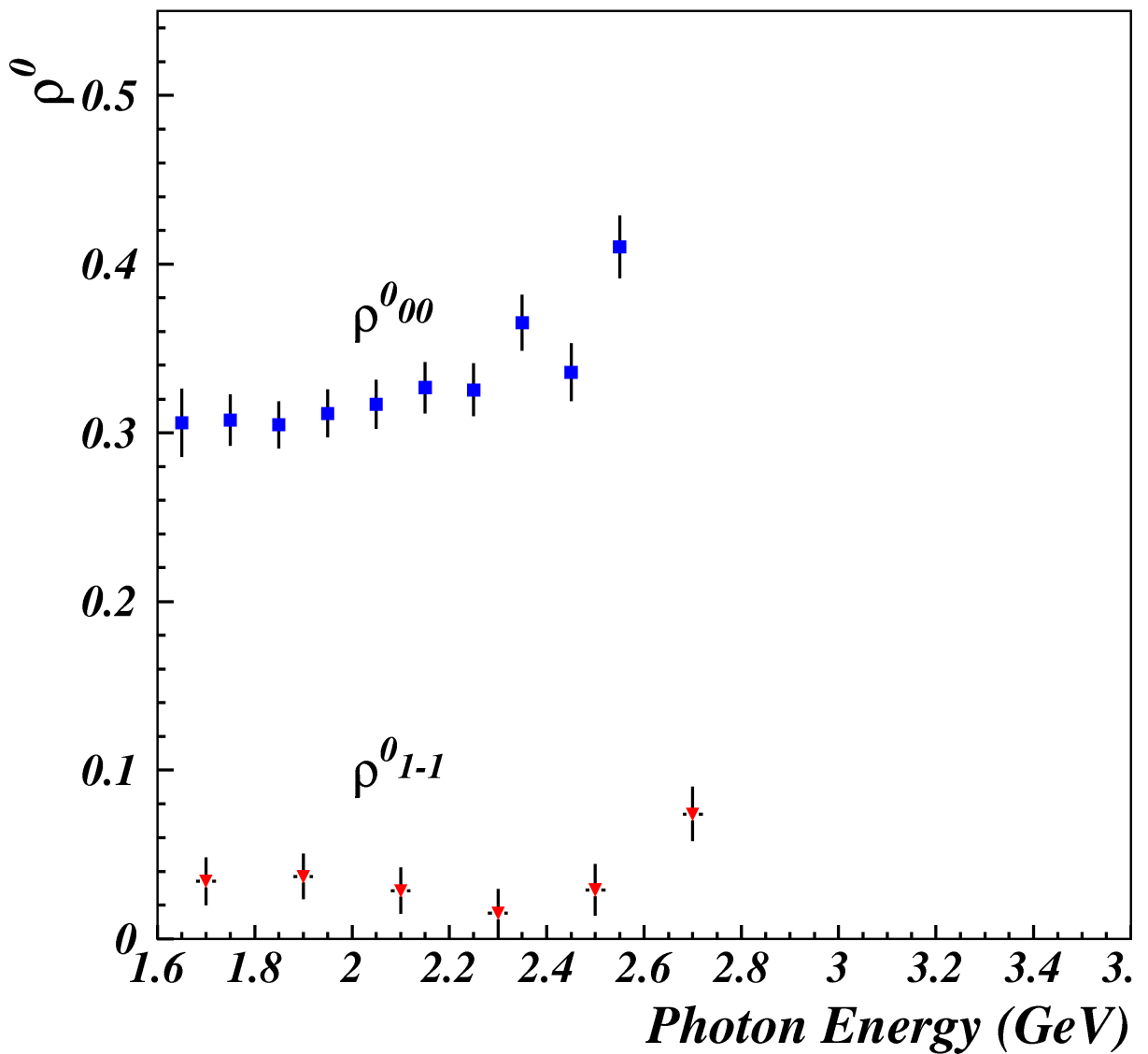


FIG. 74. Spin-density matrix element components ρ_{00}^0 (blue) and ρ_{1-1}^0 (red) for different photon beam energies in 1.6-2.6 GeV range in Gottfried-Jackson frame.

4.3 SUMMARY

The 'Charged' decay channel of $\phi(1020)$ has been studied before. The results show some peak/dip structure in differential cross section in approximately 1.8-2.2 GeV photon energy range. In the 'Charged' decay mode there is a resonance $\Lambda(1520)$ which can be simultaneously produced with ϕ meson. The phase spaces of ϕ and Λ overlap in the same energy range where the local structure in differential cross sections was observed. The two coexisting resonances can interfere. This could be a possible reason for the observed behavior of the cross section. One way to check this is to measure the ϕ production cross section eliminating the coexisting $\Lambda(1520)$. Another check could be performed by studying the 'Neutral' decay mode of ϕ (there were no existing data for this channel), where there is no known strong coexisting resonance as the $\Lambda(1520)$ produced.

In this work we describe in a detail our analysis of $\phi(1020)$ meson photoproduction in its 'Neutral' decay mode $\gamma p \rightarrow \phi p \rightarrow p K_S K_l$ using data set of g11 experiment. We present preliminary results of differential cross sections versus different variables measured in this experiment. In particular, it includes results of the analysis for the ϕ decay angular distributions and spin-density matrix elements ρ_{00}^0 and ρ_{1-1}^0 in Helicity and Gottfried-Jackson frames. As we observed, in this mode the differential cross section $d\sigma/dt$ measured at $t = t_{min}$ point still shows a local peak/dip structure as it was observed in the 'Charged' mode, but the size of the peak and the slope of the t distribution is smaller for the Neutral mode in the energy range 1.7-2.4 GeV (fig. 68). The observation of the enhancement in differential cross section of ϕ photoproduction in both decay modes could be caused by interference with simultaneous production of other resonance states leading to the same final state, and/or there might be also some other processes that influence the ϕ photoproduction cross section. Understanding the reason for the observed effect requires further studies.

BIBLIOGRAPHY

- [1] J. Barth *et al* (SAPHIR Collaboration). *Low-energy photoproduction of Φ -mesons.* Eur. Phys. J. A **17**, 269 (2003).
- [2] T. Mibe *et al* (LEPS Collaboration). *Diffractive ϕ -meson photoproduction on the proton near threshold.* Phys. Rev. Lett. 95, **182001** (2005).
- [3] D. P. Barber *et al.* *Forward and Wide Angle Elastic ϕ -Meson Photoproduction on Hydrogen Between 2.8 and 4.8 GeV.* Z. Phys. C **12**, 1 (1982).
- [4] J. Ballam *et al.* *Vector-Meson Production by Polarized Photons at 2.8, 4.7, and 9.3 GeV.* Phys. Rev. D **7**, 31503177 (1973).
- [5] H. J. Besch *et al.* *Photoproduction of ϕ Meson on Protons at 2.0 GeV.* Nucl Phys. B **70**, 257 (1974).
- [6] H.-J. Behrend *et al.* *Elastic and Inelastic ϕ Photoproduction.* Nucl. phys **B144**, 22-60 (1978).
- [7] E. Anciant *et al* (CLAS Collaboration). *Photoproduction of $\phi(1020)$ Meson on the Protons at Large momentum Transfer.* Phys. Rev. Lett. **85** 4682 (2000).
- [8] J. Breitweg *et al* (ZEUS Collaboration). *Measurement of diffractive photoproduction of vector mesons at large momentum transfer at HERA.* Eur. Phys. J. C **14**, 213-238 (2000).
- [9] Ya Azimov. J. Phys. G: Nucl. Part. Phys. **37** 023001 (2010) .
- [10] M. Amarian, D. Diakonov, M. Polyakov. Phys. Rev. D **78** 074003 (2008).
- [11] C. Nepali. http://www.jlab.org/Hall-B/secure/hadron/meetings/31oct08/cnepali_Lambda1520_Oct31_2008.pdf
- [12] S. Okubo, Phys. Lett. **5**, 165 (1963); G. Zweig,CERN Report No. 8182/TH 401 and 8419/TH 412, 1964 (unpublished); J. Iizuka, Prog. Theor. Phys. Supp. **37/38**, 21 (1966); G. Alexander, H.J. Lipkin, and P. Scheck, Phys. Rev. Lett. **17**, 412 (1966).

- [13] A.I. Titov, T.-S.H. Lee, H. Toki, and O. Streltsova, Phys. Rev. C **60**, 035205 (1999).
- [14] A.I. Titov and T.-S.H. Lee, Phys. Rev. C **67**, 065205 (2003).
- [15] R.A. Williams, Phys. Rev. C **57**, 223 (1998).
- [16] K. Schilling, K. Seyboth and G. Wolf, Nucl. Phys. **B15**, 397 (1970).
- [17] D.G. Cassel *et al.*, Phys. Rev. D **24**, 2787 (1981).
- [18] D.W.G.S. Leith, in *Electromagnetic Interactions of Hadrons*, edited by A. Donnachie and G. Shaw (Plenum Press, New York, 1978), Vol. 1, p. 345.
- [19] A. Donnachie and P.V. Landshoff, Phys. Lett. B **185**, 403 (1987); Nucl. Phys. **B244**, 322 (1984); *ibid.* **B267**, 690 (1986).
- [20] H. Suganuma, S. Sasaki, and H. Toki, Nucl. Phys. **B435**, 207 (1995).
- [21] J.-M. Laget and R. Mendez-Galain, Nucl. Phys. **B581**, 397 (1995).
- [22] M. Diehl, Eur. Phys. J. C6, 503 (1999).
- [23] F.E. Low, Phys. Rev. D **12**, 163 (1975); S. Nussinov, Phys. Rev. Lett. **34**, 1286 (1975).
- [24] J.R. Cudel, A. Donnachie and P.V. Landshoff, Nucl. Phys. **B322**, 55 (1989).
- [25] P.V. Landshoff and O. Nachtmann, Z. Phys. C **35**, 405 (1987).
- [26] A.I. Titov, Y. Oh S.N. Yang, and T. Morii, Phys. Rev. C **58**, 2429 (1998); Nucl. Phys. **A684**, 354 (2001).
- [27] Q. Zhao, J.P. Didalez, M. Guidal and E. Hourany, Nucl. Phys. A **684**, 351 (2001).
- [28] J.-M. Laget, Phys. Lett. B **489**, 3133 (2000).
- [29] N.I. Kochelev and V. Vento, Phys. Lett. B **515**, 375 (2001); hep-hp/0112292.
- [30] B. Friman and M. Soyeur, Nucl. Phys. **A600**, 477 (1996).

- [31] A.I. Titov, T.-S.H. Lee, Phys. Rev. C **66**, 015204 (2002).
- [32] T. Nakano and H. Toki, in *Proceedings of the International Workshop on Existing Physics and New Accelerator Facilities*, SPring-8, Hyogo, 1997 (World Scientific Singapore, 1998), p.48.
- [33] K. Hagiwara *et al.* [Particle Data Group Collabpration], Phys. Rev. D **A66**, 010001 (2002).
- [34] U.-G. Meissner, V. Mull, J. Speth, and J.W. Van Orden, Phys. Lett. B **408**, 381 (1997).
- [35] H.J. Besch, G. Hartmann, R. Kose, F. Krautschneider, W. Paul, and U. Trinks, Nucl. Phys. B**70**, 257 (1974).
- [36] The CLAS Collaboration, E. Anciant *et al.*, Phys. Rev. Lett. **85**, 4682 (2000).
- [37] M. Battaglieri *et al.* *Study of Pentaquark States in Photoproduction off Protons.* CLAS Experiment Proposal E-04-017.
- [38] D.I. Sober, et al. *The bremsstrahlung tagged photon beam in Hall B at JLab.* Nucl Inst Meth A **440**, 263 (2000).
- [39] S. Christo. The g11a Target Cell, <http://www.jlab.org/~christo/g11a%20target.html>
- [40] Alan J. Street et al. *Final site assembly and testing of the superconducting toroidal magnet for the CEBAF Large Acceptance Spectrometer (CLAS).* IEEE Trans. Mag. **32**, No. 4, 2074 (1996).
- [41] M.D. Mestayer et al. *The CLAS drift chamber system.* Nucl Inst Meth A **449**, 81 (2000).
- [42] D.S. Carman et al. The Region One drift chamber for the CLAS spectrometer. Nucl Inst Meth A **419**, 315 (1998).
- [43] Y.M. Qin et al. *Prototype studies and design considerations for the CLAS Region Two drift chambers.* Nucl Inst Meth A **367**, 316 (1995).

- [44] F.J. Barbosa, et al.*A drift chamber system for a toroidal detector.* Nucl Inst Meth A **323**, 19 (1992).
- [45] E. Smith et al.*The time-of-flight system for CLAS.* Nucl Inst Meth A **432**, 265 (1999).
- [46] Y.G. Sharabian et al.*A new highly segmented start counter for the CLAS detector.* Nucl. Phys. A **556**, 246 (2006).
- [47] David J. Tedeschi *et al*, Phi Meson Photoproduction with CLAS, CLAS Analysis Note (under review) (2008).
- [48] M. Ungaro, R. De Vita, L. Elouadrhiri, g11 data processing, CLAS-NOTE 2005-14.
- [49] V. Kubarovskiy.
- [50] E. Pasyuk, *The CLAS ELOSS Package.* Software available via the CLAS CVS repository under clas/packages/utilities/eloss.
- [51] W.-M. Yao *et al.* Review of Particle Physics. J. Phys. G 33, 1 (2006).
- [52] S. Stepanyan. *Evidence for an Exotic Pentaquark Baryon State $\Theta^+(1530)$, in the $\gamma d \rightarrow pK^+K^-n$ reaction.* CLAS Analysis Note 2003-105.
- [53] M. Williams, Ph.D. Thesis, *Measurement of Differential Cross Sections and Spin Density Matrix Elements along with a Partial Wave Analysis for $\gamma p \rightarrow p\omega$ using CLAS at Jefferson Lab,* Carnegie Melon University (2007).
- [54] Z.A. Krahn, Ph.D Thesis, *Photoproduction of η and η' Mesons Using CLAS at JLAB,* Carnegie Melon University (2007).
- [55] R. Bradford and R.A. Schumacher. *Liquid Hydrogen Density in the G1C CLAS Cryotarget.* CLAS Note 2002-003.
- [56] J. Ball and E. Pasyuk. *Photon Flux Determination Through Sampling of 'out-of-time' Hits with the Hall B Photon Tagger.* CLAS Note 2005-002.

- [57] R. De Vita, M. Battaglieri. *Analysis of ω production at 90° degrees in the g11 data set.* CLAS Analysis Note 2009-105 (2010).
- [58] R. De Vita. *Private Communication.*
- [59] /mss/clas/g11a/production/pass1/v1/trip.